

POLITECNICO DI TORINO

Master Degree in Aerospace Engineering

Master Degree Thesis

# 3D Aerodynamic Characterization of Rotor Systems for Martian Drones



**Supervisor**

Prof. Domenic D'Ambrosio

**Candidate**

Bergamino Davide

**Supervisor in  
Thales Alenia Space Italia**

Ing. Vincenzo Mareschi

March 2019



# Summary

The aim of this thesis is to find a correlation between the experimental tests performed in a vacuum chamber at Thales Alenia Space Italia, at the Turin site, concerning a rotor operating in the Martian environment, with a CFD model. Starting from a simple model, the details are gradually increased in order to get as close as possible to reality and then to the experimental case. Gridgen software, distributed by Pointwise, is used during the creation of the grid while in the calculation phase, the CFD ++ software produced by Metacomp is used. This last software allows to specify the motion of the grid and in particular allows to operate with rotating volumes at different speeds. In this specific case there is only a rotating volume, the one that includes the rotor.

As it can be understood, the phenomenon that develops inside the vacuum chamber is highly unsteady and quite complex. For this reason it is not expected a close correlation between experimental data and the CFD model precisely because the latter fails to capture some phenomena that affect the dynamics of the flow. This is confirmed already by some works previously carried out at the Jet Propulsion Laboratory, which is preparing to launch the Mars Helicopter Scout in 2020.

The correlation between the numerical model and the experimental test represents an important goal, since after having realized it, it will be possible to exploit the model setup in order to improve the blade performance through an optimization study.

In the second part of the work, the optimization code implemented by Domenico Zaza as the final work of his Bachelor Degree [36] has been used. The aim of the code is to optimize the shape of the blade, acting on the chord and pitch angle distribution. This type of optimization only affects the geometry of the blade and it does not concern the basic airfoil, which is assumed to be the same as that of the non-optimized blade used for the 3D model in the first part of the job.

In particular, this profile has already been analysed using the CFD by Marta Talmelli in her Master's Thesis [7] and with some changes (dictated by constructive needs) it has been used in the blade made for experimental tests.

Despite some rather forced hypotheses, it was decided to check the optimization tool to start testing a new blade geometry in a short time. As this could be a practical and fast solution for the creation of an optimized blade.

# Sommario

L'obiettivo di questa tesi è di trovare una correlazione tra i test sperimentali, eseguiti in camera a vuoto presso la sede di Torino di Thales Alenia Space Italia, con un modello CFD, per quanto riguarda un rotore funzionante in ambiente marziano.

Partendo da un semplice modello, si vanno via via ad aumentare i dettagli in modo da avvicinarsi il più possibile alla realtà e quindi al caso sperimentale. In fase di creazione della griglia viene utilizzato il software Gridgen, software distribuito da Pointwise, mentre nella fase di calcolo viene utilizzato il software CFD++ prodotto da Metacomp, Inc. Quest'ultimo software consente di specificare il moto della griglia. In particolare consente di operare con volumi rotanti a diverse velocità.

Come è intuibile, il fenomeno che si sviluppa all'interno della camera a vuoto è altamente instazionario e decisamente complesso. Per questo motivo non ci si aspetta una stretta correlazione tra i dati sperimentali e il modello CFD proprio perchè quest'ultimo non riesce a catturare alcuni fenomeni che influiscono sulla dinamica del flusso. Questo viene confermato già da alcuni lavori svolti in precedenza presso il Jet Propulsion Laboratory, che si appresta al lancio del Mars Helicopter Scout nel 2020.

La correlazione tra il modello numerico e il test sperimentale rappresenta un importante traguardo, poichè dopo averla realizzata, sarà possibile sfruttare il setup del modello per poter operare nell'ottica di migliorare le prestazioni della pala e quindi effettuare uno studio di ottimizzazione.

Come seconda parte del lavoro infatti si procede attraverso l'utilizzo di un codice implementato da Domenico Zaza [36] come prova finale della sua laurea triennale. Il codice è realizzato con lo scopo di ottimizzare la forma della pala, agendo su distribuzione di corda e angolo di calettamento. Questo tipo di ottimizzazione riguarda soltanto la geometria della pala e non riguarda invece il profilo alare di base, che viene assunto uguale a quello della pala non ottimizzata utilizzata per il modello 3D nella prima parte del lavoro.

In particolare, questo profilo è già stato analizzato con simulazioni CFD da Marta Talmelli nella sua tesi di laurea magistrale [7] e con alcune modifiche (dettate da esigenze costruttive) è stato utilizzato nella pala realizzata per i test sperimentali.

Nonostante alcune ipotesi piuttosto forzate, si è scelto di verificare il tool di ottimizzazione per incominciare a testare una nuova geometria di pala in breve tempo e perchè risulterebbe essere un modo pratico e veloce per la realizzazione di una pala ottimizzata.

# Nomenclature

$\alpha$	Angle of attack
$\delta_{ij}$	Kroeneker delta
$\dot{m}$	Mass flux
$\eta$	Blade efficiency
$\Gamma$	Circulation
$\gamma$	Intermittency
$\mu$	Dynamic viscosity
$\nu_t$	eddy viscosity
$\Omega$	Rotational velocity
$\omega$	Turbulent frequency
$\vec{n}$	Normal versor
$\vec{q}$	Velocity vector
$\phi$	Inflow angle
$\rho$	Density
$\theta$	Pitch angle
$\varepsilon$	Dissipation rate
$A$	Area
$B$	Tip loss factor
$c$	Chord
$C_d$	Drag coefficient
$C_L$	Lift coefficient

$D$	Drag
$d$	Diameter
$E$	Energy
$F$	Prandtl's coefficient
$f$	Frequency
$G$	Glauert's load parameter
$k$	Turbulent kinetic energy
$L$	Lift
$P$	Induced power
$p$	Static pressure
$Q$	Blade's torque
$R$	Gas constant
$R$	Radius
$r$	Radial coordinate
$Re$	Reynolds number
$Re_\theta$	Momentum-thickness Reynolds number
$S$	Surface
$St$	Strouhal number
$T$	Static temperature
$T$	Thrust
$t$	Time
$T/A$	Disk loading
$u^+$	Adimensional wall velocity
$V$	Velocity
$y^+$	Adimensional wall distance

# Acronyms

<b>BC</b>	Boundary condition
<b>BEMT</b>	Blade Element Momentum Theory
<b>CFD</b>	Computational Fluid Dynamics
<b>CFL</b>	Courant-Friedrichs-Lewy
<b>CNES</b>	Centre National d'Etudes Spatiales
<b>DNS</b>	Direct Numerical Simulation
<b>ESA</b>	European Space Agency
<b>FM</b>	Figure of Merit
<b>JPL</b>	Jet Propulsion Laboratory
<b>LES</b>	Large Eddy Simulation
<b>LEV</b>	Leading Edge Vortex
<b>LSB</b>	Laminar Separation Bubble
<b>MAV</b>	Micro Air Vehicle
<b>MAVEN</b>	Mars Atmospheric and Volatile Evolution
<b>MGS</b>	Mars Global Surveyor
<b>MHS</b>	Mars Helicopter Scout
<b>MOLA</b>	Mars Orbiter Laser Altimeter
<b>MRO</b>	Mars Reconnaissance Orbiter
<b>NASA</b>	National Aeronautics and Space Administration
<b>RANS</b>	Reynolds Averaged Navier-Stokes equation
<b>SST</b>	Shear Stress Transport

**TAS-I**      Thales Alenia Space Italia

**UAV**        Unmanned Air Vehicle

# Contents

<b>Summary</b>	III
<b>Sommario</b>	IV
<b>Nomenclature</b>	V
<b>List of Tables</b>	XI
<b>List of Figures</b>	XII
<b>1 Introduction</b>	1
1.1 Mars . . . . .	3
1.1.1 Atmosphere . . . . .	3
1.1.2 Topography . . . . .	4
1.1.3 Low-Reynolds number flow . . . . .	6
1.2 Drone system . . . . .	9
1.2.1 Preliminary conclusions . . . . .	10
1.3 Related works . . . . .	12
1.4 Thesis organization . . . . .	13
<b>I Correlation with experimental results</b>	<b>15</b>
<b>2 CFD analysis of rotor in free flight condition</b>	<b>17</b>
2.1 Step 0: Calculations with existent grid . . . . .	18
2.1.1 Geometry and Grid . . . . .	18
2.1.2 Calculation setup . . . . .	19
2.1.3 Results . . . . .	20
2.2 Step 1: CAD improvements . . . . .	23
2.2.1 Results . . . . .	24
2.3 Step 2: Vacuum chamber atmosphere . . . . .	25
2.3.1 Results . . . . .	25

<b>3</b>	<b>CFD analysis of rotor in vacuum chamber-like grid</b>	<b>29</b>
3.1	Step 1: Modification of the domain dimensions . . . . .	29
3.1.1	Geometry and grid . . . . .	29
3.1.2	Calculation setup . . . . .	30
3.1.3	Results . . . . .	30
3.1.4	First turbulence model benchmark . . . . .	33
3.2	Step 2: Introduction of unstructured blocks . . . . .	35
3.3	Step 3: Extension to full rotor . . . . .	37
3.3.1	Results . . . . .	38
3.4	Step 4: Introduction of asymmetric elements . . . . .	38
3.4.1	Turbulence model benchmark . . . . .	41
3.4.2	Transient simulations . . . . .	42
3.4.3	Results . . . . .	44
<b>II</b>	<b>Aerodynamic optimization</b>	<b>49</b>
<b>4</b>	<b>Blade Optimization</b>	<b>51</b>
4.1	Momentum theory . . . . .	51
4.2	Blade Element Theory . . . . .	55
4.3	Rotor model . . . . .	58
4.3.1	2D CFD simulations . . . . .	59
4.3.2	Simulation setup . . . . .	61
4.4	Results . . . . .	63
4.5	Vortex theory . . . . .	64
4.5.1	Wake structure for optimum rotor . . . . .	67
4.5.2	Prandtl's tip correction . . . . .	68
4.6	Optimization . . . . .	69
4.6.1	Rotor model . . . . .	70
4.6.2	3D model . . . . .	72
<b>5</b>	<b>Conclusions</b>	<b>79</b>
<b>A</b>	<b>Structured and Unstructured grids</b>	<b>81</b>
<b>B</b>	<b>Experimental setup</b>	<b>85</b>
B.1	Results . . . . .	88
<b>C</b>	<b>CFD solver</b>	<b>91</b>
C.1	Rotating grids . . . . .	93
C.2	Turbulence . . . . .	94
C.3	Boundary layer . . . . .	99
	<b>Bibliography</b>	<b>103</b>

# List of Tables

1.1	<i>Atmospheric parameters of the two planets[12]. . . . .</i>	11
2.1	<i>Schematic of the boundary condition imposed. . . . .</i>	20
2.2	<i>Forces developed by a single blade. . . . .</i>	20
2.3	<i>Results obtained from the grid convergence test. . . . .</i>	24
2.4	<i>Comparison between CO<sub>2</sub> and air atmosphere results. . . . .</i>	26
3.1	<i>Resume of the boundary conditions characteristics. . . . .</i>	30
3.2	<i>Turbulence model comparison. . . . .</i>	34
3.3	<i>Results comparison between full structured and hybrid grid. . . . .</i>	36
3.4	<i>Results obtained with different turbulence models. . . . .</i>	42
3.5	<i>Summary of the results obtained in all the simulations. . . . .</i>	48
4.1	<i>Reynolds number and set up parameters for the different sections. . . . .</i>	60
4.2	<i>Results obtained with different optimized blades. . . . .</i>	76
4.3	<i>Percentage performance improvement compared to the first optimized blade. . . . .</i>	76
4.4	<i>Rotor model results. . . . .</i>	77
C.1	<i>Constant used in <math>k - \epsilon</math> turbulence model. . . . .</i>	98
C.2	<i>SST turbulence model constants. . . . .</i>	99

# List of Figures

1.1	<i>Comparison between Earth and Mars atmosphere. [2]</i>	4
1.2	<i>Mars topographic map. [3]</i>	5
1.3	<i>Schematic showing the structure of a laminar separation bubble.</i>	6
1.4	<i>Comparison of the leading edge vortex behaviour between two (A) and three (B) dimensional flow models.[24]</i>	7
1.5	<i>Stable attachment of the leading edge vortex.[24]</i>	8
1.6	<i>Examples of different rotor configurations.</i>	9
1.7	<i>Sum up of some results obtained by Maryland university.[18]</i>	13
2.1	<i>CAD models of a single blade and of the complete rotor.</i>	18
2.2	<i>Visualization of the grid database, the hub is modelled as a half-cylinder starting from far upstream and finishing far downstream of the blade.</i>	19
2.3	<i>Results of the first simulation.</i>	21
2.4	<i>Visualization of the velocity field along the z-axis.</i>	21
2.5	<i>Pressure distribution along the upper part of the blade.</i>	22
2.6	<i>Pressure distribution along the lower part of the blade.</i>	22
2.7	<i>Visualization of the new implemented grid with the new database (in red).</i>	23
2.8	<i>Visualization of the Leading Edge Vortex.</i>	25
2.9	<i>Visualization of the new grid with extended domain under the blade.</i>	26
2.10	<i>Visualization of the velocity z-component field.</i>	27
2.11	<i>Visualization of the flow stream traces for different sections in the blade span wise direction.</i>	28
3.1	<i>Visualization of the vacuum chamber-like grid.</i>	30
3.2	<i>Comparison between the free flight and the vacuum chamber flowfield and velocity magnitude distribution.</i>	31
3.3	<i>Visualization of the three dimensional flowfield.</i>	31
3.4	<i>Pressure distributions comparison.</i>	32
3.5	<i>Visualization of the flow stream traces for different sections in the blade span wise direction.</i>	33
3.6	<i>Flowfield near the blade: the interaction with the swirling wake component is evident in particular near the hub.</i>	34
3.7	<i>Visualization of the flow stream traces for different turbulence models.</i>	35
3.8	<i>Visualization of the structured layers near the vacuum chamber wall.</i>	36
3.9	<i>Visualization of the residuals for two different simulations.</i>	37
3.10	<i>Full rotor grid.</i>	37

3.11	Visualization of the pressure distribution on the complete rotor. . . . .	38
3.12	Visualization of the two grid blocks concatenated, the inner cylinder is the one with motion. Here the lower part of the grid is not displayed. . . . .	39
3.13	Pressure field in the vacuum chamber. . . . .	40
3.14	Visualization of the new mesh elements (in blue). . . . .	41
3.15	Flow visualization for the different turbulence models. . . . .	43
3.16	Forces developed by the blade. . . . .	45
3.17	Forces developed by the blade in the case without the two cylinders and the blade. . . . .	46
3.18	Flow evolution on the upper part of the blade. . . . .	47
4.1	Schematic representation of the momentum theory model.(draw adapted from [34])	52
4.2	Schematic of the extended momentum theory, the swirl component is depicted in blue. (Draw adapted from [34]) . . . . .	54
4.3	Schematic of the blade section. (Draw adapted from [34]) . . . . .	56
4.4	Effect of tip loss. (Draw adapted from [34]) . . . . .	58
4.5	Grid constructed for the two-dimensional simulations. . . . .	60
4.6	Results of the 2D CFD simulations for the mean section ( $Re = 4.22e^3$ ). . . . .	61
4.7	Grid constructed for the rotor model simulation. . . . .	62
4.8	Residuals of the simulation which did not converge. . . . .	64
4.9	Velocity field for the rotor model simulation with the non-optimized blade. . . . .	64
4.10	Vortex theory for the actuator disk (Draw adapted from [34]) . . . . .	66
4.11	Matlab program outputs. . . . .	71
4.12	Velocity field of the optimized rotor model. . . . .	72
4.13	Grid constructed with the new optimized blade. . . . .	73
4.14	Pressure distribution on the optimized blade. . . . .	74
4.15	Comparison between the new and the non-optimized blade. . . . .	75
4.16	Pressure distribution on the optimized blade with a different pitch angle distribution. . . . .	75
4.17	Leading edge vortex on the optimized blade. . . . .	77
A.1	Example of a structured C-type mesh around an airfoil[8] . . . . .	81
A.2	Example of an unstructured mesh around an airfoil[8] . . . . .	82
A.3	Example of a hybrid mesh around an airfoil[14] . . . . .	83
B.1	PHASE vacuum chamber dimensions.[20] . . . . .	85
B.2	Experimental test setup dimensions.[20] . . . . .	86
B.3	Suspended setup within the vacuum chamber.[21] . . . . .	87
B.4	Schematic representation of the setup components.[21] . . . . .	87
B.5	Results of the first experimental test. . . . .	89
C.1	Schematic of the energy cascade process. . . . .	97
C.2	Universal wall law. . . . .	100



# Chapter 1

## Introduction

In the last 50 years, the planetary exploration has been focusing more and more on Mars. This because Mars is the closest planet to the Earth and for this reason it has the closest characteristics to the Earth ones than any other planet of the solar system.

The first missions were about discovering and studying the geology of Mars and its evolution, then the attention was focused on the research of sign of life on the planet, such as water.

Nowadays the main goal is to analyse the possible risks of Martian environment in order to prepare for the human exploration.

So far, all these tasks up to now have been performed by orbiters, rovers and landers. Each of these devices has advantages and disadvantages:

- *Orbiters* can observe a large portion of the planet but they have limits in the image resolution due to the great distance from the Martian ground;
- *Rovers* have a wide (compared to orbiters) resolution, as they actually stay on the ground, but their movement is limited by many factors such as surface obstacles or the batteries' autonomy;
- *Landers* can get a very high image resolution but their field of view is limited to a single location.

The NASA Mars Exploration Program (MEP) represents a huge effort to explore the planet started in 1993, during these years gave (and still gives) a huge contribution to Mars exploration. Thanks to this program, many rovers, landers and orbiters were sent to Mars. The *Odissey* Mars orbiter was launched in 2001 and it is still operating: its mission was to trace a first map of the chemical elements that populate the Martian atmosphere, at the same time its mission aimed at detecting water and ice and studying the planet geology.

In 2005, Mars Reconnaissance Orbiter (MRO) was successfully launched. Its mission was to capture details of the Martian surface thanks to a very powerful camera in order to provide information about probable landing sites for future landers and rovers. Another orbiter was launched in 2014, NASA's MAVEN (Mars Atmospheric and Volatile EvolutionN), with the aim of studying the red planet atmosphere and its evolution through time.

While talking about rovers, NASA sent *Opportunity* and *Spirit* as a double mission in 2004

(they were sent in two different landing sites), but *Spirit* lost communication with Earth in 2010, while communications with Opportunity had been lost in June 2018, due to a massive dust storm which covered the sky. The darkness combined with the dust deposited on the solar panels could have blocked the recharging of the batteries. In 2012 the rover *Curiosity*, the largest and most capable rover ever sent to Mars, landed on the planet to find out evidence of past habitable environment on Mars [3]. Recently (26th November 2018), NASA successfully landed *InSight* (Interior Exploration using Seismic Investigation, Geodesy and Heat Transfer) on Mars. InSight is a lander that means it is a static device whose goal is to study the internal structure of the planet to reconstruct the history of Mars. It is equipped with a seismometer to take measurement of the "marsquakes" and other internal activities on Mars. This device will also investigate how the Martian crust and mantle respond to the effects of meteorite impacts. As the acronym suggests, InSight is also equipped with a heat flow package, made of a self-penetrating heat flow probe. It is designed to burrow as deep as 5 m while trailing a tether with embedded heat sensors to measure how efficiently heat flows through Mars' core. However NASA is not the only agency sending spacecraft towards Mars, also ESA (European Space Agency) and Roscosmos (Russian space agency) give a relevant contribution to Mars exploration. In 2003, Mars Express Orbiter was the first planetary mission launched by ESA with the objective of collecting images of the planet's surface and determining atmosphere composition and structure. Another important mission set by ESA in collaboration with Roscosmos is *ExoMars*, which is divided in two parts:

1. The first part started in 2016 and is composed by two elements: TGO (Trace Gas Orbiter) and EDM (Entry, Descent and Landing Demonstrator Module)-*Schiaparelli*. The TGO searches for evidence of methane and other gases that could indicate active geological processes and will serve as data relay for the second part of the mission. The *Schiaparelli* lander failed to land softly and crashed, its aim was to demonstrate the possibility to perform a controlled landing on Mars' surface;
2. The second part will start in 2020 with the landing of a rover on the Martian surface. It will be able to collect samples with a drill and analyse them [2].

A very important contribution to Mars exploration is given also by SpaceX, a private company founded in 2002 by Elon Musk. Their plan is to send the first cargo mission on Mars in 2022 to confirm water resources and put in place initial life support infrastructure. This mission will be followed by a second one in 2024 with cargo and crew, with the main goal to build a propellant depot. This is an ambitious plan that will surely give a boost to the aerospace industry dominated by national and international agencies so far [4]. To have an idea of how difficult the Mars exploration is, it is sufficient to look at the information coming from NASA's *Opportunity* and *Curiosity* rovers, the most active on martian surface, landed respectively in 2004 and 2012. The rovers in these years have done slightly more than 60 Km, a really small distance compared to the extension of Mars' surface.

Given these facts it is logical to think about an alternative way to explore Mars. A wide range of rotorcrafts has been valued considering the weight, the range and the dimensions [5]. In particular, considering the roughness of the Martian surface a small rotorcraft can take off and land in a small area or can help the rover to predict the path to follow in order to avoid hazard that could affect the correct functioning of the rover. A small rotorcraft would have a limited

operational radius but this would be in any case greater than the rover autonomy. Finally it is clear that an Unmanned Air Vehicle (UAV) would be a good way to improve the mobility on Mars and at the same time to maintain a good image resolution.

## 1.1 Mars

Often called "the red planet", due to the iron oxide in its soil, Mars is the fourth planet from the Sun, about 142 million miles (193 million kilometres) of distance, and is the second smallest planet after Mercury. Mars is a terrestrial planet<sup>1</sup>, its diameter is about half of the Earth's one, but its surface area is quite the same of the total area of Earth's dry land. Furthermore, being less dense, Mars has 11% of Earth's mass and 15% of Earth's volume. As a consequence, Mars' gravitational acceleration is less than a half of Earth's one, just  $3.7 \text{ m/s}^2$  compared to  $9.81 \text{ m/s}^2$ . It has two moons, *Phobos* and *Deimos*, which have respectively 22 km and 12 km of diameter and orbit close to the planet.

As Earth, Mars spins around a tilted axis, while orbiting the Sun. The revolution about its own axis, the Martian solar day, or Sol, lasts about 24 hours and 40 minutes, while 687 days are needed to complete the orbit around the Sun. Given a similar axial tilt and a revolution period about twice the Earth's one, Mars has seasons like Earth, but they last twice.

### 1.1.1 Atmosphere

Mars lost its liquid metal core due to very low mass and its thermal capacitance. This made Mars unable to generate its magnetosphere billions years ago, so the solar wind interacts directly with the Martian ionosphere, lowering the atmospheric density by stripping away atoms from the outer layer.

The atmosphere is composed mostly of carbon dioxide, nitrogen, argon and traces of oxygen and carbon monoxide (figure 1.1).

Mars has the largest dust storms in the Solar System, reaching speeds of over 160 km/h. These can vary from a storm over a small area, to gigantic storms that cover the entire planet, they tend to occur when Mars is closest to the Sun. Atmospheric temperature is strongly influenced by dust: when the planet is in the closest position to the Sun, dust storms are stronger and the absorption of solar radiation by dust increases the daily mean temperature and diurnal temperature range above the surface [6]. Lifting and transport of dust produce non-uniform surface erosion and deposition that have substantially modified the surface of Mars over the past four billion years.

The air temperature can vary from a lows of about  $-143^\circ\text{C}$  at the winter polar caps, to highs of up to  $35^\circ\text{C}$  in equatorial summer. The wide range in temperatures is due to the thin atmosphere which cannot store much solar heat, the low atmospheric pressure, the low thermal inertia of Martian soil and, as previously said, to the dust concentration.

Atmospheric pressure goes from 30 Pa (0.3 mbar) on *Olympus Moon* to over 1155 Pa (11.55

---

<sup>1</sup>A planet composed primarily of silicate rocks or metals. Within the Solar system, also Mercury, Venus and the Earth belong to this planet type.

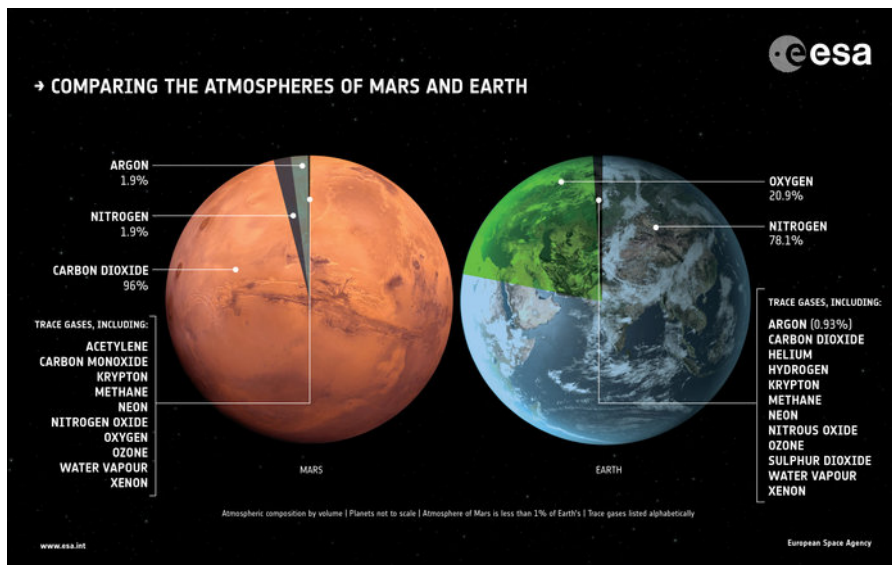


Figure 1.1: Comparison between Earth and Mars atmosphere. [2]

*mbar*) in *Hellas Planitia*. The highest atmospheric density on Mars is equal to the one found at 35 km above Earth's surface. The resulting mean surface pressure is only 0.7% of Earth's one.

As a consequence of low atmospheric temperature and low pressure, the average air density is low too, about  $0.0167 \text{ Kg/m}^3$  (more or less 1% of the Earth's air density). The really low atmosphere density means that in order to generate a reasonable lift from a wing (fixed or rotatory), it is necessary to have a higher speed or larger surfaces, with respect to terrestrial ones. At the same time, a lower value of the speed of sound<sup>2</sup> on Mars leads to a higher Mach number<sup>3</sup> and so the sonic/transonic flight condition can be reached easily. The break of the sound barrier has detrimental and dangerous effects on the aerodynamic and on the structure of the wing. On the contrary, the different air composition has not a specific effect on the drone's behaviour and efficiency.

### 1.1.2 Topography

As a consequence of the dust erosion and due to the numerous asteroid strikes, Mars' topography presents really exotic features: as shown in figure 1.2<sup>4</sup> there are important height variation of the terrain. Earth's Grand Canyon and Mount Everest are impressive, but they turn out to

<sup>2</sup>Defined as  $a = \sqrt{\gamma RT}$ , where  $\gamma$  is the specific heat ratio,  $R$  is the gas constant and  $T$  the gas temperature.

<sup>3</sup>Defined as  $M = v/a$ , where  $v$  is the wing velocity and  $a$  is the speed of sound.

<sup>4</sup>Captured by Mars Orbiter Laser Altimeter (MOLA), one of the five instruments on the Mars Global Surveyor (MGS) spacecraft, which operated in Mars orbit from September 1997 to November 2006.

be very small next to *Valles Marineris*<sup>5</sup> and *Olympus Mons*<sup>6</sup>. There are two types of regions divided by a ridge of mountains. To the north are lowlands, whose topography has been shaped by lava flows that have made the surface smooth. The south, on the contrary, is mountainous, with many meteorite impact craters, some of which are enormous.

The plains of Mars fall into two categories, the *planitiae* and the *maria*:

- *Maria*: although there is no water on Mars, some regions are called *maria* ("seas" in Latin), because the first astronomers believed they were under water. Actually their surface is covered by stones, which make them appear darker.
- *Planitiae*: lighter vast area thought to be covered in dust and sand rich in iron oxide.

Strong winds that blow the sand and dust around can change the configuration of these dark and light zones. It is clear that the use of a drone is the best way to overcome this problem, as it only needs a large enough flat spot to land, whose extension depends only by the UAV's size. A few words must be spent for the gravitational field of the red planet: due to the different

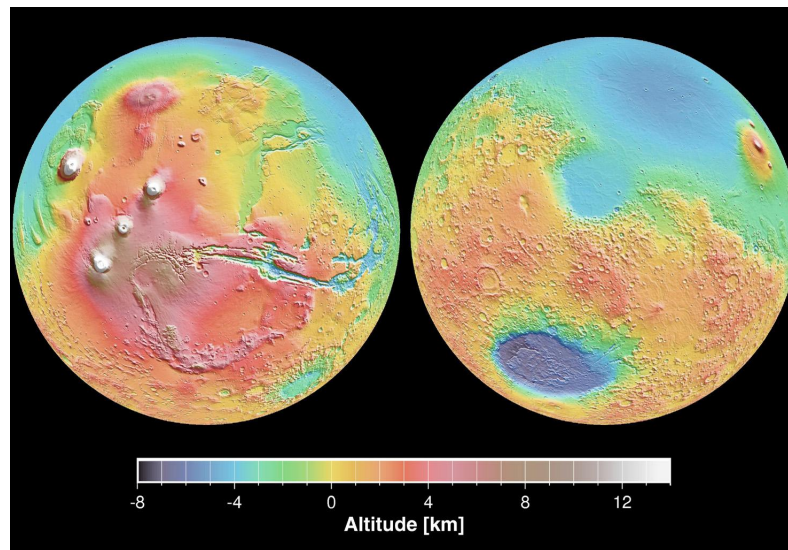


Figure 1.2: *Mars topographic map.* [3]

terrain altitudes which can be reached, it is not uniform across the planet.

A lower gravitational force means that a drone which is too heavy to flight on Earth can flight on Mars, because less lifting force is needed to take off; in other words it can be said that less lifting force is needed to fly on Mars.

<sup>5</sup>Is about four times deeper and nine times longer than the USA's Grand Canyon with a subsystem of smaller canyons that extend over more than a fifth of the planet's surface. This canyon is the largest one in the solar system as well.

<sup>6</sup>A 27 km high mountain, the tallest one known to exist anywhere in the solar system.

### 1.1.3 Low-Reynolds number flow

The main issue of flying on Mars is represented by the atmospheric characteristics; it is possible to estimate the Reynolds number flow which invests the blade of the rotor.

$$Re = \frac{\rho l V}{\mu} = \frac{0.0167 \cdot 0.05 \cdot 72}{1.04 \cdot 10^{-5}} \simeq 5800 \quad (1.1)$$

With  $\rho$  as fluid density,  $l$  as reference length (the chord profile in this case),  $V$  as velocity of the flow and  $\mu$  as dynamic viscosity it is possible to have a first estimation of the blade's Reynolds number.

The velocity considered is the one expected at the tip of the blade: it is clear that the  $Re$  value is very low compared to the ones typically encountered in aeronautical applications ( $\simeq 10^7$ ). This fact leads to a particular flow regime in which viscous forces have a more important role compared to the inertial ones. Consequently, boundary layer physics and the related flow separation/re-attachments zones change.

An important characteristic of this flow regime is the *Laminar Separation Bubble* (LSB). To be fair, this bubble does not generate itself only in this flow regime, it is also present in more conventional flows ( $Re > 500000$ ). Considering an airfoil, the laminar flow over the upper airfoil surface is subjected to an adverse pressure gradient near the leading edge. The flow separates due to the lower kinetic energy of the laminar boundary layer, then gains momentum from the free-stream and reattaches as a turbulent boundary layer, creating the LSB<sup>7</sup> [22]. As the turbulent boundary layer is energized by the free-stream, it remains attached to the wall till the trailing edge (figure 1.3). At lower Reynolds numbers ( $50000 < Re < 100000$ ), the

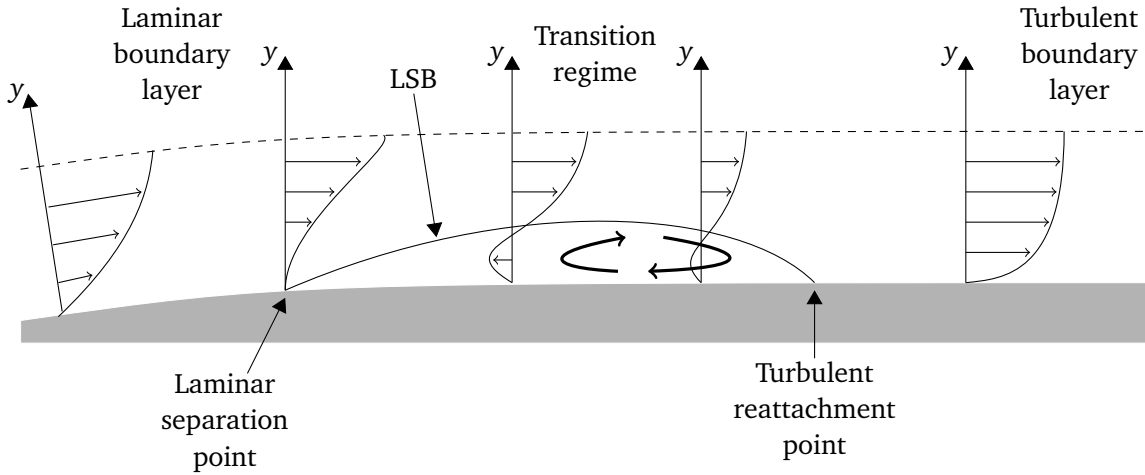


Figure 1.3: Schematic showing the structure of a laminar separation bubble.

separation bubble increases in dimensions with the boundary layer thickness, increasing the

<sup>7</sup>LSBs are caused by the inability of the flow to make a transition to turbulent flow in the attached boundary layer on the surface of the airfoil; the laminar flow separates before transition.

drag. Despite this fact, the boundary layer still gains enough momentum from the free-stream and reattaches to the airfoil surface. Decreasing a bit more the Reynolds number ( $\sim 10^4$ ), the laminar separation point is delayed until a position near the trailing edge due to the increased stability of the boundary layer which is more resistant to flow transition. In this case, however, the shear layer is unable to reattach on to the airfoil as a turbulent boundary layer and causes a drag increase and lift decrease. The trailing edge separation increases in size as the Reynolds number decreases, affecting the airfoil efficiency [23].

### Leading Edge Vortex

In many engineering works and applications the study starts from the observation of what is provided by nature, in this case the low-Re flows are related to the aerodynamics of insects ( $Re \sim 10^2 \div 10^3$ ). Physicists and biologists conducted many studies on the flow that involves insects wings. One of the characteristic encountered that developed so much attention is that at high angles of attack, a prominent leading edge vortex (LEV) remains stably attached on the insect wing and does not shed into an unsteady wake, as would be expected [24]. Its presence enhances considerably the forces generated by the wing, enabling insects to hover or maneuver.

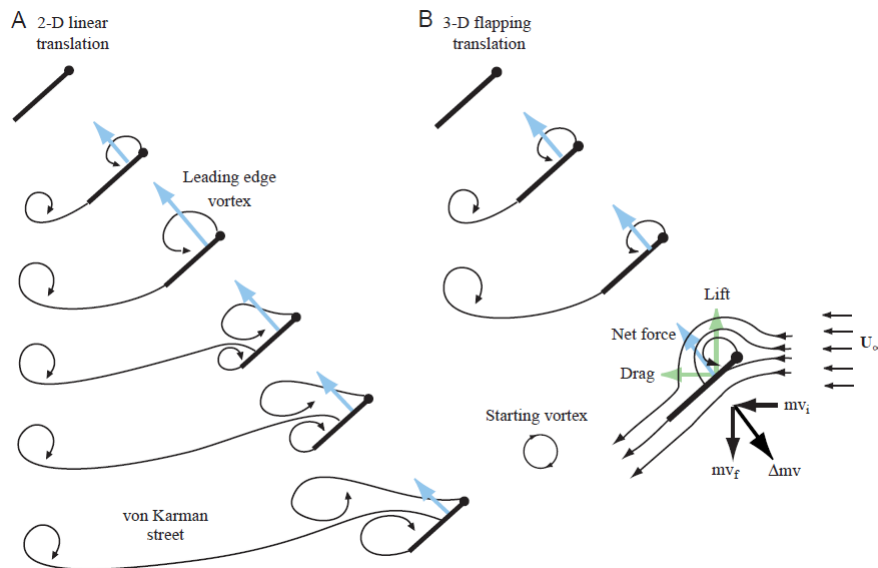


Figure 1.4: Comparison of the leading edge vortex behaviour between two (A) and three (B) dimensional flow models. [24]

Considering a 2D flow case, at high angles of attack, the fluid going over the wing separates as it crosses the leading edge but reattaches before reaching the trailing edge. In this case the wing translates at a high angle of attack so a greater downward momentum is transmitted to the fluid giving a improvement in terms of lift developed. This vortex is probably the most important feature that allows the insect to fly.

For airfoils with sharp leading edge the flow separates at the leading edge causing the formation of a vortex: a suction force is developed normal to the plane of the wing, enhancing the lift component. *In this case the resultant force is perpendicular to the plane of the wing and not to the ambient velocity, thus drag also is increased* [25].

If the wing continues to translate at high angles of attack, the leading edge vortex grows in size until flow reattachment is no longer possible. Vorticity forms at the trailing edge creating a *trailing edge vortex* as the leading edge vortex sheds into the wake, in this condition there is a drop in lift and the wing have stalled. As this last vortex detaches, a new leading edge generates: this procedure repeats creating a wake of spaced counter-rotating vortices known as *von Karmann vortex street*. All this process in which the wing is alternatively stalled is called *delayed stall*.

However, it has been observed in 3D models by *Ellington et al.* in [26] that for Reynolds numbers in the range of  $10^3$  the leading edge vortex was not shed and thus the von Karman vortex street was not created, as a consequence wing did not stall (figure 1.4).

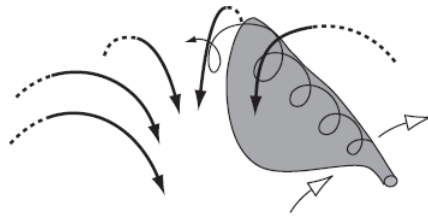


Figure 1.5: *Stable attachment of the leading edge vortex.*[24]

The reason of this behaviour is a steady span-wise flow from the wing hinge to about 75% of the wing extension, where the vortex detaches from the wing surface (figure 1.5). This flow is entrained by the leading edge vortex, causing it to spiral to the tip of the wing. Then, the span-wise flow is useful as it maintains stable attachment of the leading edge vortex, a similar vortex is stabilized by an axial flow generated due to the back-sweep of wing in delta aircraft. The flow reduces the momentum from the chordwise direction, causing the leading edge vortex to remain smaller: a smaller vortex allows the fluid to reattach more easily and the wing can sustain this reattachment for a longer time.

At first glance, one could think laminar separation bubble and leading edge vortex are two different phenomena. Actually they represent the same phenomenology but in different situations: the leading edge vortex in fact is typical of ultra-low Reynolds number flow ( $\sim 10^2$ ) while one can find the laminar separation bubble even in flows at  $Re \sim 10^5$  or more. Furthermore, given the span wise flow that allow the LEV to be attached to the body, the LEV is a typical 3D effect that cannot be captured by 2D simulations. In literature there are very few works dealing with 3D computations so it is easier to find references to the LSB than to the LEV.

## 1.2 Drone system

Drones are Unmanned Aerial Vehicles that can be remotely controlled. They can have very different functions depending on the shape and on the dimensions. Small drones can take off and land in narrow and unprepared sites, acquire small samples of soil and rocks and perform high-risk tasks. On the other hand, they have a limited range of flight. Large drones have a greater operating range and can carry heavier payloads or instruments; but they consume a large quantity of energy and need a landing site preparation [5]. What needs to be taken into account for the drone design is also the blade configuration. Depending on the dimensions a drone can have coaxial counter-rotating rotors or four separated rotors or even eight rotors.

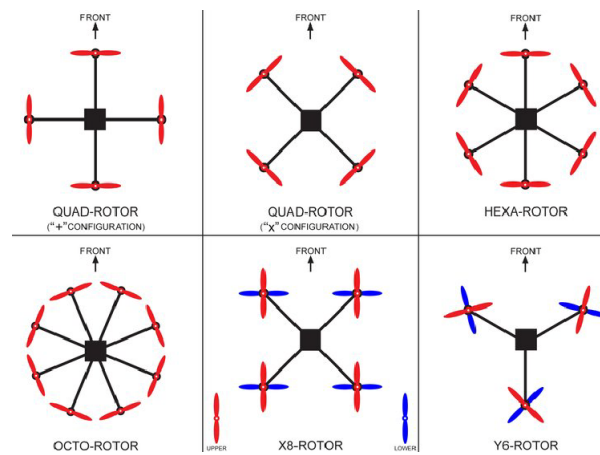


Figure 1.6: Examples of different rotor configurations.

Drones are composed by different subsystems:

- **Propulsion system:** this system produces the force needed to fly. Rotors (and as a consequence blades), motors and transmission line form this subsystem. In this system is included also the aerodynamic design, as the blade needs to have the best geometry to grant the maximum thrust and requires the minimum power. In this project in particular, the aerodynamic efficiency is an important driver of the whole design as, once the blade geometry has been decided, all the other aspects of the drone such as structure and power system can be implemented.
- **Power system:** the main goal of this system is the production, the storage and the distribution of power needed by the motors to produce thrust. The weight is a critical aspect of the whole project because, given the low air density it is harder to develop a consistent thrust. It is also true that, even if less thrust is required, it is critical to have the lightest component that maximize the payload, so the motors need to be small and light. Linked to the weight issue there is the torque needed to move the blade: the torque must be kept as low as possible because the higher is the torque needed the higher is the weight of the motor needed.

- Thermal control system: this system includes all the devices needed to control the operating and non operating temperatures of the drone components. Considering the mission type, thermal system will be a fundamental part of the drone:
  - There is a critical diurnal temperature excursion, this cycle of temperature can damage the structure of the drone.
  - Temperature is very low so the critical components must be sufficiently insulated. On the other hand, heat generated by the motor must be dissipated. This fact can be worsened by the diurnal excursion, as temperature can rise by several degrees.
  - The very low density of the atmosphere causes the convection to be ineffective. As a consequence heat must be dissipated by conduction and radiation.
- Structural system: is the structure itself. The structure must resist to all the load applied in order to protect the other subsystems. The investigation relative to the materials to use to build the structure and the mass distribution analysis are part of this subsystem.
- Guidance, Navigation and Control (GNC) system: usually it is a computer which includes accelerometers, gyroscopes and altimeter to determine drone location and path.
- Avionic and communication systems: these two systems are linked to one other because the first includes a computer which can collect and store data while the second is necessary to transmit them to the ground station so that post-processing can be performed.
- Payload: it represents the extra weight the drone can transport and it can include very different instruments depending on the mission the drone has to accomplish. Usually a high resolution camera is always included in the payload because it allows to know the terrain conformation and to spot landing sites. For an exploration mission it is a must-have device.

Micro Air Vehicle (MAV) are small UAVs used for surveillance, search and rescue operations, scientific research and other terrestrial applications. As their dimensions are really limited they operate in the low-Reynolds number range. For this reason they are the terrestrial UAVs the closer to the Mars drone and some of the designing processes and features involved in their construction can be useful to the design of the Mars rotor. In fact they share the same aerodynamic characteristics, as the LSB which is surely the phenomenon that affects the most the flow around the blades.

### 1.2.1 Preliminary conclusions

The detrimental effects of Mars atmosphere on the drone have already been anticipated by discussing about the low density, the very strong winds and dust storms. The following 6 points can help to clarify the issues faced while designing:

1. The low density atmosphere is responsible for a larger blade surface or for a higher rotational speed to generate lift force. As a consequence the Reynolds number drops to very low values compared to the Earth atmosphere.

2. The low sound velocity causes to reach easily transonic and supersonic speeds especially at blade tip. Shock wave can affect the blade structure and the aerodynamic behaviour.
3. Strong wind and dust storms make necessary the need to have stabilization devices.
4. The rough terrain makes necessary the design of flexible legs or other devices for safe landings.
5. The very low temperature and the poor thermal exchange are dangerous for the avionic system and can determine the flight autonomy of the drone.
6. The formation of important laminar separation bubble and leading edge vortex on the airfoil upper surface influence the aerodynamic performance.

Starting from a quad-rotor configuration and considering that the drone realized by NASA's JPL weighs around 1.8 Kg, it can be assumed that the drone should weight about 2 Kg. For this reason the target thrust required to be developed by a single rotor is  $T_r = 0.5 \text{ Kg} \cdot 3.72 \text{ m/s}^2 = 1.86 \text{ N}$ , as the configuration chosen is a quad-rotor one. This is not the thrust expected from the blade considered in this work but it is target to accomplish in future optimization works. It is possible to make a comparison between the main features of the atmospheric parameters which are summarized in the table below (table 1.1).

	Earth ( $h = 0 \text{ Km}$ )	Mars ( $h = 0 \text{ Km}$ )	Earth ( $h = 35 \text{ km}$ )
Gravity [ $m/s^2$ ]	9.81	3.72	9.71
Mean temperature [ $K$ ]	288	213	216
Mean pressure [ $Pa$ ]	101300	730	890
Density [ $kg/m^3$ ]	1.225	0.0167	0.014
Dynamic viscosity [ $Pa\cdot s$ ]	$1.80 \cdot 10^{-5}$	$1.04 \cdot 10^{-5}$	$1.4 \cdot 10^{-5}$
Sound velocity [ $m/s$ ]	340	238	295
Constant heat ratio	1.4	1.29	1.4
Gas constant	287	192	287

Table 1.1: Atmospheric parameters of the two planets[12].

To this table has been added the column relative to the conditions of the Earth's *stratosphere*. This has been done because this particular part of the Earth's atmosphere has conditions very similar to the Martian ones. The main differences concern the gravity, the sound velocity and the gas constant. For these reasons *the aerodynamic study conducted in this work could be helpful also for the study of drone that could fly in the stratosphere*.

Thales Alenia Space is working on a stratospheric airship (20 km of altitude), called *Stratobus*, whose launch is expected in 2022. Its main purposes are [30]:

- Surveillance missions, including land, maritime, oil platform and piracy at sea;
- Environmental monitoring missions;
- Telecommunications (4G and 5G connectivity);

- Strengthen the AIS (Automatic Identification System) network in heavy traffic zones, improving traffic control.

As the airship is solar powered (and autonomous) it is not expected to land in short times, that is why a drone could help the technicians in monitoring the airship' structure condition or damages in order to verify if a repair is needed. Thanks to the small dimensions of the drone it could be stored in the airship and activated periodically to conduct inspections.

### 1.3 Related works

Concerning aerodynamics a few works have been published, most of them deals with numerical simulation of two and three dimensional flows around the blade [9], [10], [11], [12]. In particular in [9], [11] and [12] several investigation have been done on the rotor configuration, concerning how many blades need to be put in the rotor and which rotor configuration is the best (see figure 1.6 for some examples), which is the best airfoil for this particular flow regime (parametric studies have been done using XFOIL software, which use panel method, developed by M. Drela) and which is the best way to obtain a performance estimation (3D CFD model or *Blade Element Momentum Theory*, also called BEMT). In [13] it is important to note some discrepancies between the experimental tests and the CFD simulations.

Some experimental investigations have been done in order to simulate the low-Reynolds number atmosphere of Mars but the papers which can be found are even fewer than the ones related to the numerical investigations [15], [16], [17]. Maryland University contribution was fundamental in this research [18]: their rotor was developed by JPL to create the Mars Helicopter Scout (MHS). This rotor is the one modelled in the CFD simulations of this thesis and has been replicated in TAS-I in order to have a comparison term. In the latter paper it is possible to find the experimental procedures and results obtained. Two sets of studies were conducted:

1. Thrust and torque of the rotor were measured at the exact martian density ( $\rho = 0.0167 \text{ Kg/m}^3$ );
2. The performances were measured for different Reynolds numbers by varying the gas density.

The rotor was then investigated for different rotational speeds and collective pitch angles (figure 1.7). The results underline that the best configuration for this type of blade (which is a simple rectangular, untwisted blade) is a high-pitch one ( $30^\circ \sim 32^\circ$ ).

This grants a sufficient thrust and the best FM (*Figure of merit*), which is a parameter that allows to know whether a rotor is efficient or not<sup>8</sup>. It is useful to observe that, comparing the maximum FM obtained with rotors that operate on Earth difference is important, as the latter has a FM typically of  $0.7 \div 0.9$ .

The JPL's MHS is a co-axial counter-rotating rotors drone of about 1.1 m diameter.

---

<sup>8</sup>The *propeller efficiency* is defined as  $\eta_p = \frac{TV_\infty}{P}$ , where  $T$  is the thrust,  $V_\infty$  is the vertical velocity and  $P$  is power. In hovering condition  $V_\infty = 0$  so the efficiency's definition loses its meaning. To overcome this problem the *Figure of Merit*, FM, is introduced: it is defined as the ratio between the ideal induced power and the real one.

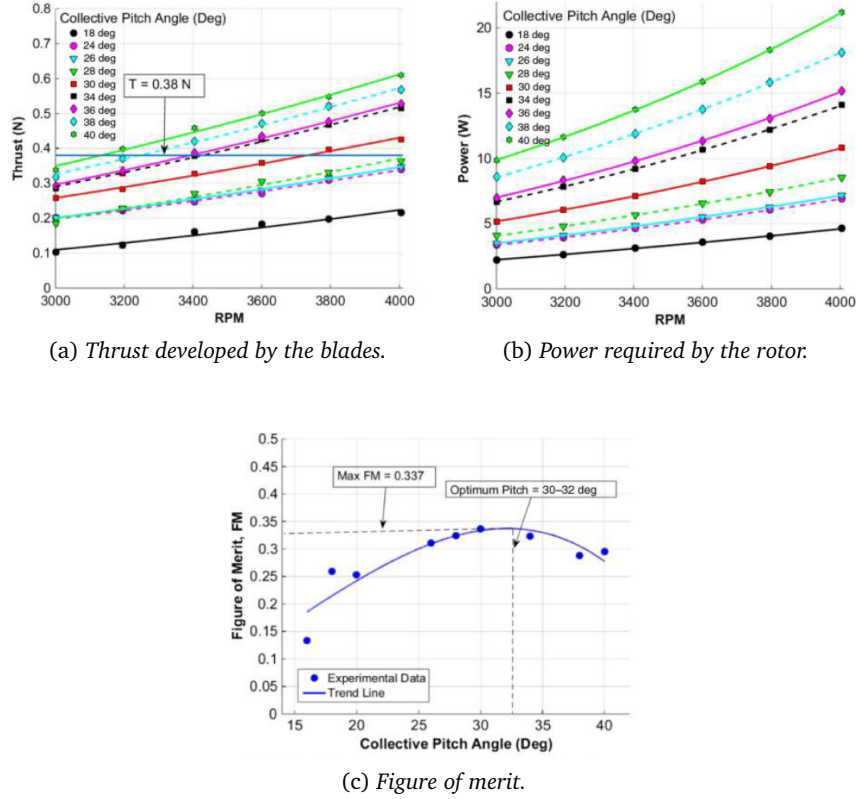


Figure 1.7: Sum up of some results obtained by Maryland university.[18]

It will be sent to Mars with Mars 2020 mission and it is expected to fly up to five times during its 30-day testing. It is solar powered and it can operate for a maximum of three minutes per day (due to the high temperatures developed by the motors), covering a range of 600 m and reaching a maximum altitude of 400 m.

Also the *Centre National d'Etudes Spatiales* (CNES) developed a Martian UAV called MOSQUITO (*Mars Original System for Qualitative Imaging and Tactical Operations*) following the guidelines given by the studies done by the University of Maryland and French universities [19]. Up to now, it has been developed a software to optimize the architecture of a multicopter drone flying on Mars and system analysis, as well as design and testing of several drone solutions.

## 1.4 Thesis organization

This work can be divided in two main parts: the first dealing with the implementation of a 3D model to simulate the experimental case and to compare with (Chapters 2 and 3), the second is a validation test for an optimization tools implemented by Domenico Zaza in his Bachelor Degree's final work [36] (Chapter 4).

The first part is an iterative process in which each iteration adds a level of detail, while the second part tries to find a proper geometry for the blade to improve the thrust, because the

blade examined in the first part does not give enough thrust to lift a reasonable weight. In particular the second chapter examines the *free flight* condition case, starting from an existing CAD and improving it to simulate both Martian and terrestrial environmental conditions. In the third chapter the grid is modified to obtain the vacuum chamber's dimensions and then some elements which make the model not symmetric are introduced. All these modifications are done to approach gradually the experimental case (some relevant informations can be found in Appendix B).

In the second part (the fourth chapter) new blade geometries are tested to find out how the optimization code works. It must be specified that this optimization involves only the blade chord and pitch angle distribution and it does not operate on the section, which remains the same of the previous blade.

There is anyway a link between the two sections, in fact once the new geometry is found, CFD simulations are performed in order to estimate how new blade can be more efficient.

Together with these 3D CFD simulation in which the blade is modelled, it is chosen to use also the *Rotor Model* option given by CFD++. This model uses the actuator disk theory with the BEMT theory to estimate the thrust of a rotor. It is an approximation but allows to have faster simulations and it is also verified the accuracy of this model.

Every simulation is performed with the realizable  $k-\varepsilon$  model which is as default in the CFD++ software and, according to Metacomp, is the more stable and robust turbulence model for a wide range of simulations. Anyway, other turbulence models are used in this work to have also an idea of how the turbulence modelling affects the calculations (see Appendix C for further theoretical informations about the different turbulence models used).

## **Part I**

# **Correlation with experimental results**



## Chapter 2

# CFD analysis of rotor in free flight condition

Starting from the work done by Marta Talmelli [7] in TAS-I, the study of the blade is extended to the third dimension. Following her work, a very thin and cambered profile is chosen to generate the blade, which has a very simple geometry: it is a rectangular blade, not twisted and without chord variations. The rotor considered in the following analysis is composed of two blades and a hub, whose geometry is approximated with a cylinder.

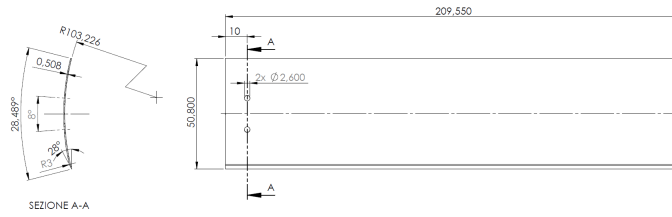
Before starting considering the full rotor (comprehensive of the two blades and of the hub), only half of the latter is considered. This choice is done because the grid implementation<sup>1</sup> and the calculation will be faster, as soon as this model gives good results in term of convergence and in term of forces, the full rotor will be implemented. The first step to be done is to build a database model on which the grid has to be constructed; starting from the CAD model (figure 2.3), it is necessary to eliminate the holes in the blade and the two supports which give the blade the pitch angle and to find an appropriate measure of the cylinder radius which will approximate the hub. The rotor geometry replicates as close as possible the geometry of the blade developed by Maryland University (figure 2.3):

- Rotor diameter = 18 in  $\simeq$  457 mm;
- Chord = 2 in  $\simeq$  51 mm;
- Camber = 6.35%;
- Thickness-to-chord (t/c) ratio = 1%;
- Blade pitch angle<sup>2</sup> = 32°.

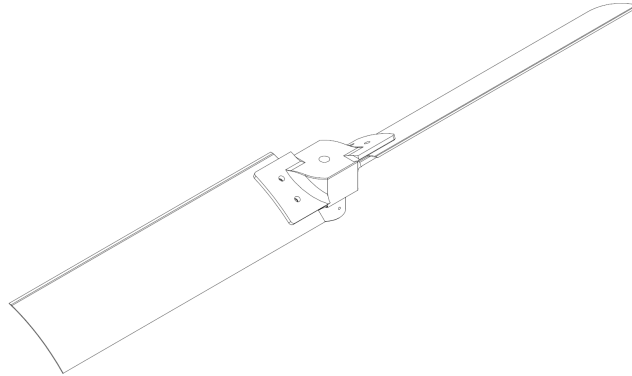
---

<sup>1</sup>The grid is realized with Gridgen®, a Pointwise.Inc. software.

<sup>2</sup>The hub has two fixed supports (not modelled) which allow to mount the blades, consequently the pitch angle is fixed.



(a) Blade geometry.



(b) Complete rotor geometry.

Figure 2.1: CAD models of a single blade and of the complete rotor.

One information that is worth to remember is that for the thesis work, the rotor will be considered in *hover* condition.

This means that the rotor has no velocity relative to the air both vertically and horizontally. The thrust developed is only the one necessary to the drone to lift itself, but with no velocity, so the thrust is coincident with the weight of the drone.

## 2.1 Step 0: Calculations with existent grid

At the beginning of the thesis work, a grid was already implemented. Even if the database (i.e. the CAD model) was not really accurate, the grid was used to start to understand how to set up the calculation.

### 2.1.1 Geometry and Grid

As it is possible to see from figure 2.2 the hub was modelled as a cylinder going from far upstream the blade to far downstream. The grid includes a large portion of fluid, this was made to simulate the condition of *free flight* for the blade. Talking about the blade it can be said that the latter is positioned with a side corresponding to the centre of rotation of the rotor. This is not truly representing the reality as the spacing for the hub must be taken into account, this will lead to a difference in terms of rotational speed at the tip of the blade. Consequently, as in this case is missing a portion of blade which faces a high velocity, the registered force

will be lower than the case in which the hub is taken into account. This because considering a blade's section, if the velocity encountered is low then the lifting force developed will be lower than the force developed by a section which sees a higher velocity, this can be immediately seen by the general formulation of lift

$$L = \frac{1}{2} \rho S V^2 C_L \quad (2.1)$$

where given the same conditions, density  $\rho$  and surface  $S$  ( the lift coefficient  $C_L$  depends from the Reynolds number which depends from the velocity), it is straightforward that if the velocity  $V$  increase then also the lift will increase.

The grid is all composed of structured blocks (see appendix A for further information about structured and unstructured grids): also for the next grids a structured configuration will be used, in order to have a faster convergence velocity and better numerical stability.

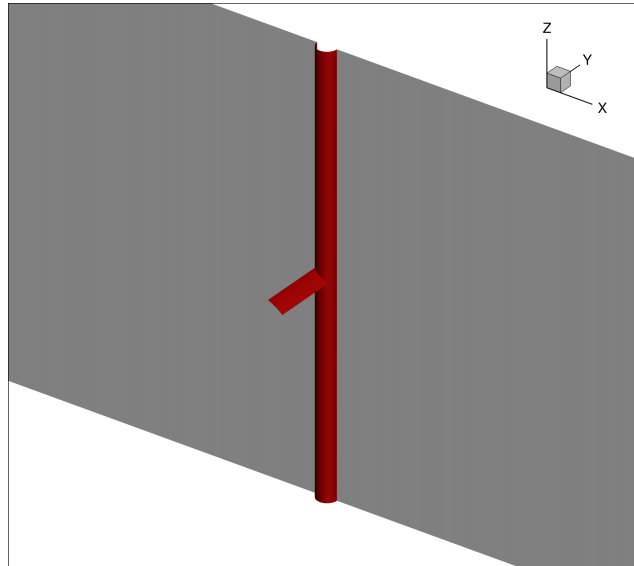


Figure 2.2: Visualization of the grid database, the hub is modelled as a half-cylinder starting from far upstream and finishing far downstream of the blade.

### 2.1.2 Calculation setup

The main goal of this section is to find out how to set the rotation of the grid in CFD++. Starting from the general informations about the setup, a steady state *laminar*<sup>3</sup> simulation is chosen. The fluid is a perfect gas, in particular  $CO_2$ , its temperature<sup>4</sup> is 215 K and its pressure  $790 Pa = 790 N/m^2$  (these are the initial conditions of the simulation).

<sup>3</sup>The choice of the turbulence model will be analysed later and further informations about turbulence and turbulence model can be found in Appendix C.

<sup>4</sup>Both temperature and pressure values are the static ones.

The next informations to be inserted are the boundary conditions, particular attention must be taken for the two boundaries which represent the symmetry plane: a zonal BC is used and in particular it is imposed a connection between these two boundaries after rotating them by  $180^\circ$  around the z-axis. As the interface region contains no overlaps and there are only face to face connections, the *patched only* option is selected. Concerning the hub and the blade, a wall BC is chosen, in particular the wall type is adiabatic (as no heat transfer is considered), viscous and stationary with the mesh motion. According to the latter characteristic, the hub and the blade rotate integrally with the grid. For the inflow and the farfield region, initial values of temperature and pressure are set, while for outflow region only the pressure is imposed. In table 2.1 all the boundary condition informations are resumed.

Bc	Bc type	Sub-group	Specification
Outflow	Open	Outflow only	Back pressure imposition
Inflow	Open	Inflow only	Pressure and temperature
Farfield	Open	Inflow and outflow	Static pressure and temperature
Hub	Wall	Viscous	Stationary with mesh motion
Blade	Wall	Viscous	Stationary with mesh motion
Periodic_1	Zonal	Patched only	Rotational, connected to Periodic_1
Periodic_2	Zonal	Patched only	Rotational, connected to Periodic_2

Table 2.1: Schematic of the boundary condition imposed.

The next step is to impose a grid motion, for this first case a rotation velocity of 3000 rpm is applied to all the groups; time integration is implicit and the spatial discretization is second order accurate.

### 2.1.3 Results

The absence of a turbulence model affected the calculations, which didn't converge. This could be expected due to the unsteady nature of the flow. For this reason another run is done considering this time a turbulence model, in particular the realizable  $k - \varepsilon$  model. The results obtained converged in a thousand of iterations and gave the results in table 2.2.

Z-force [N] (Thrust)	0.212
Z-moment[N](Torque)	0.018
X-force[N]	0.1176

Table 2.2: Forces developed by a single blade.

It must be specified that the thrust generated by the blade (z-force) considers only one blade, so the force (in the z-direction) and the torque must be doubled to obtain the force developed by the complete rotor<sup>5</sup>. According to these results the thrust produced by the complete rotor

<sup>5</sup>In the complete rotor, the x-force is zero because each blade develops a x-force of the same intensity of the other one but directed in the opposite direction.

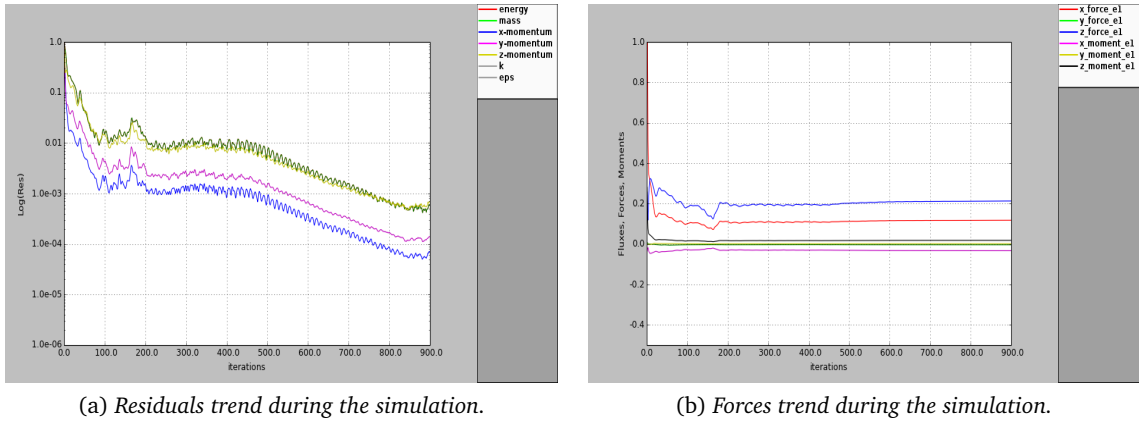


Figure 2.3: Results of the first simulation.

is 0.424 N; as it can be seen from appendix B the results obtained in the experimental tests give a force which is almost 60% of the force obtained with this calculation. However, the aim of this first CFD model was not the one to have a force similar to the experimental case, but to find a way to impose a motion to the grid.

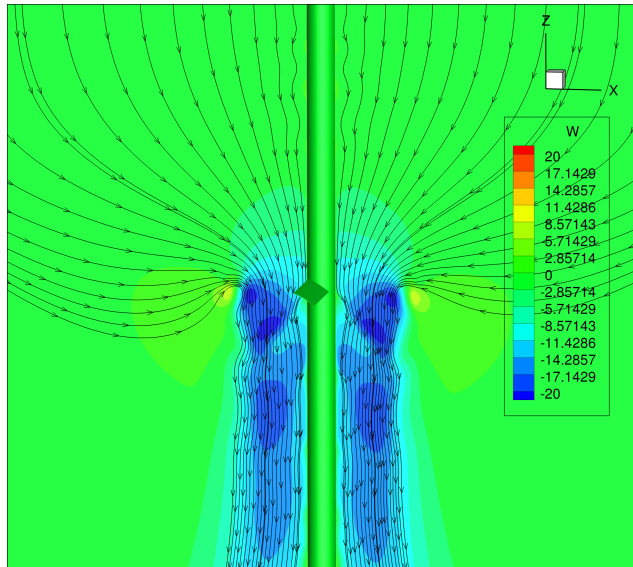


Figure 2.4: Visualization of the velocity field along the z-axis.

By taking a look to the velocity field<sup>6</sup> (figure 2.4) of the domain it can be seen the motion has been set up correctly so it is possible now to start the implementation of a more accurate database and grid. In addition, the typical flow tube expected by the actuator disk theory is

<sup>6</sup>The results are visualized with the CFD++ Solution Visualizer tool or with Tecplot.

visible, confirming a realistic fluid dynamic behaviour.

In figure 2.5 and 2.6 is represented the pressure distribution along the blade. As anticipated, the blade is not very effective near the hub, because of the low velocity that face the section and because of the low density fluid. In the upper part of the blade, there is a low pressure region near the three quarters of the span wise direction which decrease going toward the tip of the blade.

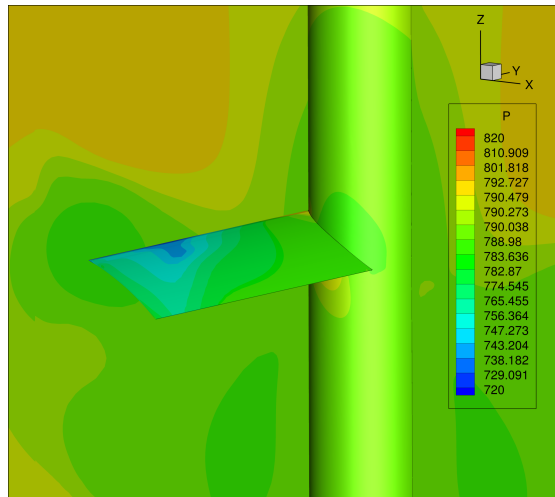


Figure 2.5: Pressure distribution along the upper part of the blade.

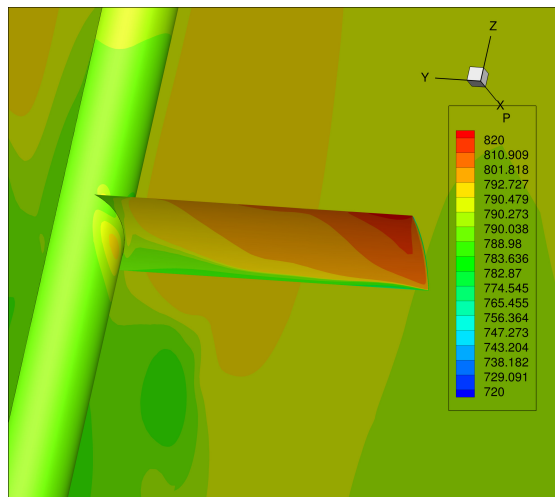


Figure 2.6: Pressure distribution along the lower part of the blade.

Looking at the lower part of the blade it is possible to see that the pressure is slightly higher than the initial value and only near the tip this difference is relevant.

## 2.2 Step 1: CAD improvements

One of the first modifications that can be done is the CAD geometry (or *database*, according to Gridgen's nomenclature). The main difference with the previous case is the cutting of the cylinder which represent the hub: in the new geometry the hub has a  $110\text{ mm}$  long axis and a diameter of  $64\text{ mm}$ . Furthermore, the blade is translated so that one of its sides does not coincides with the axis of rotation and the radius of the cylinder is a bit over dimensioned to avoid some grid generation problems. In fact, the cylinder and the one end of the blade which is near to it must be not only in contact, but the end of the blade must be included in the cylinder so in this way overly distorted cells are not created.

As the database is modified, also the grid must be reconstructed. Choosing a full structured mesh is very time-consuming but allows not only to have a faster convergence, it is possible to have a better control on the grid parameters near the walls (and near leading and trailing edge of the blade), where large changes in flow properties are expected. In fact, the grid is very fine near these areas in order to capture as best as possible the boundary layer. The tip is to have some cells in the  $y^+ < 1$  coordinate, in this way a wall function is not necessary, as explained in section C.3. Furthermore, it is very important to have a smooth variation of cells dimensions from fine to coarse mesh regions, if this condition is not respected, the simulation will have difficulty to converge.

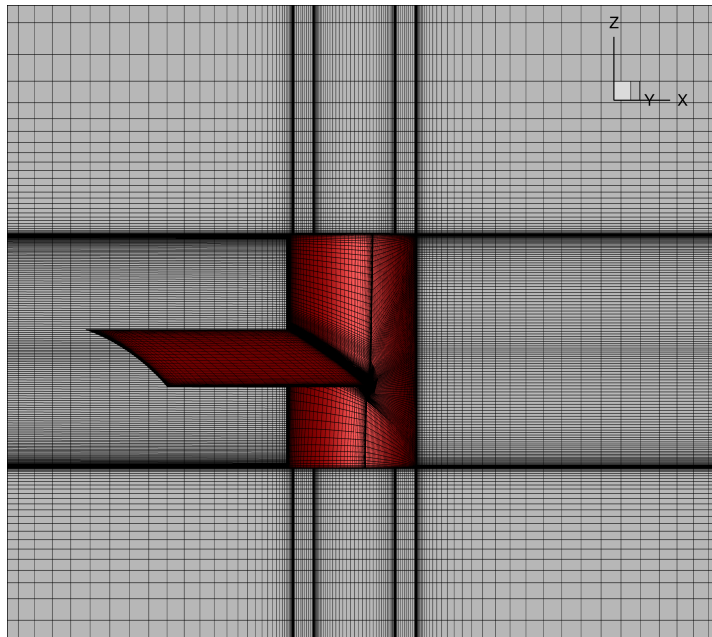


Figure 2.7: Visualization of the new implemented grid with the new database (in red).

Once the grid is finished (figure 2.7), the CFD code can run with the same specifications of the previous case, obviously some convergence problems are encountered but following the tips listed above allows to reach a good solution in terms of residuals and forces.

### 2.2.1 Results

The finished mesh has 2.8 millions of cells and to know how the grid accuracy is related to the cells number it is a good idea to increase the cells number and evaluate how much different are the forces developed by the blade. For this reason, other grid are implemented, maintaining the same geometry but increasing the number of grid points (and of cells as a consequence); the calculation are done with these other grids, which have 3.5, 5, 7.5 and 10 millions of cells, and the result are listed in the table below (table 2.3)

Cells # [mln]	Z-force (Thrust) [N]	X-force [N]	Z-moment (Torque) [Nm]
2.8	0.2508	0.137	0.0227
3.5	0.249	0.1362	0.0227
5	0.2413	0.132	0.0218
7.5	0.2425	0.1333	0.022
10	0.2412	0.1328	0.0219

Table 2.3: Results obtained from the grid convergence test.

It is clear that the mesh with 10 millions cells is the more accurate, anyway the grid with 5 millions cells is also quite similar in terms of forces and moment and in addition the calculation is faster than the previous one. For these reasons, the five millions cells mesh is the better in terms of convergence velocity and accuracy. As already said, the forces and the moment are higher than the case analysed in section 2.1.1, because the blade has a slightly larger diameter and of course a higher tip velocity that leads to a higher thrust developed.

Increasing the number of cells makes necessary doing more iterations to reach roughly the same convergence order, but a more accurate solution is provided. It must be said also that increasing the cells' number makes the simulation to resolve one step longer, for this reason the 10 million cells grid is not the best option, because even if it is more precise, each time step is resolved in more time and, compared for example to the 7.5 million cells grid, it takes roughly 500 iteration more to converge. In all cases the residuals reached at least the order of  $10^{-3}$  and remained stable once the convergence is reached.

With Tecplot it is possible also to visualize the stream traces, that is how the fluid behaves on the calculation domain. In figure 2.8 is represented an important phenomenology which has been already explained in section 1.1.3, the Leading Edge Vortex. With the pressure plotted it can be seen that where there is the point of maximum depression on the blade, there is where the LEV detaches from the blade after being attached to it from the hub. This is in perfect agreement with the definition given in [32]: "[...] Steady span-wise flow from the wing hinge to approximately three-quarters of the distance to the wing tip, at which point the leading edge vortex detaches from the wing surface. This spanwise flow is entrained by the leading edge vortex, causing it to spiral towards the tip of the wing [...]"

From this figure can also be made a comparison between the pressure distribution with the previous case (figure 2.5). In the tip section, it is less evident the depression zone, where the leading edge is already detached.

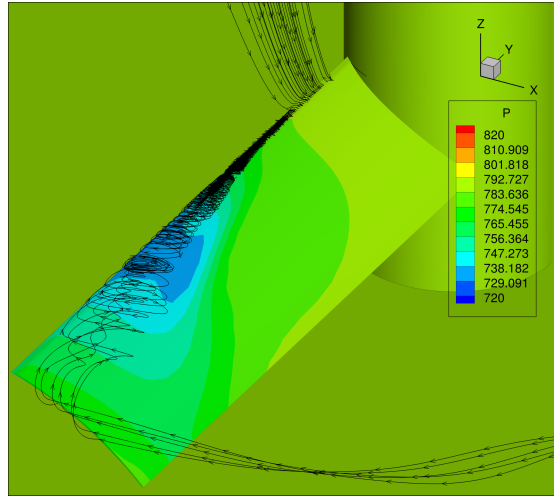


Figure 2.8: Visualization of the Leading Edge Vortex.

## 2.3 Step 2: Vacuum chamber atmosphere

The next step that can be done to improve the accuracy of the model (relative to the experimental case) is to modify the gas properties and the initial conditions. Following this strategy, the grid remains the same as the previous case, but the gas considered is air and not  $CO_2$  and the initial conditions are:

- Static pressure:  $p = 1340 \text{ N/m}^2 = 13.4 \text{ mbar}$ ;
- Static temperature:  $T = 296.65 \text{ K}$

These conditions are the same of the ones in which the experimental tests were done. In particular, the pressure value needs to be computed every time because the temperature changes (as the chamber has not a temperature control system) and the value of density varies with temperature (see Appendix B for further informations). According to this condition, the pressure value is the one which allows to have the right air density (the closest to the Martian value as possible). The simulation is done with the 3.5 millions grid in order to have less computational cost.

A convergence problem is encountered with these small modifications. To resolve it, it is necessary a grid modification: the grid zone below the blade is extended to make sure the wake of the flow is captured in an appropriate manner.

Starting from 3.5 millions cells the grid reaches 4.2 millions of cells (figure 2.9).

### 2.3.1 Results

The forces developed by the blade decreased simply by modifying the fluid type and the initial conditions, as it is possible to see from table 2.4 In the last row the experimental results have been added in order to verify that the new values are going in the right direction, i.e while in the  $CO_2$  atmosphere the z-force was  $\sim 84\%$  more than the experimental one, in this case

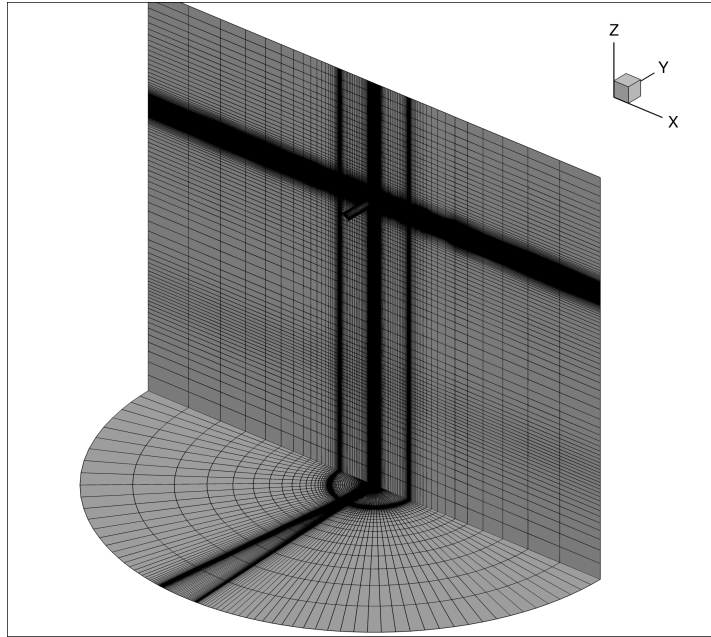


Figure 2.9: Visualization of the new grid with extended domain under the blade.

	Z-force [N]	X-force [N]	Z-moment [Nm]
CO <sub>2</sub>	0.249	0.1362	0.0227
Air	0.1998	0.1128	0.0188
Experimental Results	0.135	/	0.015

Table 2.4: Comparison between CO<sub>2</sub> and air atmosphere results.

the z-force reduced this gap to the  $\sim 48\%$ . This consideration confirms that more model improvements are necessary but also that the modifications that have been done have a positive impact on the model itself.

In figure 2.10 is depicted the velocity z-component,  $w$ , and also in this case it is visible the flow tube: the flow is accelerated downward by the blade. In figure 2.11 are represented more in detail three different sections:

- Hub section: in this section the velocity that faces the blade is very low, considering a radius of  $0.04\text{ m}$  and knowing the rotational speed ( $3000\text{ rpm}$ ) it is possible to find the section's velocity. Before doing this the rotational velocity must be converted from  $\text{rpm}$  to  $\text{rad/s}$

$$\frac{3000\text{ rpm} \cdot \pi}{30} = 314.159\text{ rad/s}$$

then it is possible to calculate the velocity

$$V = \omega r = 314.159 \cdot 0.04 = 12.566\text{ m/s}$$

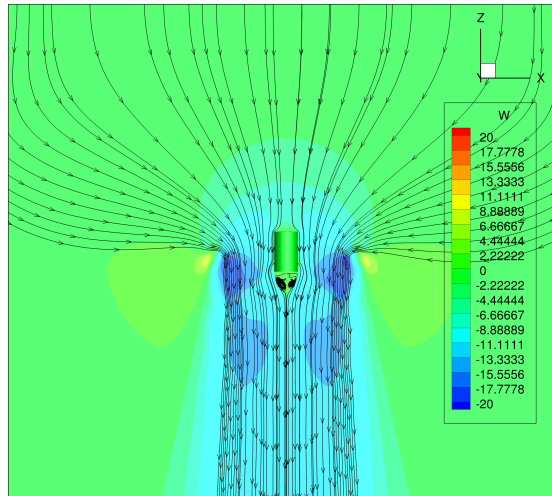


Figure 2.10: Visualization of the velocity z-component field.

Known the velocity it is possible to find the Reynolds number, which represent the balance between the inertial and the viscous forces

$$Re = \frac{\rho cV}{\mu} = \frac{0.0167 \cdot 0.05 \cdot 12.566}{1.04 \cdot 10^{-5}} = 1009$$

where density and dynamic viscosity values can be found in table 1.1.

Following this calculus, it turns out that the Reynolds number is really low and this explain why the flow is completely attached to this section. The flow is viscous and it follows the curvature of the airfoil. Consequently, the force developed by this section is really low.

- Mean section: repeating the reasoning done in the previous point it is possible to find the section's velocity and the Reynolds number.

This time the radius considered is 0.14 m so the resulting velocity is

$$V = 314.159 \cdot 0.14 = 43.98 \text{ m/s}$$

and the Reynolds number

$$Re = \frac{\rho cV}{\mu} = \frac{0.0167 \cdot 0.05 \cdot 43.98}{1.04 \cdot 10^{-5}} = 3531$$

Higher the inertial forces, lower viscous ones. In fact in this section at the leading edge there is the formation of a vortex (the LEV) but the flow separation seems not to involve all the airfoil, so there is a reattachment point.

- Tip section: this section has a radius of 0.23 m and a velocity of

$$V = 314.159 \cdot 0.23 = 72.256 \text{ m/s}$$

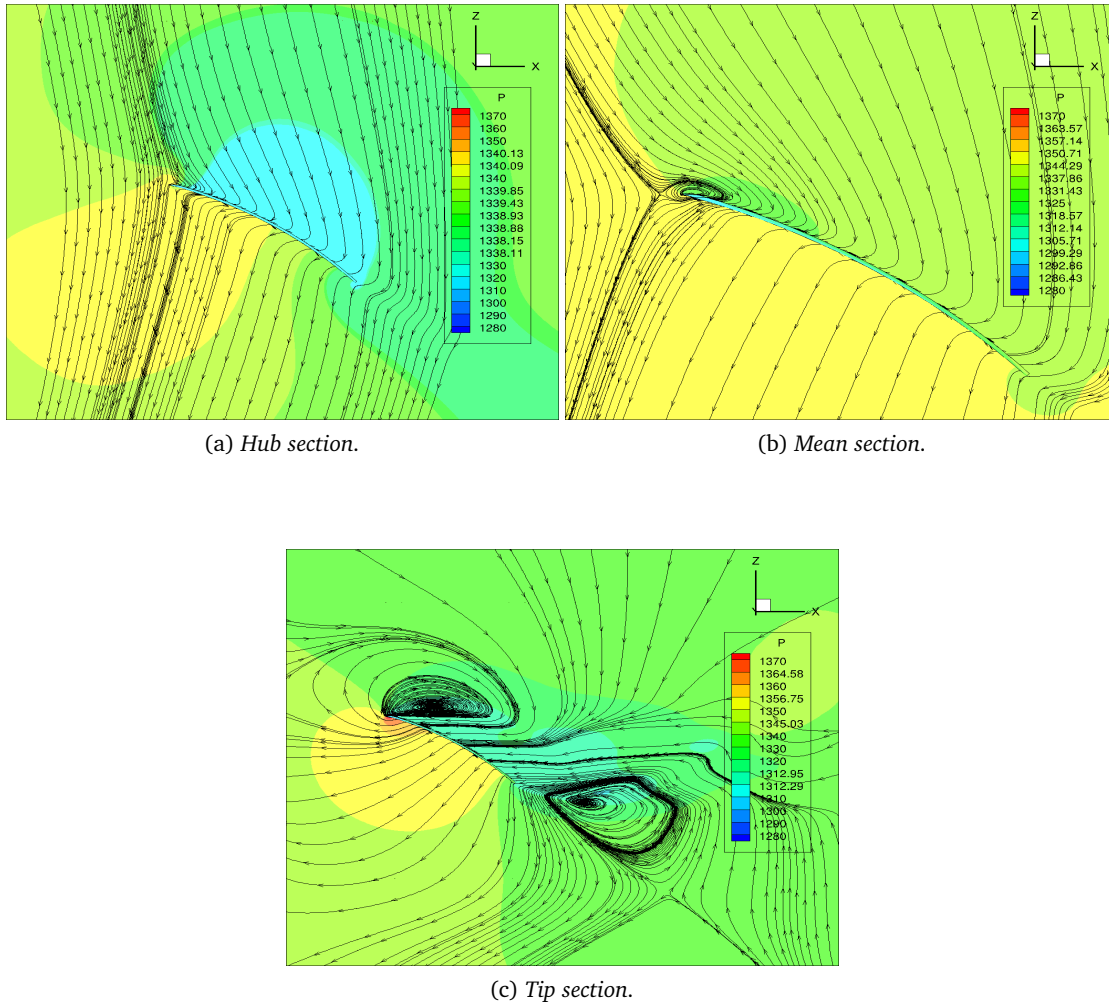


Figure 2.11: Visualization of the flow stream traces for different sections in the blade span wise direction.

and the Reynolds number is

$$Re = \frac{\rho c V}{\mu} = \frac{0.0167 \cdot 0.05 \cdot 72.256}{1.04 \cdot 10^{-5}} = 5801$$

For this Re value as showed in figure 2.11(a) there is a massive separation on the airfoil on the leading edge that involves most of the section. It is visible also another vortex which is detached from the airfoil: as said in section 1.1.3, if the airfoil translates at high angles of attack, the leading edge grows inducing the creation of a trailing edge vortex. In this condition the airfoil is stalled.

What will be done in the next chapter is to modify the grid to make it more accurate to the experimental setup, in particular, the model will be extended to the full rotor (with two blades), the blade's rotational axis will be translated and new elements will be added to the model.

## Chapter 3

# CFD analysis of rotor in vacuum chamber-like grid

The forces and the moment developed by the blade encountered a significant variation simply by changing the gas in which the rotor is operating. Following the structure of the previous chapter, the model is gradually implemented until it is almost the same of the experimental case. The main goal is to extend the model to the full rotor (with two blades) and to introduce some setup components that can affect the aerodynamic behaviour.

### 3.1 Step 1: Modification of the domain dimensions

The next modification that can be done to improve the model is to adapt the grid dimensions to the vacuum chamber ones: so far the rotor has been considered in free flight conditions, the reduction of the dimensions of the grid could introduce significant effect due to the inferior distance between the wall of the chamber and the blade. Furthermore, boundary conditions must be modified because inflow, outflow and farfield are no more a *open* type boundary condition.

#### 3.1.1 Geometry and grid

Starting from the existent mesh, it is not necessary to erase all the domains and restart the grid construction. The part concerning the hub and the blade remain the same while the two semicircle representing the farfield boundary must be modified, decreasing the radius. The vacuum chamber dimensions and specifications can be found in Appendix B, anyway the two dimensions that are needed are the chamber length and radius (respectively 1.2 m and 0.8 m). The two caps at both ends of the chamber are approximated with a flat circle, to simplify the mesh generation process.

In figure 3.1 is displayed the new mesh, it is an evolution of the grid studied in section 2.3. The reduction of the dimension makes necessary the reduction of the cells numbers (in particular near the hub, where the mesh is finer) due to negative volume cells formation; for this reason the cells number has been reduced to 3.8 millions.

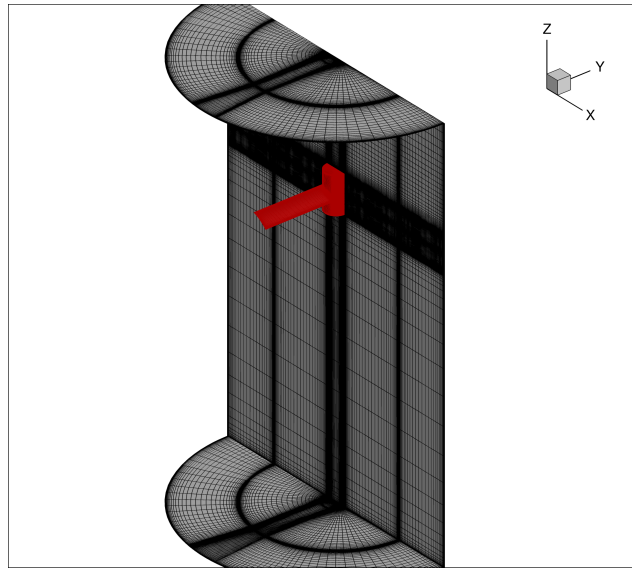


Figure 3.1: Visualization of the vacuum chamber-like grid.

### 3.1.2 Calculation setup

What is immediately evident is that the *farfield* zone is significantly closer to the blade, this for sure will induce some effects on the flowfield. Moreover, *inflow* and *outflow* zones together with *farfield* zone are not a *open* type boundary condition anymore, they must be switched to *wall* type.

While *blade* and *hub* wall condition impose a stationary motion with the mesh (stationary with the relative reference frame), outflow, inflow and farfield need to be stationary in the absolute reference frame; as a consequence their rotation is set 0.0 *rpm* about z-axis.

Bc	Bc type	Sub-group	Condition
Outflow	Wall	Viscous	Rotation, without rotational velocity
Inflow	Wall	Viscous	Rotation, without rotational velocity
Farfield	Wall	Viscous	Rotation, without rotational velocity
Hub	Wall	Viscous	Stationary with mesh motion
Blade	Wall	Viscous	Stationary with mesh motion
Periodic_1	Zonal	Patched only	Rotational, connected to Periodic_2
Periodic_2	Zonal	Patched only	Rotational, connected to Periodic_1

Table 3.1: Resume of the boundary conditions characteristics.

### 3.1.3 Results

There are many differences with the previous cases, especially considering the interference between the blade and the walls of the vacuum chamber.

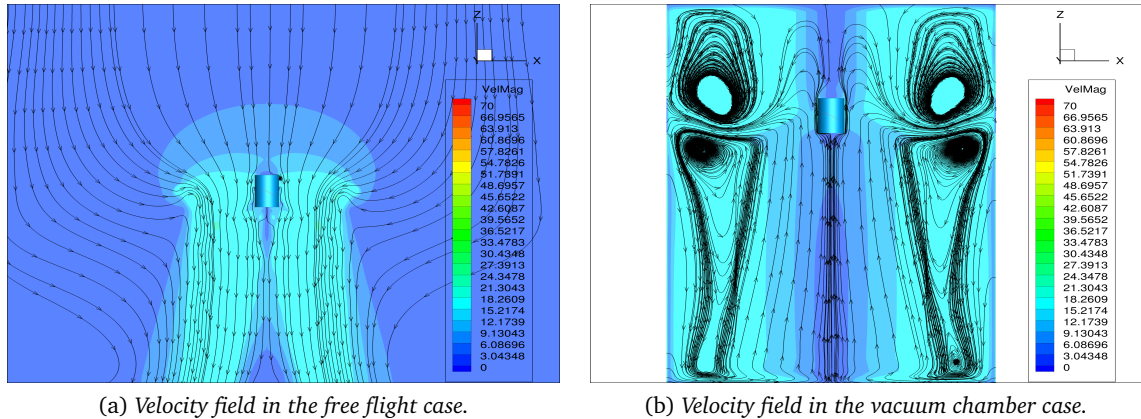


Figure 3.2: Comparison between the free flight and the vacuum chamber flowfield and velocity magnitude distribution.

The calculation converged in a relatively few iterations ( $\sim 600$ ). Despite these differences the results are similar, in fact the blade develops a  $0.2\text{ N}$  thrust and  $0.1105\text{ Nm}$  of torque. This is even more strange if the two flowfields are considered (see figure 3.2): the two cases present very different behaviour.

In fact in free flight condition the velocity field is the one already encountered in figure 2.4 with the flow tube evident under the blade (figure 3.2(a)). Meanwhile in figure 3.2(b) the smaller dimensions of the chamber cause some important recirculation effects near the blade tip. Another very strange fact is the flow direction under the blade: while in the first case the flow is going downwards (because the the blade works as a fan, it pulls the flow in the downward direction), in the second case the flow is going upwards, influenced by the recirculation vortices generated by the walls.

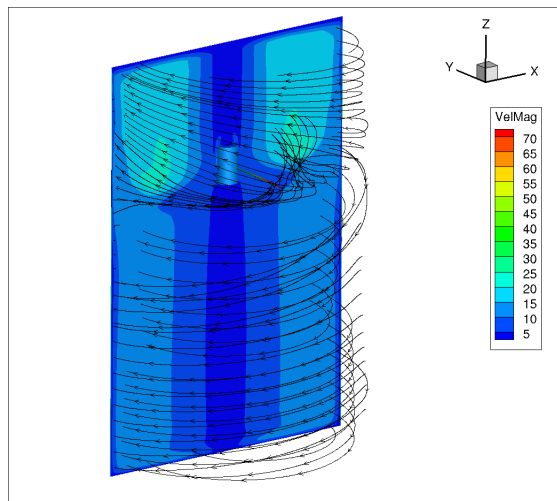
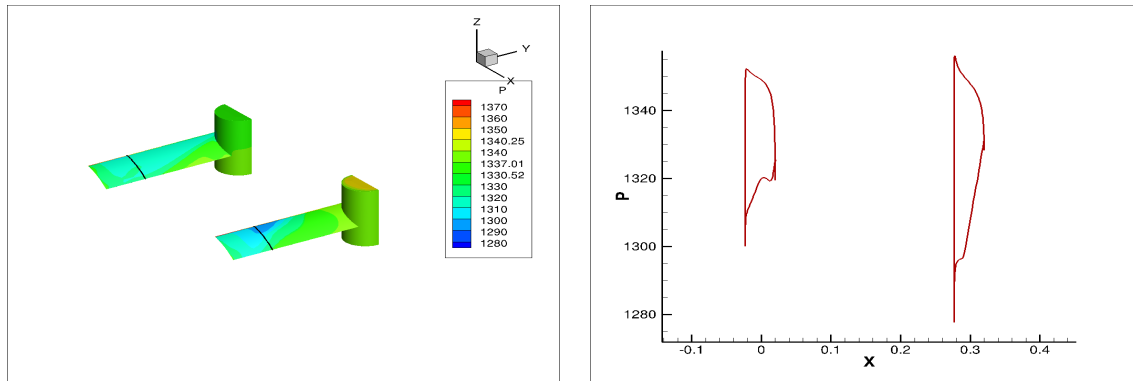


Figure 3.3: Visualization of the three dimensional flowfield.

It is possible to look closer to this flow behaviour through figure 3.3, here it is easy to see the global motion of the air: mainly rotational, the fluid rotates with the blade. This because of the very low density and because of the low Reynolds number.

During the experimental tests, some wool threads are positioned on the wall of the vacuum chamber and with the rotor operating they confirmed the rotational behaviour of the flow.



(a) Pressure distribution in three dimensions, the two black lines indicate the sections in which the 2D pressure distribution are evaluated. (Free flight condition on the right side, vacuum chamber on the left).

(b) 2D pressure distribution.

Figure 3.4: Pressure distributions comparison.

Given these important differences, the reason why the two blades develop the same thrust can be found in the pressure distribution along the blade. The two blades have different pressure distributions but, while in the free flight condition the pressure has a smaller peak value (figure 3.4), in the vacuum chamber condition the pressure has a wider zone in which is less than the initial pressure value, furthermore the areas of the pressure distribution are similar. The thrust generated is a balance between these two characteristics.

As done in the previous section, it is useful to see how the presence of the vacuum chamber affects the flowfield along the blade.

In figure 3.5 there are the same airfoil sections considered in 2.3.1, so even the velocity and the Reynolds number values can be found in that section. Comparing this figure with the previous case, many differences can be spotted:

- Hub section: in this case nearly the entire airfoil is included in a separated flow which forms a bubble, the airfoil is completely stalled. In the previous case instead the flow was going downward and was poorly influenced by the presence of the blade. This behaviour was already anticipated by figure 3.2 and figure 3.3 where it can be seen the flow has a strongly rotating component.
- Mean section: here the flow has a behaviour more similar to the free stream case, the difference is that in this case the leading edge vortex is bigger.

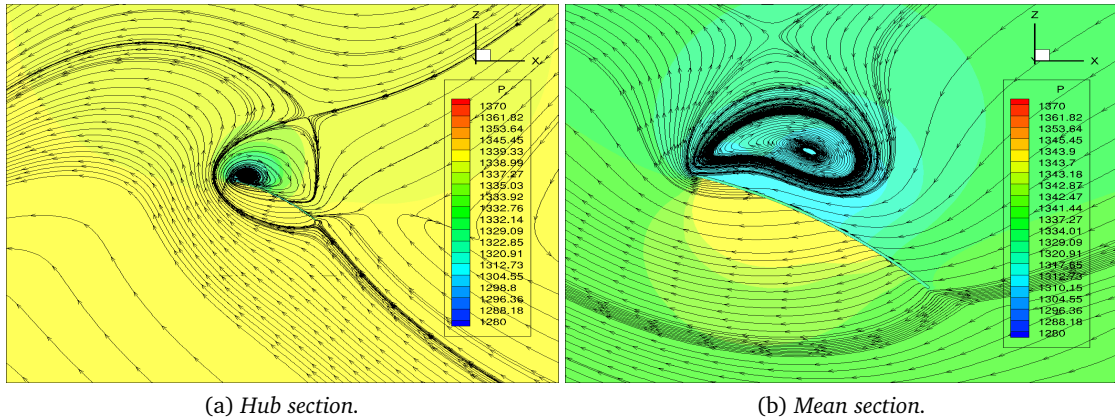


Figure 3.5: Visualization of the flow stream traces for different sections in the blade span wise direction.

- Tip section: the flow does not seem to be influenced by the presence of the blade, probably because it is faster than the other section and it has a rotational component just as the blade.

The flow behaviour in this case is very different from the free flight condition (figure 3.6). This is due to the interaction between the swirling component, caused by the blade motion, and the blade rotation. In the free flight case instead, the flow had a more intense flow in the downward direction so the interaction between the swirling wake and the rotational motion of the blade was not possible (figure 2.8).

### 3.1.4 First turbulence model benchmark

In parallel with the grid modifications, a few runs of the simulation are done changing the turbulence model, in order to see how this affects the velocity convergence and the results in

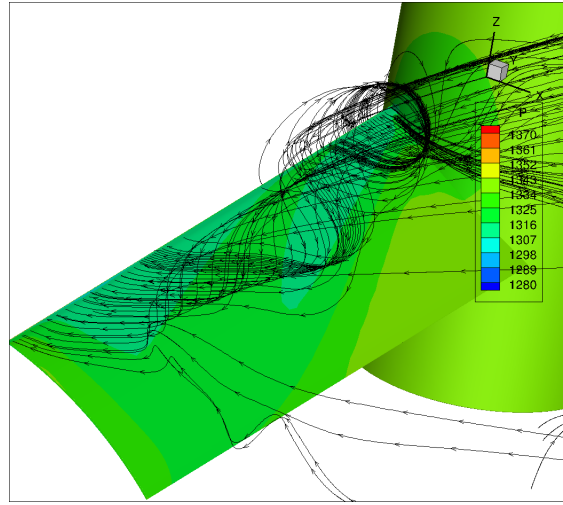


Figure 3.6: Flowfield near the blade: the interaction with the swirling wake component is evident in particular near the hub.

terms of forces. In addition to the realizable  $k-\varepsilon$  model, also *Spalart-Allmaras* and  $k-\omega$  SST models are considered. The results obtained are listed below in table 3.2.

Turbulence model	Z-force [N]	X-force [N]	Z-moment (Torque) [Nm]
Spalart-Allmaras	0.222	0.1208	0.02
$k-\varepsilon$	0.2	0.1105	0.0165
$k-\omega$ SST	0.234	0.1285	0.0185

Table 3.2: Turbulence model comparison.

In figure 3.7 the reader can find the visualization of the stream traces and of the z-component velocity for the different turbulence models analysed.

As can be read in section C.2 the *Spalart-Allmaras* model is simpler than the other models as it has only one equation, in fact the massive vortices present in the vacuum chamber are poorly described. The  $k-\varepsilon$  and the SST model instead show important recirculating zones suggesting the difficulty to capture all the phenomena occurring during the simulation. For this reason *it is logical to predict some discrepancies of the CFD model from the experimental case*. However, in any case four main vortices can be identified.

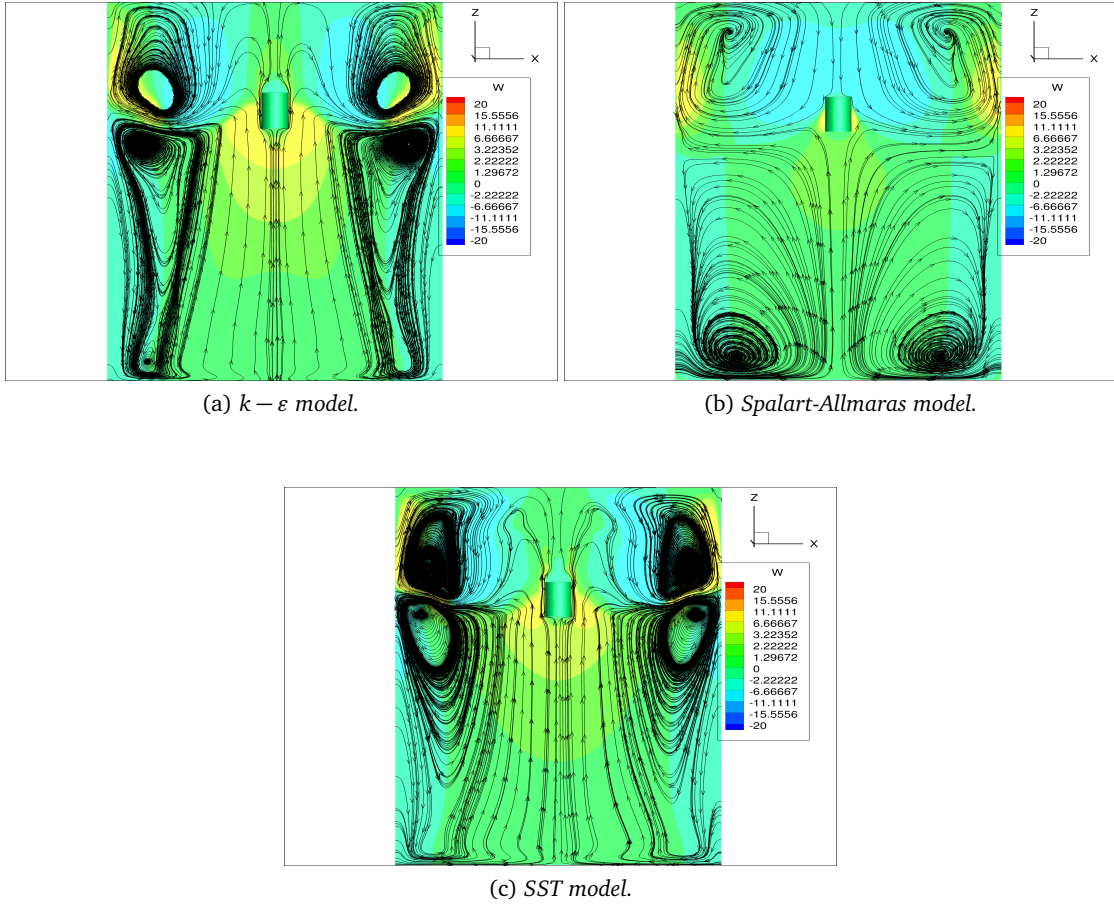


Figure 3.7: Visualization of the flow stream traces for different turbulence models.

### 3.2 Step 2: Introduction of unstructured blocks

So far, the motion has been given to all the grid groups but actually only the blade and the hub move. Furthermore, as the plan is to introduce more elements in the grid, it is more convenient to have a non structured block under the blade to insert, for example, the flat plate on which the rotor is positioned.

For these two reasons, the structured block under the plate is modified into a unstructured one (figure 3.8). To improve convergence performance affected by the introduction of unstructured block, some layers of structured block are maintained, near the *farfield* wall. This is useful also to capture in the right way the boundary layer.<sup>1</sup> As reported in Appendix A this new grid, with structured and unstructured block is called *hybrid mesh*.

No significant variations in the results are expected, actually for the model to be perfect the

<sup>1</sup>Remember that the grid spacing near wall must be on the order of  $y^+ \sim 1$  or it is necessary the use of wall functions.

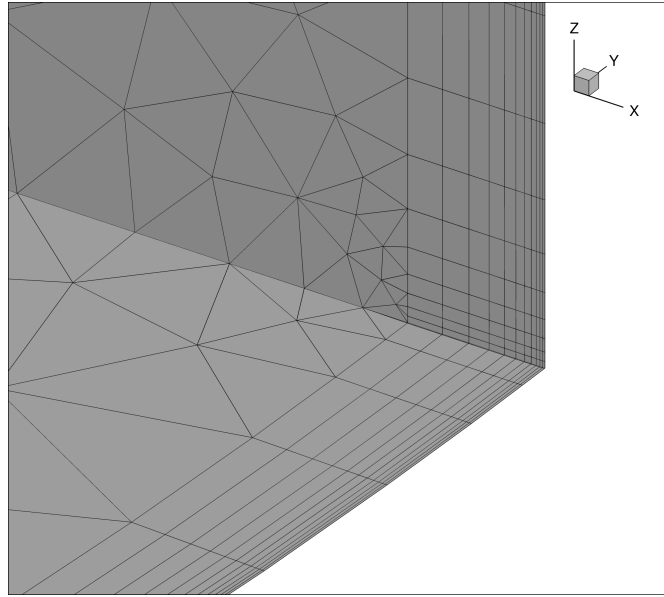


Figure 3.8: Visualization of the structured layers near the vacuum chamber wall.

results should be exactly the same as the ones of the previous section. Obviously introducing the non structured grid generates some variations in the forces developed by the blade, fortunately these variations are not significant (table 3.3) so it is possible to continue the work of improving the model accuracy.

	z-force [N]	x-force [N]	z-moment [Nm]
Structured	0.2	0.1105	0.0165
Hybrid	0.205	0.115	0.0175

Table 3.3: Results comparison between full structured and hybrid grid.

In this case another modification was done: the grid motion in CFD++ is imparted to all groups, but actually only the groups near to the blade and the hub moves. Here the grid motion is given only to the upper part of model, with "upper" it is indicated the part of the mesh above the non structured block. To better understand how the unstructured mesh affects the convergence performances, in the following figures are showed the residuals trend during the simulation for the following cases:

1. The unstructured block under the blade does not have any structured layer;
2. The unstructured block under the blade has some prism layer, so the grid is the one represented in figure 3.8.

The two cases are displayed in figure 3.9. In the first case, the calculation did not converge and the results show high residuals values near the unstructured boundaries. The second case shows better performance with the z-momentum and mass equations residuals gaining one order of magnitude, from  $10^{-2}$  to  $10^{-3}$ .

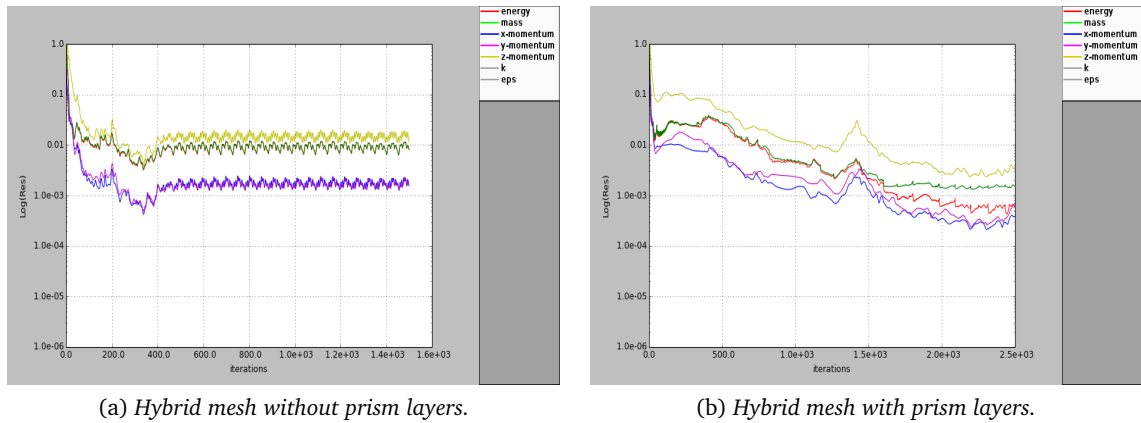


Figure 3.9: Visualization of the residuals for two different simulations.

### 3.3 Step 3: Extension to full rotor

The grid extension to the full rotor configuration is necessary as the blade rotational axis is not the same of the cylinder axis which approximates the vacuum chamber. In the real configuration, the blade, with the steel plate and the two support cylinders, is an element which makes asymmetric the configuration, so the full rotor implementation is required.

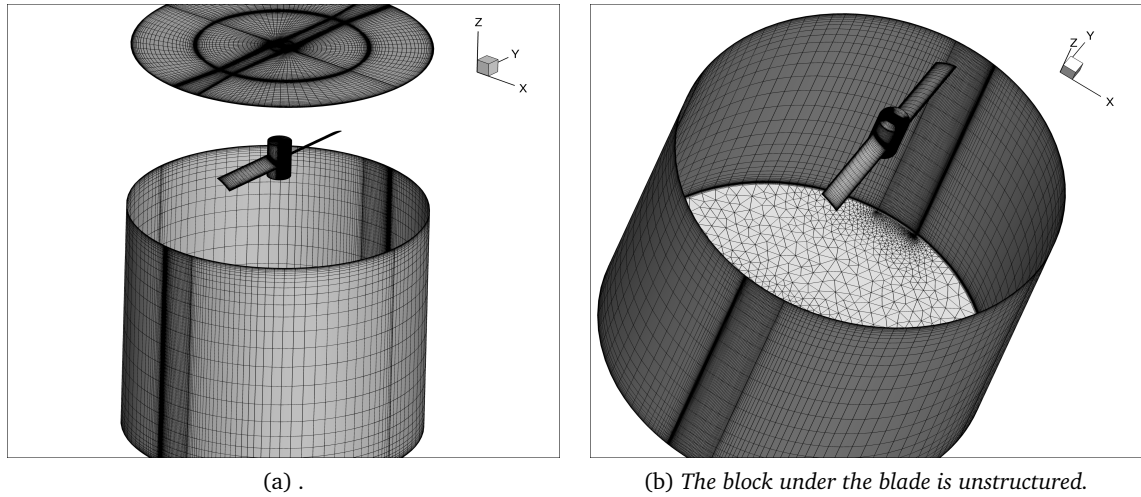


Figure 3.10: Full rotor grid.

With Gridgen it is quite easy to do that, it is sufficient to copy the existent grid and rotate it about z-axis by  $180^\circ$  (figure 3.10). The main goal of this section is only to verify that this method of copying the grid is effective. As the grid is extended, the two *zonal* periodic boundary conditions are not anymore necessary because the calculations are performed for the entire domain. What is expected from this modification is the thrust doubled as the torque

and that the x-force becomes zero. The reason of this last expected result is because each blade develops the same x-force but with opposite directions, this causes the x-force to be zero. A thrust of  $0.4022\text{ N}$  and a torque of  $0.0335\text{ Nm}$  are obtained, these results confirm that the grid has been extended in the right way so it is possible to continue with the model optimization.

### 3.3.1 Results

In figure 3.11 it is possible to find the pressure distribution on the complete rotor. The results confirm the rotor has been copied in the right way as the pressure distribution is symmetric as expected. If the single blade is considered, then it is evident that it has the same pressure distribution than the one encountered in figure 3.4(b).

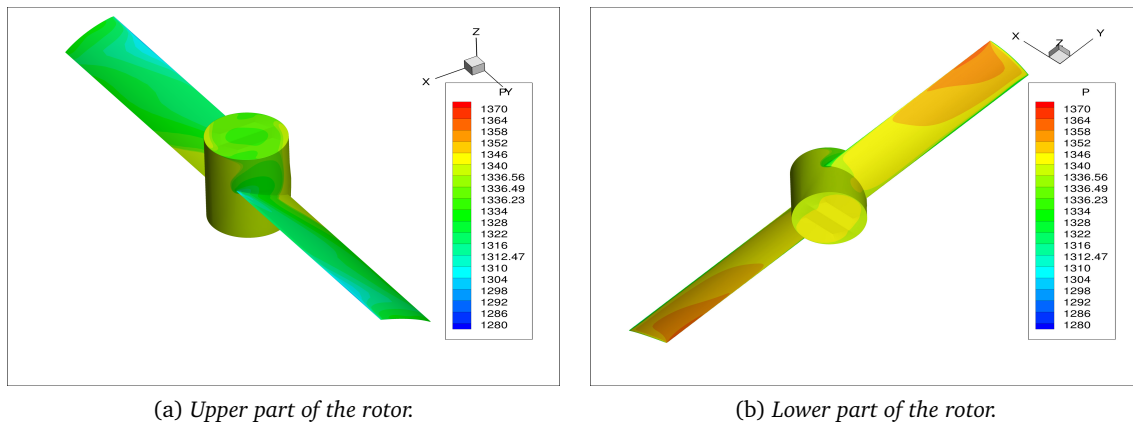


Figure 3.11: Visualization of the pressure distribution on the complete rotor.

## 3.4 Step 4: Introduction of asymmetric elements

The last step of the model implementation is the introduction of the elements that makes the model not anymore symmetric, these elements are the two cylinders that support the structure and the steel plate on which these cylinders are positioned. Last but not least, the blade axis of rotation does not coincide with the vacuum chamber axis. This is important because it make one end of the blade closer to the walls so it must be considered, the model implementation will start from this last point.

What can be done is translating the hub axis along the y-axis by  $0.08\text{ m}$ . The grid obtained will result heavily deformed so a few more modifications must be done. As the centre of rotation imposed in CFD++ has coordinates  $x = 0$  and  $y = 0$ , the whole mesh is again translated and, to reduce the zone that have a motion, a new volume is created inside the mesh. The process is a bit tricky but allows to obtain good results:

1. The blade rotation centre is moved by  $0.08\text{ m}$  along y-axis;

2. A new cylinder is created starting from the existing one by splitting the blocks. This new cylinder is in an intermediate position between the external one (vacuum chamber walls) and the internal one, that is the cylinder originated from the revolution of the blade;
3. As only the grid contained inside the intermediate cylinder has a motion, it is detached from the rest. This leads to the formation of new interfaces and boundary condition as a consequence;
4. Now the grids are two; in CFD++ through the use of the *Concatenate* tool the two meshes are again put in one piece.

The reader now could ask himself the motivation of the process at point 3, the reason is purely for ease of calculation set up. In the *grid motion* window in CFD++, the user is asked to specify the groups that have a motion. Due to grid construction, groups can be a lot and the grid motion specification can both be time consuming and can lead to errors. With this strategy, there are only two groups, one that moves and the other stationary.

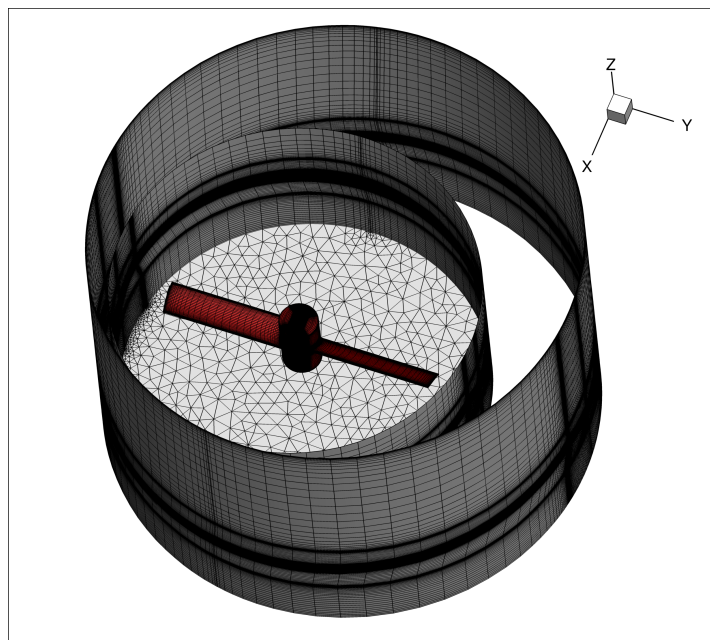


Figure 3.12: Visualization of the two grid blocks concatenated, the inner cylinder is the one with motion. Here the lower part of the grid is not displayed.

With the  $k - \varepsilon$  turbulence model, the calculation converged in about 800 iterations and gave  $0.36 N$  as thrust and  $0.031 Nm$  as torque. These results confirmed the modification of the flowfield done by simply translating the blade axis of rotation. In particular, the new results get the simulation a little closer to the experimental ones, now the thrust calculated is 33% more than the one obtained in the vacuum chamber. It is right to remind that also the experimental results are affected by some errors, especially talking about the vibrations of the

vacuum chamber that affect the measures of thrust and torque.

In figure 3.13 is showed the pressure field in the vacuum chamber. In this case the pressure distribution is not any more symmetric and the wall closer to the blade causes an interference effect on the blade.

This can produce an imbalance of thrust produced between the blade which is near the wall and the other. The effect, given the rotation is periodic and can lead to vibrations, probably the same vibrations which noticed in the experimental test. Some of them are produced by the wires which support the entire rotor: at around 2700 *rpm* it is easy to see the wires clearly oscillating. Obviously the effect of this vibrations in detrimental for the measure of thrust and cause a lot of noise both in terms of measures and in term of audible noise.

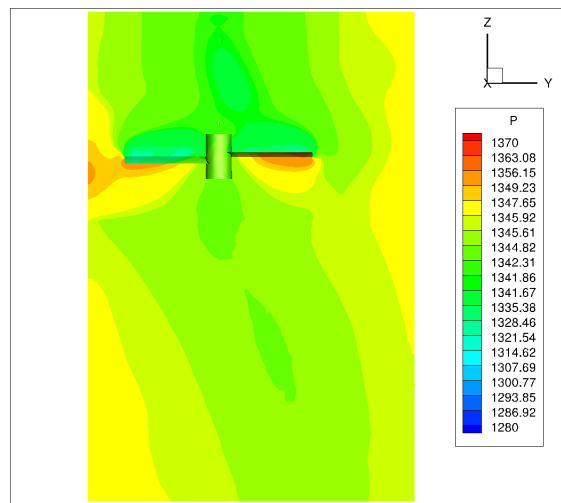


Figure 3.13: *Pressure field in the vacuum chamber.*

As a second (and last) modification, steel plate and the two cylinders can be added. These last elements will complete the model so it is expected that they modify the flowfield in a manner that allows to obtain results even closer to the experimental ones than the results just obtained<sup>2</sup>.

Thanks to the non structured blocks introduced in section 3.2 it is easy to introduce these elements. The two cylinders have the following dimensions:

- Diameter= 0.048 *m*;
- Height= 0.46 *m*;
- Distance between the two cylinder= 0.015 *m*.

They are placed symmetrically to the hub above the steel plate which has dimensions the closer to the real ones (figure 3.14). As it has been done for the vacuum chamber walls, some layers of finer grid are maintained in order to capture in the right way the boundary layer.

<sup>2</sup>The previous division of the mesh in rotating and non-rotating grid is maintained.

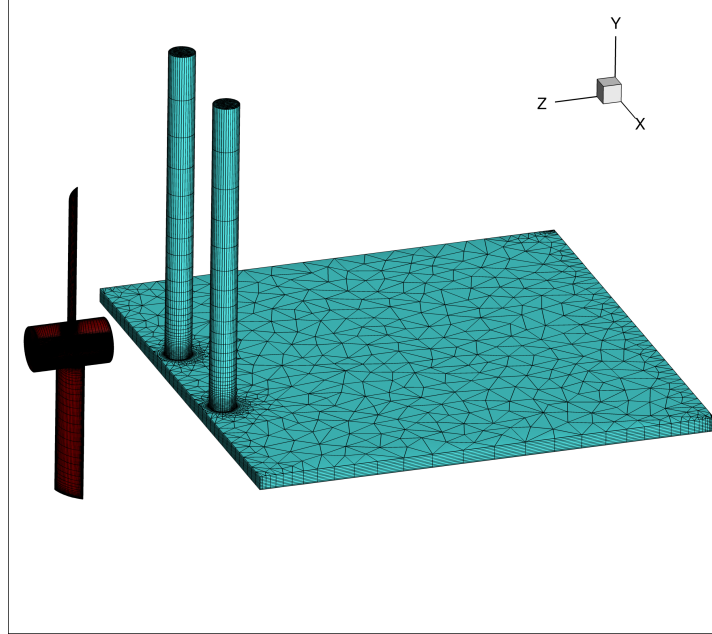


Figure 3.14: Visualization of the new mesh elements (in blue).

The results obtained show an unpredicted effect, in fact the thrust is  $0.388\text{ N}$  and the torque  $0.0325\text{ Nm}$ . Actually it was expected a decrease of the force due to the presence of the two cylinders, while the thrust increases.

### 3.4.1 Turbulence model benchmark

As there are significant turbulence effects in this configuration, it is useful to perform the simulation with different turbulence model to see how the turbulence affects the calculation. Many turbulence model have been tested, but the only ones that gave good convergence, beside the  $k - \varepsilon$  model were the Spalart-Allmaras and the Langtry-Menter SST 4-equation transitional model.

The latter model is also known as the  $\gamma - Re_\theta$  SST model because it uses the equation for  $\gamma$  and  $Re_\theta$  (respectively intermittency and momentum-thickness Reynolds number) in addition to the equation of  $k$  and  $\omega$  used in the classical SST model. The two new equation are [33]:

$$\frac{\partial (\rho\gamma)}{\partial t} + \frac{\partial (\rho v_j \gamma)}{\partial x_j} = P_\gamma - E_\gamma + \frac{\partial}{\partial x_j} \left[ \left( \mu + \frac{\mu_t}{\sigma_f} \right) \frac{\partial \gamma}{\partial x_j} \right] \quad (3.1)$$

$$\frac{\partial (\rho Re_\theta)}{\partial t} + \frac{\partial (\rho v_j Re_\theta)}{\partial x_j} = P_\theta + \frac{\partial}{\partial x_j} \left[ 6\sigma_\theta (\mu + \mu_t) \frac{\partial Re_\theta}{\partial x_j} \right] \quad (3.2)$$

where  $P_\gamma$  and  $E_\gamma$  are source terms for the  $\gamma$  equation while  $P_\theta$  is the source term of the  $Re_\theta$  equation. The  $Re_\theta$  is defined as follows

$$Re_\theta = \frac{\rho V \theta}{\mu}$$

where  $V$  is the local velocity and  $\theta$  is where the transition occurs.

Despite the Spalart-Allmaras model is a one equation model, the Langtry-Menter 4-equations model has better convergence performances while the realizable  $k - \varepsilon$  model is worst of the three, but giving anyway good results.

Turbulence model	Thrust [N]	Torque [Nm]
$k - \varepsilon$	0.386	0.0325
Spalart-Allmaras	0.365	0.032
Langtry-Menter SST	0.4	0.0328

Table 3.4: Results obtained with different turbulence models.

From the results listed in table 3.4 it is evident that, whatever is the turbulence model chosen, the thrust developed by the blade differs from the results obtained in the experimental tests. This should not surprise the reader because, as already said, there are significant turbulence effects which probably the model did not catch.

Moreover, even if the experimental tests show a certain accordance with the results coming from Maryland University, there are several effects that affects the measures, vibrations and instruments calibration firsts of all.

By looking at the flow field in the different cases (figure 3.15) it can be seen as there are no significant differences. Once again, the Spalart-Allmaras model seems the less precise as instead the Langtry-Menter SST model looks more precise describing quite well the vortices over the rotor.

It is curious that *the two cylinders seem not to affect the flow*, this justifies the the similarity of the forces developed in respect to the case in section 3.3.

### 3.4.2 Transient simulations

So far, all the simulations performed were steady state ones. Given the high non-stationary motion induced by the vacuum chamber's walls, it is logical to perform some transient simulations.

In steady-state simulations the characteristics of the flow do not change with time, these are reached after a relatively long time. Otherwise, transient simulations require real time information to determine the time intervals at which the solver calculates the flow field. The flow characteristic can be one that a steady-state condition is never reached, even if all other aspect of the flow condition are not changing.

By this definition it is clear that the transient simulation could be helpful in this last section, as the the numerous vortices induced by the walls can lead to unsteady flow conditions.

It is seen that with the current implemented mesh, the calculation does not start. This problem has been really hard to solve but an accurate analysis of the grid pointed out some critical problems of the grid itself:

1. Together with Metacomp's support it is decided to apply a *patched only* option to the zonal boundary conditions instead of *patched and overset*. The grids do not have to be node-aligned at the zonal boundaries but these boundaries should still be roughly coincident.

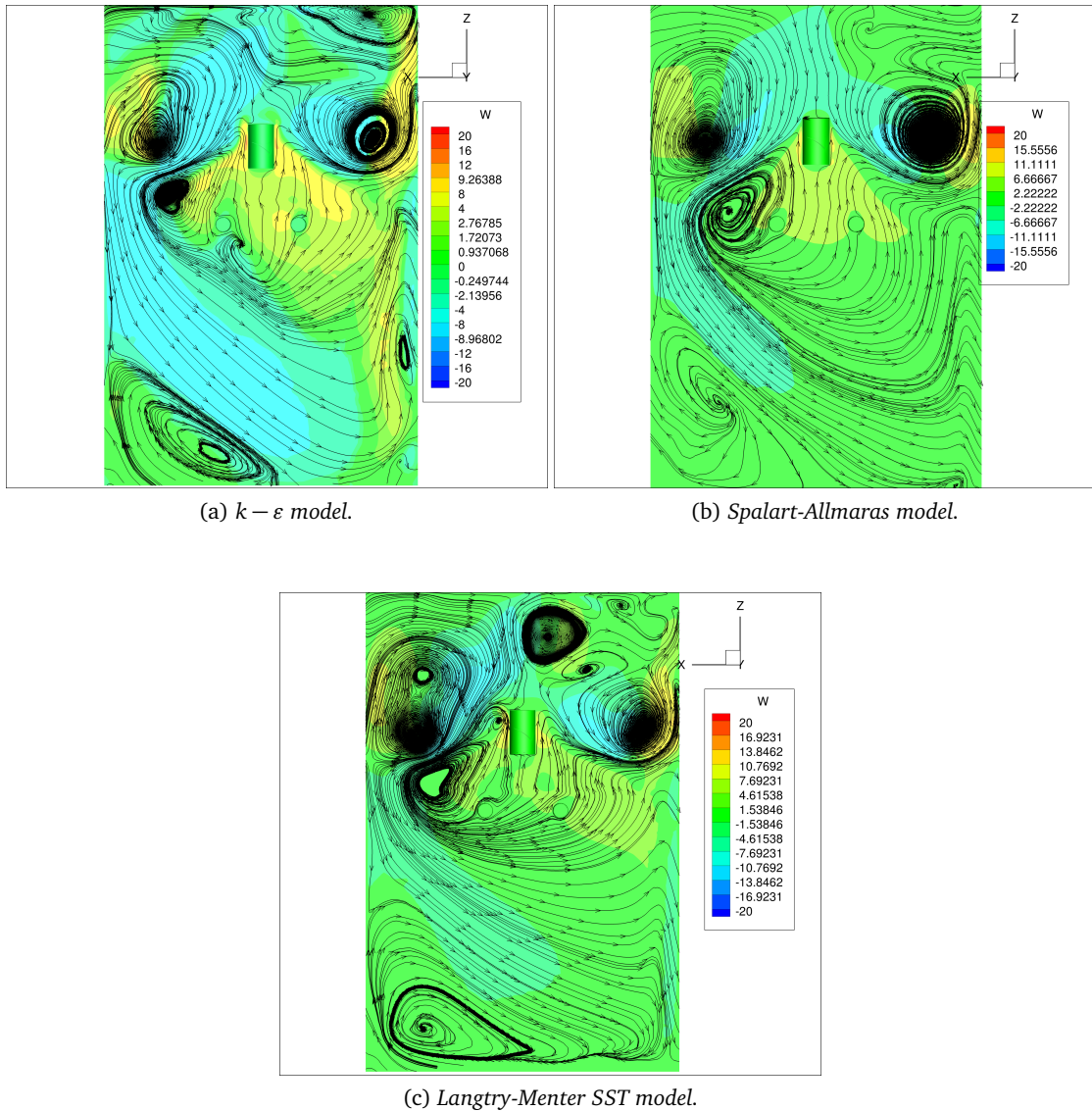


Figure 3.15: Flow visualization for the different turbulence models.

2. By taking a closer look to the lower interface between the rotating and the stationary cylinder, an important discrepancy between the two domains is found. The lower domain is an unstructured one and it has a coarser mesh distribution along its surface while the upper domain is a structured one and it has a really fine grid compared to the other domain.

When the calculation starts the solver tries at every time step to link the unstructured cells with the structured ones at every time step after applying the motion. Now, one unstructured cell, which is larger than the structured one, incorporates more than one

structured cells so the solver has difficulty in connecting the cells in an appropriate manner.

3. Another issue encountered is in the interface at the top of the rotating group. Here some points do not lie in the same plane. Once the mesh starts to rotate there will be gaps in certain locations which will also cause issues with zonal connections. This problem can be easily solved with a tool in CFD++ but given the other issues it is decided to improve the grid directly in Gridgen.

To overcome the second issue it is necessary to change the grid structure, in particular the moving block. The concept of the modification is to have the same interface between the rotating and the stationary grid in terms of cell's type and dimensions, in this way there will not be a problem with the zonal boundary conditions.

To do that, the structured mesh is restricted to an essential part of the grid, just the part which contains the rotor. In this way another block is created, its function is to make a link between the unstructured and fixed domain and the structured and rotating group. As a consequence it is a rotating, unstructured group.

Given these tips, a new mesh is implemented and thanks to the new unstructured volume (instead of the structured one) also the cells' number is reduced. This is an important aspect as transient simulations are really time-demanding and reducing the number of cells allows to have results in a faster way.

### 3.4.3 Results

In a transient simulation there are more parameters to be set. This type of simulation is a time-marching one so it has to be defined a global time step which is the variation of time between one global step and the following. It is said *global* time step because there is another type of step, which is called *inner iteration step*; in fact, for every global time step the user can define how much inner global time steps the simulation can perform.

For example, in this simulation the global time step has been chosen to be 0.0001 s and the inner iteration step are set to 15. This means that when the simulation starts at time 0 the solver will solve the system of equations for fifteen times at the same time step, then it will pass at the following time step, that will be  $t = 0.0001$  s, and run other 15 iterations with this time, and so on.

It is straightforward that a time-dependent simulation takes a lot more time than a steady-state one<sup>3</sup>, but for this type of problem it is better to know the variation of the forces developed during time.

If an explicit scheme is chosen, it is important to choose the global time step so that it respects the CFL condition

$$CFL = \frac{V \Delta T}{\Delta x} < 1$$

where  $V$  is the largest wave propagation speed,  $\Delta T$  is the physical (global) time step and  $\Delta x$  is the cell size.

---

<sup>3</sup>A single global time step takes about 10 minutes to be solved with 8 cores.

If an explicit scheme were chosen, the global time step would be  $10^{-15}$  and given the time time necessary for a single time step this would be very time-consuming. Fortunately, the time integration is implicit<sup>4</sup> so it is possible to overcome this problem and a physical time step of  $10^{-4}$  s is chosen.

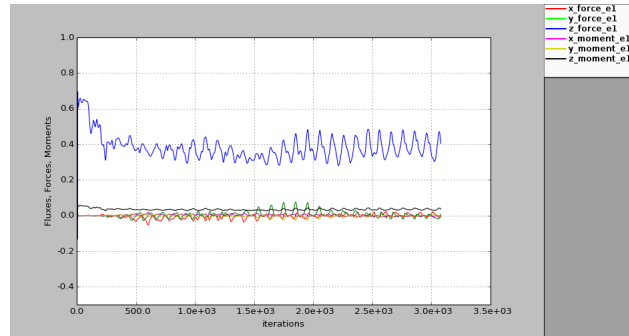


Figure 3.16: Forces developed by the blade.

In figure 3.16 are displayed the forces developed by the blade. Their trend is very different from the one they have in steady state simulations as explained above.

There are consistent oscillations in the thrust that from  $t = 0.2$  s go from  $0.28$  N to  $0.48$  N periodically. A complete oscillation lasts about 100 iterations, in terms of time nearly  $0.01$  s and in terms of frequency about  $100$  Hz.

By looking at the pressure distribution results, it can be seen that when the blade, during its rotation, passes near the cylinders, on the upper side the low-pressure zone become larger and on the lower side the high-pressure zone also become more evident. As the blade passes the two cylinders, so it is in the lower zone of the vacuum chamber, these two effects vanish and the pressure distribution returns similar to the one observed in the other simulations. This alternating effect could be responsible for the thrust oscillations observed in figure 3.16.

To find out if these oscillations are due to the presence of the cylinders it is chosen to make another simulation with the grid without the plate and the two cylinders.

In figure 3.17 it is possible to see that the thrust is characterized by the same oscillations of the previous case. This lead to affirm that this unsteady phenomenon is not due to the interference with the cylinders but probably is related with to the vortex shedding: the thrust drops occur when the vortex detaches from the blade.

<sup>4</sup>Explicit and implicit schemes are approaches used in numerical analysis to obtain numerical approximations to the solutions of time-dependent ordinary and partial differential equations. To know the solution at the new time step, the explicit methods calculate the state of the system using information coming from the system at the current time. Implicit methods, instead, find a solution by solving an equation involving both the current state of the system and the later one.

Furthermore, this last type of method requires extra time in resolving the equations. They are used anyway because many problems can't be resolved with explicit schemes due to numerical instability, to solve them an impractical time step should be chosen to respect the CFL condition.

The use of explicit time stepping is fairly restrictive. It is used primarily to capture the transient behaviour of moving waves such as shocks, because it is more accurate and expensive from a computational point of view than the implicit time stepping methods in such cases [35].

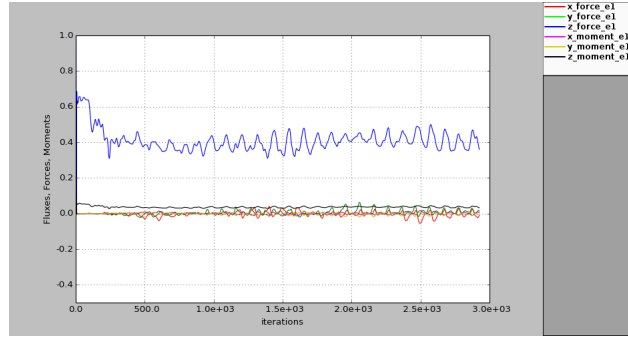


Figure 3.17: Forces developed by the blade in the case without the two cylinders and the blade.

The vortex shedding is a particular flow condition in which vortex separate periodically from the body generating a particular wake called *Karman vortex street*. This condition occurs when there is a *bluff body* such as a cylinder, but in general a body which has a section with similar dimensions (not thin). In this case, given the high pitch of the blade, it can be considered a *bluff body*. Considering a cylinder invested by a flow, when the Reynolds number is very low ( $\sim 10$ ) two recirculating bubbles (one on the upper half of the cylinder and the other on the lower half) start to form in the back of the cylinder. As the Reynolds number starts to rise these two bubbles become bigger until they separate from the body, not simultaneously but alternatively. The frequency of the bubble's detachment is related to the Strouhal number

$$St = \frac{fD}{V}$$

where  $f$  is the frequency,  $D$  is the diameter of the body and  $V$  is the velocity.

Now, it can be said that starting from the blade's hub, as the Reynolds number rises, also the dimension of the vortex rises, leading to the detachment of it near the tip. This phenomenon does not clash with the LEV concept, in fact as observed in figure 2.8 the vortex starts at the blade's hub, grows going in the span-wise direction and then separates as soon as the Reynolds number is high enough. In [38] similar oscillations in the lift coefficient of a NACA 4402 airfoil are found out for a Reynolds number of 6000 confirming that this behaviour is not typical only of this particular case. Furthermore, in that analysis is pointed out that as the angle of attack is increased, the amplitude of the oscillations increases and the frequency of oscillation changes. In figure 3.18 it is possible to see the evolution of the pressure distribution through the blade rotation. The process in which the suction zone appear more evident and then disappear is cyclic, this is the process responsible for the thrust oscillations and in which vortices periodically detach from the blade.

On the lower part of the blade it can be observed an analogous process, while the two cylinders and the plate do not have any pressure variation, confirming what previously said, they do not have any impact on the flow and on the forces developed.

3.4 – Step 4: Introduction of asymmetric elements

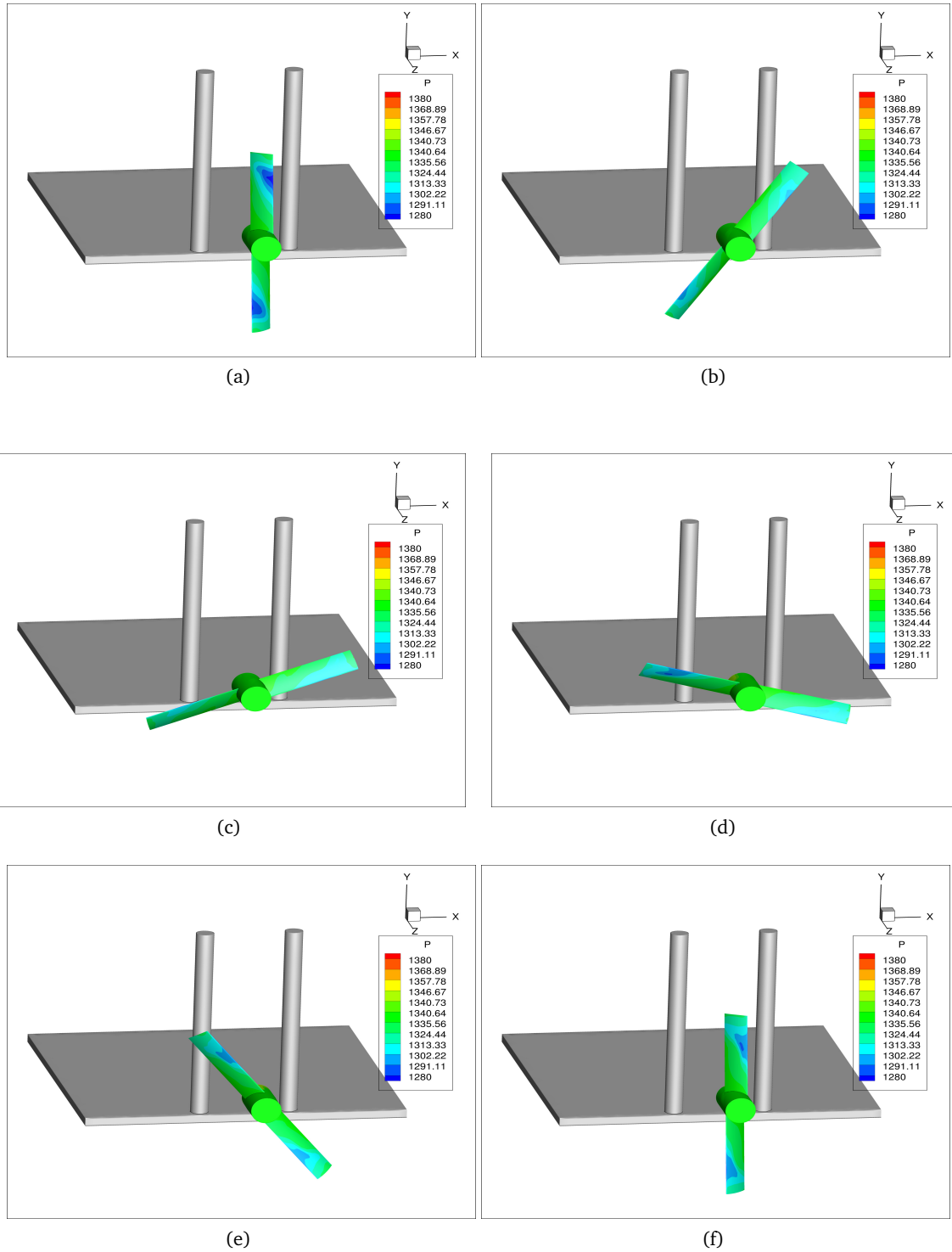


Figure 3.18: Flow evolution on the upper part of the blade.

### Results' summary

In table 3.5 are resumed all the results obtained in this first part of the thesis: the ones

Case	Turbulence model	Thrust [N]	Torque [Nm]
Experimental		0.27	0.03
Free flight in CO <sub>2</sub>	Realizable $k - \varepsilon$	0.4826	0.0436
Free flight in air	Realizable $k - \varepsilon$	0.3996	0.0376
Vacuum chamber	Realizable $k - \varepsilon$	0.4	0.0335
	Spalart-Allmaras	0.444	0.04
	$k - \omega$ SST	0.468	0.037
Vacuum chamber with asymmetries	Realizable $k - \varepsilon$	0.36	0.031
Vacuum chamber with plate and cylinders	Realizable $k - \varepsilon$	0.388	0.0325
	Spalart-Allmaras	0.365	0.032
	L-M SST	0.4	0.0328

Table 3.5: Summary of the results obtained in all the simulations.

which are useful to make a correlation between the experimental tests and the CFD model are highlighted in red. Assuming correct the value registered in the experimental tests (remember that there were a lot of vibrations and noise in the measurements), it is obvious that the correlation is not reached in an acceptable manner. In fact *in the best case the error done with the 3D model reaches the 35% of the value registered in the vacuum chamber, while in the worst case it rises to the 48%*. Meanwhile, a good accuracy in the torque results is obtained. The error done oscillates from the 6% to the 9%.

It must be said that the torque error could rise roughly to the thrust error value because, as reported in Appendix B, the torque measured in the experimental test was affected by some error due to friction on the transmission's shaft. For this reason it is likely that the torque error is similar to the thrust one.

Another aspect that emerges is the increment in thrust and torque given by changing the gas in which the rotor operates: there is an increment of 20% and 15% respectively for thrust and torque in the CO<sub>2</sub> atmosphere.

In blue are highlighted the results useful for the blade design, these values need to be compared with the thrust requested to lift a useful mass.

## **Part II**

# **Aerodynamic optimization**



## Chapter 4

# Blade Optimization

The blade characteristics definition is a key point in the drone design, as from this it is possible to know the dimensions of the blades (and consequently of the drone), how much weight is it possible to lift and also how much power it is necessary to use the drone. As a consequence aerodynamics is a design driver of great importance.

What is clear from the first part of this work is that with the actual configuration of the blade is not able to lift a mass of practical interest, mainly because of the blade dimensions. In fact, given the very low flow density, the blade has a small chord to pull the flow downstream. For this reason in this part will be implemented a method to improve the blade performances. Together with this, the goal is also to find a way to make this optimization process as fast as possible but maintaining a good accuracy of the results.

It worth to remember that the blade optimization can be divided into two parts: the optimization of the blade itself, such as chord distribution and twist angle, and airfoil optimization, which involves an optimization of the airfoil efficiency. In this work only the first of the two part will be considered.

In the first section of this chapter the CFD++ *rotor model* will be analysed and used in order to make a comparison with the 3D model implemented in the previous sections and with the experimental results. In the following sections will be presented a method to obtain blade span-wise chord and twist angle distributions optimized to get the maximum performances available.

### 4.1 Momentum theory

The theory was developed by Rankine and Froude and then improved by Betz who introduced the effect due to the wake's rotation.

In the momentum theory the rotor is modelled as an actuator disk which provides energy to the flow receiving back a force as a reaction. The actuator disk is a circular surface of zero thickness that can support a pressure difference and accelerate the air through the disk [34]. The theory aims to find the influence of the rotor on the flow, this means to find the induced velocity and the power required for a given thrust.

The actuator disk model assumes a rotor blade loading which is equivalent to considering an

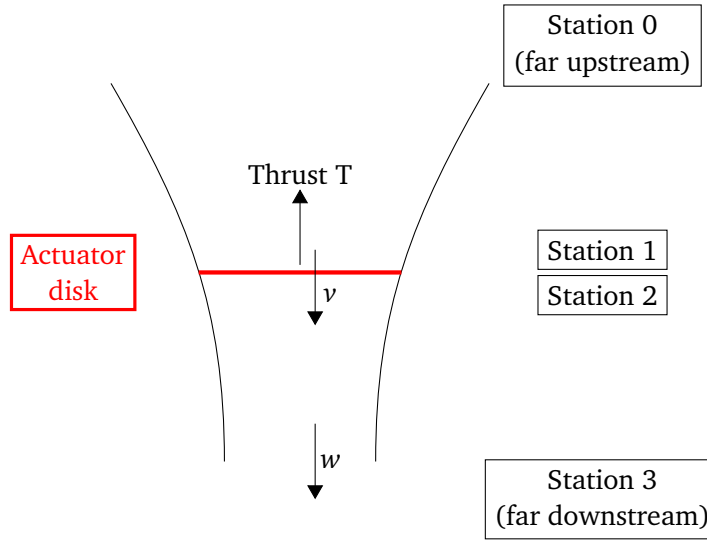


Figure 4.1: Schematic representation of the momentum theory model. (draw adapted from [34])

infinite number of blades, which is a strong approximation and limits the model to be used only as a first estimate of the wake induced flow.

Some assumptions need to be made:

1. The pressure discontinuity across the disk and the induced velocity are constant along the disk radius;
2. The fluid is inviscid and incompressible;
3. The flux is stationary and has zero vorticity everywhere;
4. The rotational energy in the wake due to the rotor torque is neglected.

Let's now consider a disk of area  $A$  and thrust  $T$ ,  $v$  is the induced velocity at the rotor disk and  $w$  is the wake-induced velocity far downstream. The mass flux through the disk is  $\dot{m} = \rho Av$  and is constant all along the wake thanks to the mass conservation.

The momentum conservation equates the momentum at far downstream less the momentum far upstream so, for a hovering rotor it is obtained

$$T = \dot{m}w \quad (4.1)$$

From the energy conservation instead it is obtained

$$Tv = \frac{1}{2}\dot{m}w^2 \quad (4.2)$$

by substituting the 4.1 from the 4.2 the following relation is obtained

$$w = 2v$$

It is possible then to write  $T = \dot{m}w = 2\rho Av^2$  and to find the induced velocity

$$v = \sqrt{\frac{T}{2\rho A}} \quad (4.3)$$

hence the induced power is

$$P = Tv = T\sqrt{\frac{T}{2\rho A}} \quad (4.4)$$

It is useful to introduce another parameter, the *figure of merit*, which is a rotor hovering efficiency indicator and it is defined as the ratio of the minimum power required (ideal power) to hover and of the actual power required to hover. This parameter comes in handy when considering hovering rotor because the general blade efficiency formulation is

$$\eta = \frac{TV_\infty}{P}$$

but in hovering  $V_\infty = 0$  m/s so it would be useless to measure the rotor efficiency with this expression.

Anyway, the *figure of merit* (FM) is defined as

$$FM = \frac{P_{ideal}}{P}$$

from the momentum theory it is known that  $P_{ideal} = Tv = T = \sqrt{T/2\rho A}$ , hence

$$FM = \frac{T\sqrt{T/2\rho A}}{P} = \frac{C_T^{3/2}}{C_p} \quad (4.5)$$

where the last formulation is expressed in terms of coefficients, with  $C_T$  as thrust coefficient and  $C_p = C_T^{3/2}/\sqrt{2}$  as power coefficient.

A more detailed analysis can be provided by the *extended momentum theory* which accounts for the wake rotation and the related losses. The theory is still based on conservation laws but another equation is added, the angular momentum conservation. Given the thrust, *the theory aims to find the axial and tangential velocity distributions which define the minimum induced power.*

It is assumed that there are no viscous losses on the surface of a body in the fluid, the conservation equations are the following:

- Mass conservation<sup>1</sup>:

$$\rho \int \vec{q} \cdot \vec{n} dS = 0 \quad (4.6)$$

$$\int_{A_d} v \cdot dA - \int_{S_1} w \cdot dS_1 = 0 \quad (4.7)$$

<sup>1</sup> $\vec{q}$  represents the velocity vector,  $dS$  the differential area,  $\vec{n}$  the outward normal to the surface.

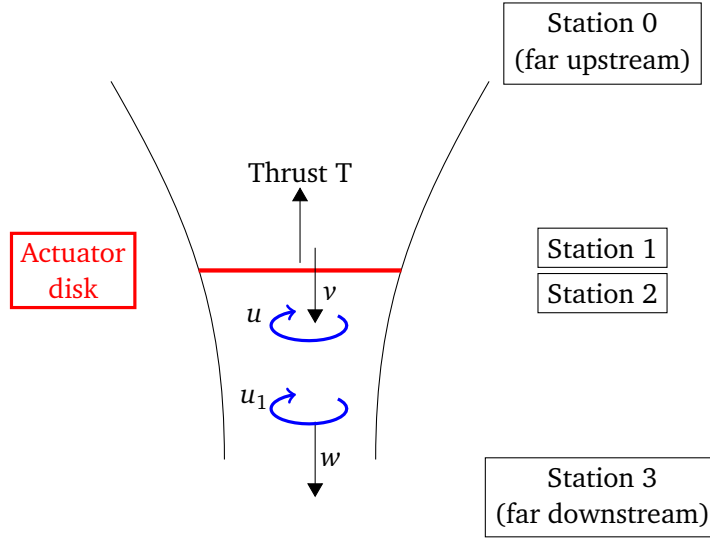


Figure 4.2: Schematic of the extended momentum theory, the swirl component is depicted in blue. (Draw adapted from [34])

- Momentum conservation:

$$\rho \int \vec{q}\vec{q} \cdot \vec{n}dS + \int p\vec{n}dS = \vec{F} \quad (4.8)$$

$$T = \int_{A_d} \Delta p \cdot dA = \int_{S_1} \rho w^2 dS_1 + \int_{S_1} (p_1 - p_0) dS_1 \quad (4.9)$$

- Energy conservation:

$$\int (p + 1/2\rho q^2) \vec{q} \cdot \vec{n}dS = dE/dt \quad (4.10)$$

$$P_i = \int_{A_d} \Delta p \cdot v dA + \int_{A_d} \frac{1}{2} \rho u^2 v dA \quad (4.11)$$

- Angular momentum conservation:

$$\rho \int \vec{r} \times \vec{q}\vec{q} \cdot \vec{n}dS + \int p\vec{r} \times \vec{n}dS = \vec{M} \quad (4.12)$$

$$Q = \int_{A_d} \rho v u r \cdot dA = \int_{S_1} \rho w u_1 r_1 dS_1 \quad (4.13)$$

where  $v$  is the axial velocity component,  $u$  the tangential component and  $Q$  is the blade torque. In the equation 4.11 the power is composed of two component: the first is the work done in moving the air through the disk, the second is the kinetic energy added to the slipstream.

For the energy conservation, it is known that the induced power is the same given by the formula  $P = Q \cdot \Omega$ , now equating this last formulation (in which equation 4.13 can be substituted) with the equation 4.11, the following expression is obtained:

$$\int_{A_d} \Delta p \cdot v dA + \int_{A_d} \frac{1}{2} \rho u^2 v dA = \int_{A_d} \Omega \cdot \rho u v r \cdot dA \quad (4.14)$$

which gives

$$\Delta p = \rho \left( \Omega r - \frac{1}{2} u \right) u \quad (4.15)$$

From Momentum Theory, it can be written that  $\Delta p = 2\rho v^2$ , which in equation 4.15 gives

$$2v^2 = \left( \Omega r - \frac{1}{2} u \right) u \quad (4.16)$$

The *extended momentum theory* for a rotor with swirl in the wake can be formulated as follow: the power must be minimized for a given thrust, with the constraint given by equation 4.16. This is a variations problem and can be solved through the Euler equation. The expression which, combined with 4.16, gives the approximate relations for  $u(r)$  and  $v(r)$  is

$$u(r) = \Omega r \cdot \frac{2v_0^2}{(\Omega r)^2 + v_0^2} \quad (4.17)$$

$$v(r) = v_0 \cdot \frac{(\Omega r)^2}{(\Omega r)^2 + v_0^2} \quad (4.18)$$

where  $v_0$  is a constant.

It is possible then to find the relation for the thrust, from  $T = \int 2\rho v^2 \cdot dA$ :

$$T = 2\rho A v_0^2 \left[ 1 + \frac{4v_0^2}{(\Omega r)^2} \cdot \ln \left( \frac{v_0}{\Omega R} \right) + \frac{v_0^2}{(\Omega R)^2} \right] \quad (4.19)$$

Known the thrust it is possible now to find the induced power, remember that from equation 4.11 it is composed of two terms:

$$P = \int_{A_d} \Delta p \cdot v dA = \int v(r) \cdot dT$$

as  $\Delta p \cdot dA = dT$

$$P_{swirl} = \int_{A_d} \frac{1}{2} \rho u^2 v dA = \int_0^R \rho \pi r u^2 v dr$$

## 4.2 Blade Element Theory

Momentum theory and blade element theory were two separate approaches in the early development of rotary wing theories and were put together in the 1920's, in the *Blade Element Momentum Theory*.

Blade element theory calculates the forces on the blade due to its motion through the air [34]. It is based on the Prandtl lifting-line theory<sup>2</sup> applied to rotating wing. According to this theory, the blade is divided into infinitesimal sections, each of these is considered a two-dimensional airfoil and produces aerodynamic forces.

<sup>2</sup>Mathematical model that predicts lift distribution over a three-dimensional unswept wing.

The effects of the wake is contained in the *induced angle* at the section. To know this angle it is necessary to have an estimation of the wake-induced velocity at the rotor disk, this can be provided by the *momentum theory*. Moreover, it is assumed a *low disk loading* ( $T/A$ ), a *uniform inflow* and *stall and compressibility are neglected*.

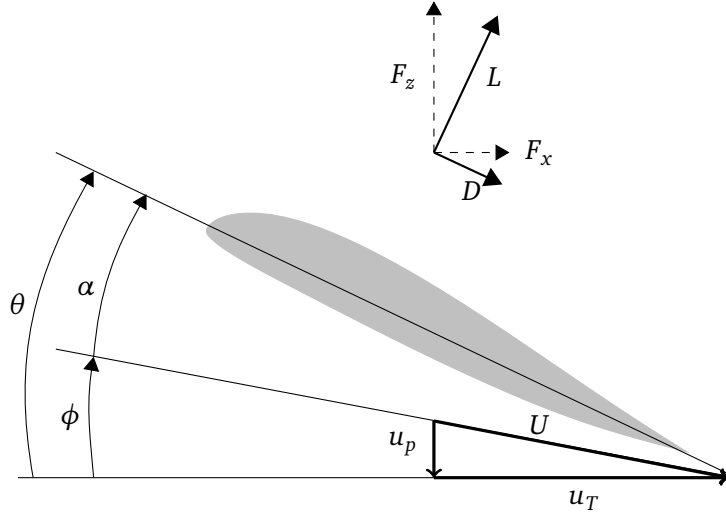


Figure 4.3: Schematic of the blade section. (Draw adapted from [34])

Let's consider now the blade section in figure 4.3.

The pitch angle  $\theta$  is measured from the plane of rotation to the zero-lift line. The air which invests the section has two components:  $u_t$  is tangent to the disk plane and  $u_p$  is perpendicular to the latter. In hover condition  $u_p$  consists in the induced velocity obtained with the actuator disk theory, while  $u_t$  is the rotational velocity  $\Omega r$ . So the resultant velocity is

$$U = \sqrt{u_t^2 + u_p^2} = \sqrt{(\Omega r)^2 + v_i^2}$$

and can also be defined the velocity angle as

$$\phi = \tan^{-1} \left( \frac{u_p}{u_t} \right)$$

As a consequence, the aerodynamic angle of attack is

$$\alpha = \theta - \phi$$

Thanks to the trigonometry it can be written

$$F_z = L \cos \phi - D \sin \phi \quad (4.20)$$

$$F_x = L \sin \phi + D \cos \phi \quad (4.21)$$

then elemental thrust, torque and power can be written as

$$dT = NF_z dr \quad (4.22)$$

$$dQ = NF_x dr \quad (4.23)$$

$$dP = \Omega dQ = NF_x \Omega dr \quad (4.24)$$

where  $N$  is the number of blades and  $dr$  is the infinitesimal radius considered. By neglecting the compressibility and stall effects, the lift coefficient is linearly related to the angle of attack, then the blade section forces are

$$dL(r) = \frac{1}{2} \rho U^2(r) C_l(r) dS = \frac{1}{2} \rho U^2(r) C_l(r) c(r) dr$$

and

$$dD(r) = \frac{1}{2} \rho U^2(r) C_d(r) dS = \frac{1}{2} \rho U^2(r) C_d(r) c(r) dr$$

where infinitesimal lift and drag are function of the radius because along the blade span the airfoil can be different for different sections and also velocity and chord can vary.

It is possible to make another assumption, if the inflow angle  $\phi$  is small (which is almost true for low inflow rotors) then it follows:

- $\cos \phi \approx 1$ ;
- $\sin \phi \approx \phi$ ;
- $\phi \approx \frac{v_i}{(\Omega r)}$ ;
- $U \approx \Omega r$ ;

given these approximations it can be written

$$dT \cong NLdr = N \frac{1}{2} \rho (\Omega r)^2 C_l c dr \quad (4.25)$$

$$dQ = N(L\phi + D)rdr = N \left[ \frac{1}{2} \rho \Omega^2 r^3 (C_l \phi + C_d) c dr \right] \quad (4.26)$$

$$dP = \Omega dQ = N \left[ \frac{1}{2} \rho (\Omega r)^3 (C_l \phi + C_d) c dr \right] \quad (4.27)$$

Hence is possible to obtain thrust, torque and power simply by integrating the infinitesimal quantities

$$T = \frac{N\Omega^2 \rho}{2} \int_0^R C_l c r^2 dr \quad (4.28)$$

$$Q = \frac{N\Omega^2 \rho}{2} \int_0^R (C_l \phi + C_d) c r^3 dr \quad (4.29)$$

$$P = \frac{N\Omega^3 \rho}{2} \int_0^R (C_l \phi + C_d) c r^3 dr \quad (4.30)$$

### Tip losses

One of the Prandtl lifting-line theory limits is that it does not consider the tip losses due to the finite extension of the blade and other three-dimensional effects such as tip vortex and vortex wake. As a consequence the theory loses its meaning near the blade tip, in fact, according to it the lift does not go to zero at the blade tip. This fact is important as it can lead to an overestimation of the forces developed. The tip losses can also be seen as a reduction of the actuator disk area which implies a higher induced power loss (figure 4.4).

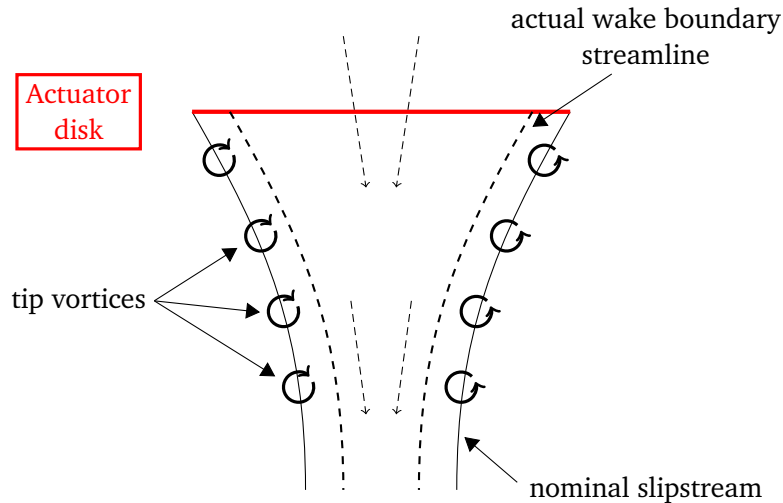


Figure 4.4: *Effect of tip loss.* (Draw adapted from [34])

It is defined a *tip loss factor* as

$$B = 1 - \frac{\sqrt{2C_T}}{N}$$

where  $N$  is the blade number and  $C_T$  is the thrust coefficient.

### 4.3 Rotor model

This model is available with CFD++ license and is based on the *Blade Element Momentum Theory* (BEMT) exposed in the previous section. It can be used both as a source term and as a boundary condition: the rotor model modifies the momentum and pressure of the fluid as it pass through the rotor. These changes in momentum and pressure are determined by the blade properties and rotor operating conditions [31].

To run the model, it is necessary to have some informations about the rotor geometry:

1. Number of blades;
2. Outer radius of rotor blades;
3. Hub radius of rotor blades;

4. Rotation speed of rotor blades;
5. Freestream velocity (zero in case of hovering condition);
6. Pitch angle;
7. Twist angle;
8. Fluid density;
9. Blade Chord;
10. Blade centre of rotation;
11. Positive thrust direction: the direction in which thrust is produced;
12. Azimuth datum direction: direction on the rotor plane where the azimuth angle is set to zero.

It is necessary then to specify a file name where informations about the blade section performances are listed.

If there are no section variation along the blade it is sufficient to write on this file the angle of attack (in the range in which the blade is expected to be operating) and the relative lift and drag coefficient<sup>3</sup>.

On the contrary, if there are section variations, in the file for each section it is necessary to specify the adimensional coordinate ( $r/R$ ), the pitch angle and the name of the file in which are contained the information relative to the blade performances. So in this last case if there are 10 different sections, it is needed a file with the various pitch angles and other ten files where lift and drag coefficient are listed.

Now, the next step is to perform the rotor model for the blade studied in the first thesis chapters to see how much is different from the experimental tests and from the CFD model. To do that, it is necessary to simulate the same conditions both for the rotor model and for the 2D simulations necessary to calculate the lift and drag coefficient (section 4.3.1).

#### 4.3.1 2D CFD simulations

To simulate the 2D airfoil, a C-type mesh is constructed with Gridgen. The grid has about 56000 cells and is structured.

Now, the comparison with the 3D model has to be made in the freeflight case so the initial condition of the simulation will be:  $p = 790 \text{ N/m}^2$  and  $T = 210.5 \text{ K}$ .

It is necessary also to specify the velocity that faces the airfoil and on this point it is possible to proceed in different ways. For example it can be considered the velocity associated to the mean Reynolds value along the blade span. In this case three different sections are considered: each of them has a Reynolds number which can be found respectively near the hub, in the middle

---

<sup>3</sup>These two coefficient can be obtained with the software *Xfoil* for example, but to have a better accuracy, as the Reynolds number is really low, it is chosen to perform 2D CFD simulation for the airfoil.

of the blade and at the blade tip. In this way it can be seen also how the Reynolds number affects the airfoil performances.

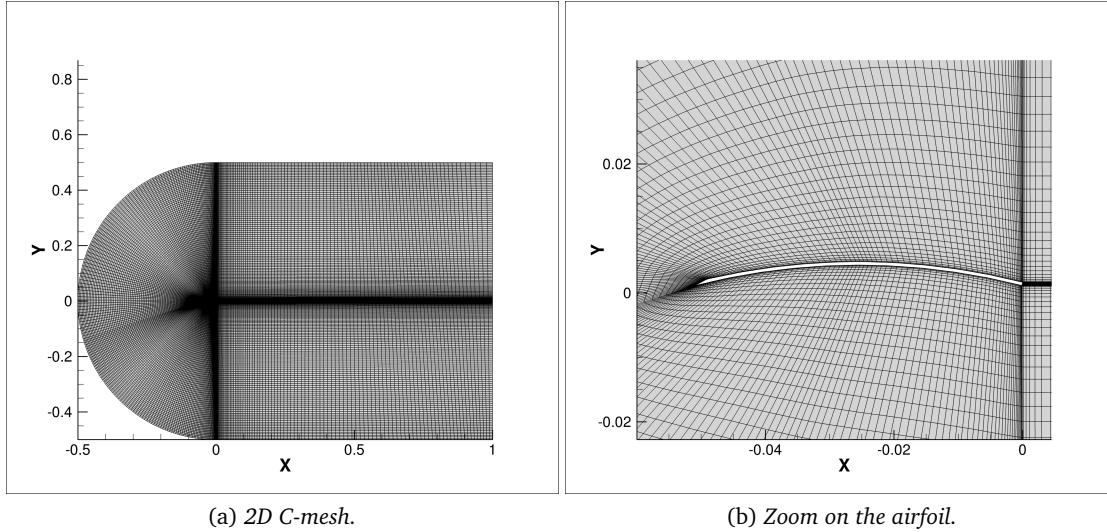


Figure 4.5: Grid constructed for the two-dimensional simulations.

Every simulation is run for different values of angle of attack, from  $0^\circ$  to  $56^\circ$  with a gap of four degrees between each values of  $\alpha$ , in steady state mode with  $k-\varepsilon$  turbulence model. For the three different sections the operating conditions are listed in table 4.1.

	Tip	Mean	Hub
Pressure [ $N/m^2$ ]	790.5	790.5	790.5
Temperature [ $K$ ]	210.5	210.5	210.5
Density [ $Kg/m^3$ ]	0.019879	0.019879	0.019879
Chord [ $m$ ]	0.05	0.05	0.05
Velocity [ $m/s$ ]	72	45	15
Dynamic viscosity [ $Pas$ ]	1.06e-05	1.06e-05	1.06e-05
Re	6.75e+03	4.22e+03	1.41e+03

Table 4.1: Reynolds number and set up parameters for the different sections.

The results obtained show that the mean section has a better efficiency and higher value of lift coefficient than the other two sections. For the section in the  $Re = 4.22e^3$  condition (figure 4.6), at about  $12^\circ \div 16^\circ$  of the angle of attack the simulations have difficulty to converge so the forces values are not really accurate, and the airfoil reaches the stall at very high values of  $\alpha$  and maximum efficiency is reached in the range of  $4^\circ \div 8^\circ$ , while the maximum lift coefficient is reached at  $\alpha = 24^\circ$ .

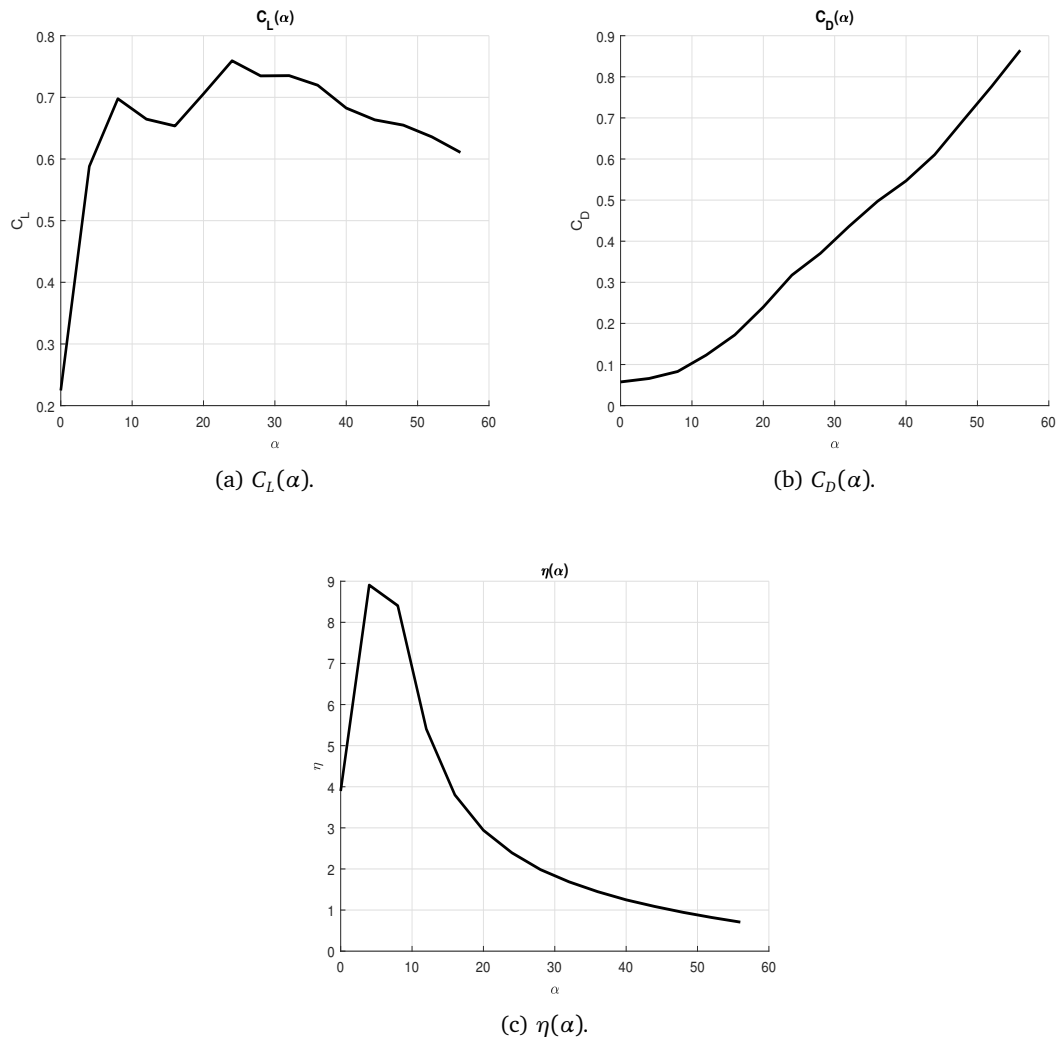


Figure 4.6: Results of the 2D CFD simulations for the mean section ( $Re = 4.22e^3$ ).

### 4.3.2 Simulation setup

Now that the information about the lift and drag coefficient of the blade section are available it is possible to go on with the rotor model simulation.

First of all it is necessary to construct the grid: another point in favour of the rotor model is that the grid can be easily made, because the rotor is modelled as a circle. In fact the grid has a cylindrical shape, easy to build by simply creating a block from a circle. It is only important to pay attention to the grid spacing, in fact in order to have a better accuracy of the results a finer grid is used for the rotor surfaces (it is important to create two surfaces for the rotor, the upper and the lower surface), for this reason it is necessary a smooth transition from the rotor to the farfield zone.

The implemented grid has about 650000 cells (figure 4.7), which is really less than the five

millions cells grid of the 3D model presented in section 2.2. From this aspect it is straightforward the reduction of time needed for the simulation to be converged, remember that the reason why the rotor model is investigated is to find a faster way to know which is the thrust developed by the rotor. This means that a good accuracy is not indispensable, in the sense that this method would be used only to check if an hypothetical improved blade is better than the actual one.

One thing that instead plays against the rotor model is the fact that only transient simulations are possible with this model. As already explained, transient simulations require more time than steady state ones but are more accurate.

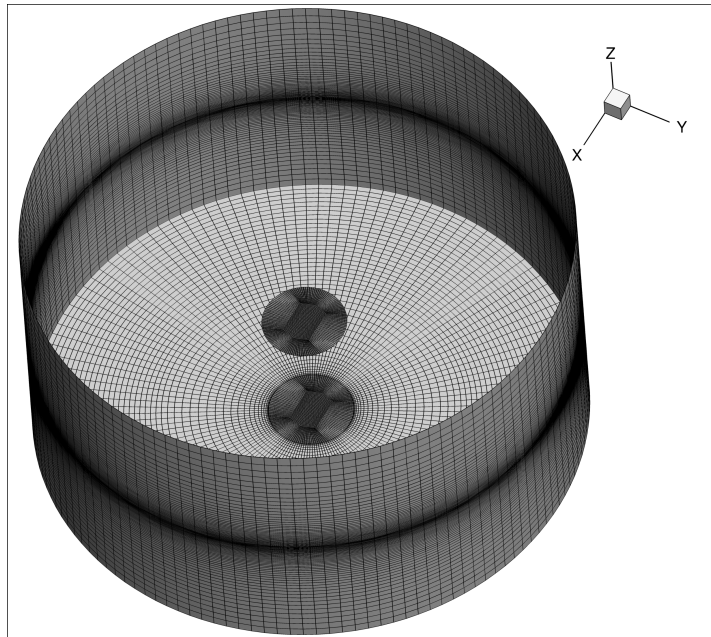


Figure 4.7: Grid constructed for the rotor model simulation.

In a transient simulation it necessary to set certain additional parameters, in these simulations the number of internal iteration per global time step has been fixed to 15, the global time step size is 0.0001 s and the global step inner iteration termination criterion is 0.001, this means that the inner iteration will stop when the residuals of the inner cycle reach the order of  $10^{-3}$ . What is missing to start the simulation are the information about the rotor and the boundary conditions:

1. Number of blades: 2;
2. Outer radius of rotor blades=0.229 m;
3. Hub radius of rotor blades=0.032 ;
4. Rotation speed of rotor blades=-3000 rpm;
5. Freestream velocity=0 m/s;

6. Pitch angle=32°;
7. Twist angle=0°;
8. Fluid density=0.0167 kg/m<sup>3</sup>;
9. Blade Chord=0.05 m;
10. Blade centre of rotation=[0, 0, 0];
11. Positive thrust direction: [0, 0, 1];
12. Azimuth datum direction: [-1, 0, 0].

The boundary conditions to impose are the classical inflow, outflow and farfield plus two boundaries which are the two disk surfaces. Each of the two disk surfaces has a zonal boundary condition (with *patched only* as zonal connection type) with the specification of the *rotor model* option. It is necessary to impose also the type of BC, which is *inflow only* for the lower part of the disk and *outflow only* for the upper part of the latter.

This specification, according to the CFD++ user manual, is made in following way: the inflow option assumes the flow is coming towards the current BC family from the other side, the outflow option assumes the flow is leaving the current BC family towards the other side. This specification is very important because if not applied in the right way the simulation would give wrong results, such as the flow going upwards and not downwards. The simulation solves the RANS equation with the two-equations realizable  $k - \varepsilon$  model.

## 4.4 Results

The blade is divided into three sections:

1. The first goes from the hub to the 33% of the blade span and presents the aerodynamic characteristic of the hub section, found with the 2D simulation ( $Re = 1.41e^3$ );
2. The second goes from the 33% to the 80% of the blade and has the characteristics of the medium section ( $Re = 4.22e^3$ );
3. The last one goes until the tip of the blade and has the performances of the tip section ( $Re = 6.75e^3$ ).

This distribution is more realistic than considering only one Reynolds number.

The calculation did not converge, probably because of the coarse grid, for this reason the grid is improved by adding some cells in the radial direction.

The resulting grid has 900000 cells, which is considerably more than the previous one but is anyway less than one fifth of the 3D model. After this modification, the simulation reached good convergence in few time steps and in about fifteen hours allowed to obtain a value of 0.132 N for the thrust and 0.0275 Nm for the torque. The thrust value is very different both from the 3D model and from the experimental case. Then this model seems not to be very effective for this type of flow, but what is important now is to assume this value as a reference

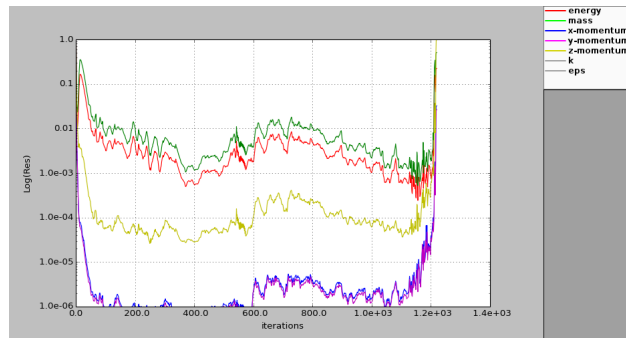


Figure 4.8: Residuals of the simulation which did not converge.

for the optimization that will follow in section 4.6.

Given the low thrust provided by the rotor, by taking a look at the velocity z-component it is clear that even the flow tube has difficulty to develop due to the low portion of air pulled down by the blade (figure).

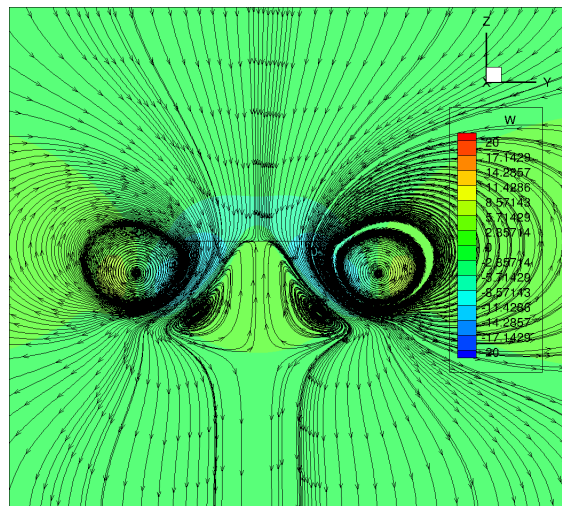


Figure 4.9: Velocity field for the rotor model simulation with the non-optimized blade.

## 4.5 Vortex theory

This section proposes another theory which represent a complement of the two theories exposed in the first parts of this chapter. The main aim is to follow the work done by Domenico Zaza in his bachelor degree thesis [36], where an optimization tool is implemented, and verifying with CFD simulations that it effectively improves the blade performances.

N. E. Joukowski laid the foundations of the vortex theory, investigating the induced velocity due to the helical wake system of a propeller, using the infinite blade model because of the mathematical complexities. Then, A. Betz determined the minimum induced power and the

best thrust distribution and L. Prandtl found a correct approximation for the optimal circulation distribution to account for the finite blades number.

It is useful to remind some basic formulation that will be used during this chapter:

- Biot-Savart's law:

$$d\vec{V} = \frac{\Gamma}{4\pi} \frac{d\vec{s} \times (\vec{r} - \vec{r}_0)}{|\vec{r} - \vec{r}_0|^3}$$

is the induced velocity in a generic point  $P(\vec{r})$  from an infinitesimal vortex in  $\vec{r}_0$ , with intensity and length respectively  $\Gamma$  and  $d\vec{s}$ ;

- Kutta-Joukowski's theorem:

$$L = \rho V \int_0^R \Gamma(r) dr$$

- Helmholtz's theorems:

1. The strength of a vortex filament is constant along its length;
2. A vortex filament cannot end in a fluid, it must extend to the boundaries of the fluid or form a closed path;
3. In absence of rotational external forces, a fluid that is initially irrotational remains irrotational.

- Vorticity equation:

$$\frac{D\vec{\omega}}{Dt} = \vec{\omega} \cdot \Delta\vec{V}$$

As already showed in equation 4.25 (in this case the rotor disk is in the infinite-blade approximation), it is possible to write  $dT \approx dL$  and  $U \approx \Omega r$ , with these the Kutta-Joukowski relation can be rewritten as  $dT \approx \rho \Omega r \Gamma(r) dr$  which can be divided by the infinitesimal disk area to obtain the disk load

$$\frac{dT}{dA} = \frac{\rho \Omega \Gamma(r)}{2\pi}$$

The simplest vortex theory is the one which refers to the actuator disk so, as the flow is irrotational in the far upstream, according to the vorticity equation, it must be irrotational until it crosses the disk, where the axial velocity is continuous while the tangential component presents a discontinuity depending from the radius, meanwhile on the flow tube outside vorticity is always zero. If the circulation is constant along the blade (along the  $r$  coordinate), which corresponds to uniform loading, vorticity is trailed into the wake only from the blade root and tip. The tip vortex is trailed in a helix because of the combination of the blade motion and the axial velocity of the flow through the rotor disk. The root vortices are trailed along the axis of the rotor in a straight line. The wake then consists of a vortex sheet at the boundary of the slipstream and a line vortex in the axis as showed in figure 4.10.

This model presents the following components:

- A vortex filament with intensity  $\Gamma$  aligned with the rotor axis;

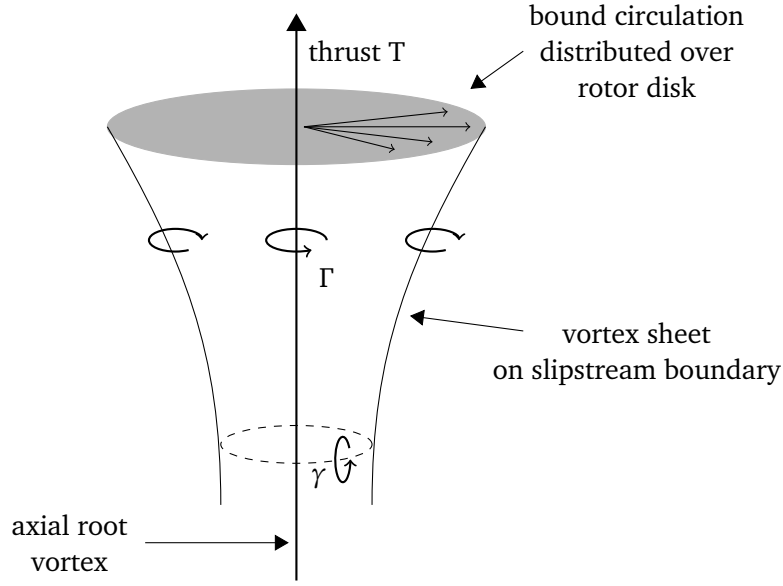


Figure 4.10: *Vortex theory for the actuator disk* (Draw adapted from [34])

- A radial distribution of vortex filaments on the actuator disk surface, which represent the vortices on the blades,  $\gamma_b = \Gamma/(2\pi r)$ ;
- A tube of vortex ring parallels to the blade plane whose strength is  $\gamma = \Gamma/h$  (this because the tip vortices have a helical geometry), where  $h$  is the distance the wake moves during one rotor revolution and it can be related to the axial velocity giving

$$h = (2\pi v)/\Omega \quad (4.31)$$

consequently  $\gamma = T/(\rho Av)$ ;

- Vortex filaments, which represents the axial component of the tip vortex sheet, with intensity  $\gamma = \Gamma/2\pi R$ , where  $R$  is the radius of the wake.

The root vortex induces a tangential velocity given by  $u_r(r) = \Gamma/(4\pi r)$  while the radial distribution of vortex filaments induces a tangential velocity  $u_b$  just below the disk and  $-u_b$  just over the disk. Given the requirement of no swirl outside the wake then it follows that  $u_b = 2 \cdot u_r = \Gamma/(2\pi r)$  and in the far downstream  $u = u_r = \Gamma/(4\pi r) = u_b/2$ .

Let's consider now the relation 4.31, here the disk induced velocity  $v$  appears. It is demonstrated a vortex ring distribution with density  $\gamma$  generates a velocity potential in a point P on the disk

$$\phi_P = \frac{\gamma}{4\pi} \int_{z_0}^{z_1} \omega dz \quad (4.32)$$

where  $\omega$  is the solid angle in P subtended by the vortex ring in  $z$ , while  $z_0$  and  $z_1$  and are the distribution extension. From the velocity potential definition the axial induced velocity can be obtained

$$v(P) = \frac{\gamma}{4\pi} \int_{\omega_0}^{\omega_\infty} d\omega \quad (4.33)$$

Knowing that the disk is at  $z = 0$ , then  $\omega_0 = \omega(z = 0) = 2\pi$  and  $\omega_\infty = \omega(z = -\infty) = 0$  it follows that for any point on the disk

$$v(P) = \sqrt{\frac{T}{2\rho A}} \quad (4.34)$$

For a point in the far wake  $v_\infty = 2v$ , which is the same result found in the momentum theory. The case just exposed was with a constant radial circulation distribution, now let's focus on an actuator disk with *non uniform loading*. Every time the intensity  $\Gamma$  varies, a vortex filament leaves the blade, the sum of all these filaments gives a swirling helical surface carried by the fluid to the entire wake. These surfaces generate an angle with the disk's plane given by [36]

$$\phi = \arctan\left(\frac{v}{\Omega r - u/2}\right) \quad (4.35)$$

with  $v$  and  $u$  respectively the axial and tangential induced disk velocity.

It is possible to demonstrate that, by applying the Bernoulli's law to the streamlines, the pressure discontinuity ( $\Delta p$ ) through the disk is

$$\Delta p = \rho \left(2v^2 - \frac{u^2}{2}\right)$$

Through this relation it can be obtained the infinitesimal thrust

$$dT = 2\pi\rho \left(2v^2 - \frac{u^2}{2}\right) r dr$$

according to the Kutta-Joukowski's law it can be written

$$dT = \rho V \Gamma dr = \rho \left(\Omega r - \frac{u}{2}\right) \Gamma dr \quad (4.36)$$

By equating these two last relation and remembering that  $u = \Gamma/(2\pi r)$ :

$$\Gamma(r) = \frac{4\pi v^2}{\Omega} \quad (4.37)$$

#### 4.5.1 Wake structure for optimum rotor

The optimum condition is the one where the induced power is at its minimum, this problem was solved by Glauert. The rotor is still considered as an actuator disk with the approximation of infinite number of blade.

The minimum induced power condition requires the swirling surface to rotate about the axis like a rigid surface and to form horizontal planes with constant  $\phi$ . This wake type pulls the fluid downstream giving the fluid a velocity normal to the surface itself. This velocity can be decomposed in a tangential and in an axial component.

It can also be written

$$\phi \approx \arctan\left(\frac{v}{\Omega r}\right) \quad (4.38)$$

As the infinitesimal induced power is  $dP = dT \cdot v$ , remembering the 4.36 it follows that

$$dP = 2\pi\rho \left( \Omega r - \frac{u}{2} \right) u r dr \cdot v \quad (4.39)$$

where  $v = \Omega r \tan \phi$  (from 4.38). Glauert obtained an equation for the minimum induced power computation which, in hovering condition, reduces to a cubic which can be solved in a closed form [37]:

$$\bar{\omega} = \frac{6}{5 + \bar{r}^2 + 2(1 + \bar{r}^2) \cos(\theta/3)} \quad (4.40)$$

$$\theta = \arccos \frac{\bar{r}^6 + 3\bar{r}^4 + 3\bar{r}^2 - 1}{\bar{r}^6 + 4\bar{r}^4 + 3\bar{r}^2 + 1} \quad (4.41)$$

where  $\bar{\omega}$  is the adimensional angular velocity  $\bar{\omega} = \omega/\Omega$ ,  $\omega = u/r$ ,  $\bar{r} = r/(RG)$  and  $G$  is the Glauert's load parameter which is determined by imposing a rotor thrust. From the tangential velocity formulation it is possible to find the circulation  $\Gamma = 2\pi r u(r)$  and knowing that  $u = \omega r = \bar{\omega}\Omega r$  it follows:

$$\Gamma(r) = 2\pi\bar{\omega}\Omega r^2$$

While the adimensional circulation is

$$\bar{\Gamma}(r) = \frac{\Gamma(r)}{2\pi\Omega R^2 G^2} = \bar{\omega} \left( \frac{r}{RG} \right)^2$$

#### 4.5.2 Prandtl's tip correction

So far the rotor has been considered with a infinite number of blades.

The main effect of considering finite the number of blades is a reduction of the forces developed at the blade tip. In fact, there is a flow from the lower surface to the upper one that reduces the total downward momentum. This phenomenon can be considered as a loss, in fact it is often called *tip loss* and its consequence is the annulment of the blade's lift and circulation near the tip. Prandtl found a coefficient,  $F$ , which can be used to account for this effect, it is defined as:

$$F = \frac{2}{\pi} \arccos \left( \exp^{-f} \right)$$

where  $f$  is

$$f = \frac{N(R-r)}{2r\phi}$$

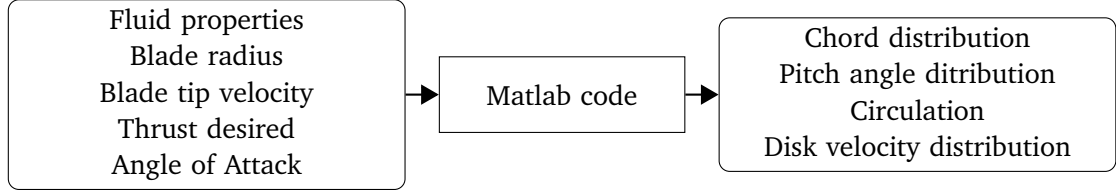
with  $N$  the number of blades.

This coefficient can be inserted in the circulation formulation to obtain a corrected value to account for the finite number of blades. Obviously, the bigger is the blade number, the closer are the circulation values to the infinite blades case. The coefficient has unitary value until it approaches the blade's tip, where it reaches zero. Given this, it is sufficient to insert the coefficient in the adimensional circulation formula to obtain the corrected value

$$\bar{\Gamma}_{corr} = \frac{2}{\pi} \arccos \left( \exp^{-\frac{r-R}{r\phi}} \right) \bar{\omega} \left( \frac{r}{RG} \right)^2$$

## 4.6 Optimization

A simple code, written with MATLAB, is obtained following the theories previously exposed and following the guidelines given in [36].



The approach is to impose a value of thrust desired to find the value of the Glauert's parameter,  $G$ , and then to find the correct circulation along the blade span. So the number of blades, the thrust, the blade radius and tip velocity are set as input, the code through an iterative process finds the thrust value imposing an arbitrary value for  $G$ . The cycle is repeated (increasing the value of  $G$  every time cycle is repeated) as long as the thrust found in the iteration is lower than the value imposed by the user; when the two values are equal, the cycle is stopped and the value of  $G$  is found. The thrust is found using the relation written in the preceding sections:

1.  $\tilde{r} = \frac{r}{RG}$
2.  $\theta = \arccos \frac{\tilde{r}^6 + 3\tilde{r}^4 + 3\tilde{r}^2 - 1}{\tilde{r}^6 + 4\tilde{r}^4 + 3\tilde{r}^2 + 1}$
3.  $\bar{\omega} = \frac{6}{5 + \tilde{r}^2 + 2(1 + \tilde{r}^2)\cos(\theta/3)}$
4.  $\omega = \bar{\omega} \cdot \Omega$  with  $\Omega$ , being the rotation velocity
5.  $v_0 = \Omega \cdot r \cdot \sqrt{\frac{\bar{\omega}}{2 - \bar{\omega}}}$
6.  $\phi = \arctan\left(\frac{v_0}{\Omega \cdot r}\right)$
7.  $\bar{\Gamma}_{corr} = \frac{2}{\pi} \cdot \arccos\left(\exp^{\frac{r-R}{r\phi}}\right) \bar{\omega} \left(\frac{r}{RG}\right)^2$
8.  $f = \frac{N}{2} \cdot \frac{R-r}{r\phi}$
9.  $F = \frac{2}{\pi} \cdot (\exp^{-f})$
10.  $\bar{\Gamma} = \bar{\omega} \cdot \tilde{r}^2$
11.  $\Gamma = \bar{\Gamma} \cdot 2\pi\Omega R^2 G^2$
12.  $\Gamma_{corr} = F \cdot \Gamma$
13.  $u(r) = \frac{\Gamma_{corr}}{2\pi r}$

$$14. v(r) = \frac{1}{2} \sqrt{\frac{\Gamma_{corr} \cdot \Omega}{\pi}}$$

$$15. dT = \frac{1}{2} \rho \sqrt{(\Omega r - u/2)^2 + v^2} \cdot \Gamma_{corr} dr, \text{ where } dr \text{ is the distance between each station considered}^4.$$

$$16. T = \sum_i (N \cdot dT), \text{ where } i \text{ goes from 1 to the number of stations.}$$

Following this procedure it is possible to find the circulation and the tangential and axial velocity at the disk section. With these two velocities it is possible to find the inflow angle  $\phi$ , which summed to the alpha angle (angle of attack) gives  $\theta$ , the pitch angle. In fact,  $\phi$  has been defined in equation 4.35, (see also figure 4.3). Now, to find the correct values of the pitch angle it is necessary to make an assumption: *every blade section works at a specified angle of attack, which is chosen by the user*. The angle of attack is chosen in order to have the maximum efficiency at the blade section, then the pitch angle is

$$\theta = \alpha + \phi$$

To find the chord distribution it is necessary to make another approximation, in fact, as the angle of attack of the section is chosen, also the lift and drag coefficient are fixed. While  $\alpha$  is the same for all the blade sections, the coefficients vary due to the different Reynolds numbers. The assumption made is to consider only one value for the lift and drag coefficient for all the blade, this is acceptable because the blade is not large and the Reynolds number remains very low even for the tip section. It is possible then to calculate the chord distribution with the following formula

$$c(r) = \frac{2dT/dr}{\rho \cos \phi (\Omega r)^2 C_l}$$

The program outputs can be visualized in figure 4.11. It computes a large chord value near the hub because in this way more thrust is produced where the blade section faces a lower velocity. Also the pitch angle is very large at these section to optimize the poor efficiency. In fact, in the previous blade, these sections were quite useless in terms of thrust generation. Obviously, these parameters define a blade with a very particular geometry (by looking at the chord, it reaches the 70% of the blade span) which needs also some verifications by a structural point of view. But at this design stage what is important is the aerodynamic performance, not the structural behaviour. The latter can be done once the blade thrust improvement has been proved.

#### 4.6.1 Rotor model

Now that the new blade geometry is known, it is possible to go on with the rotor model analysis to find out if this configuration is better than the previous one (and if the code implemented is useful to this purpose). As previously said, it is not expected the model to be accurate, what is expected is an increase in the thrust developed by the blade, in order to proceed with the creation of a 3D model.

---

<sup>4</sup>The blade is divided into a certain number of station in which thrust is calculated, the more are the station, more accurate will be the calculation.

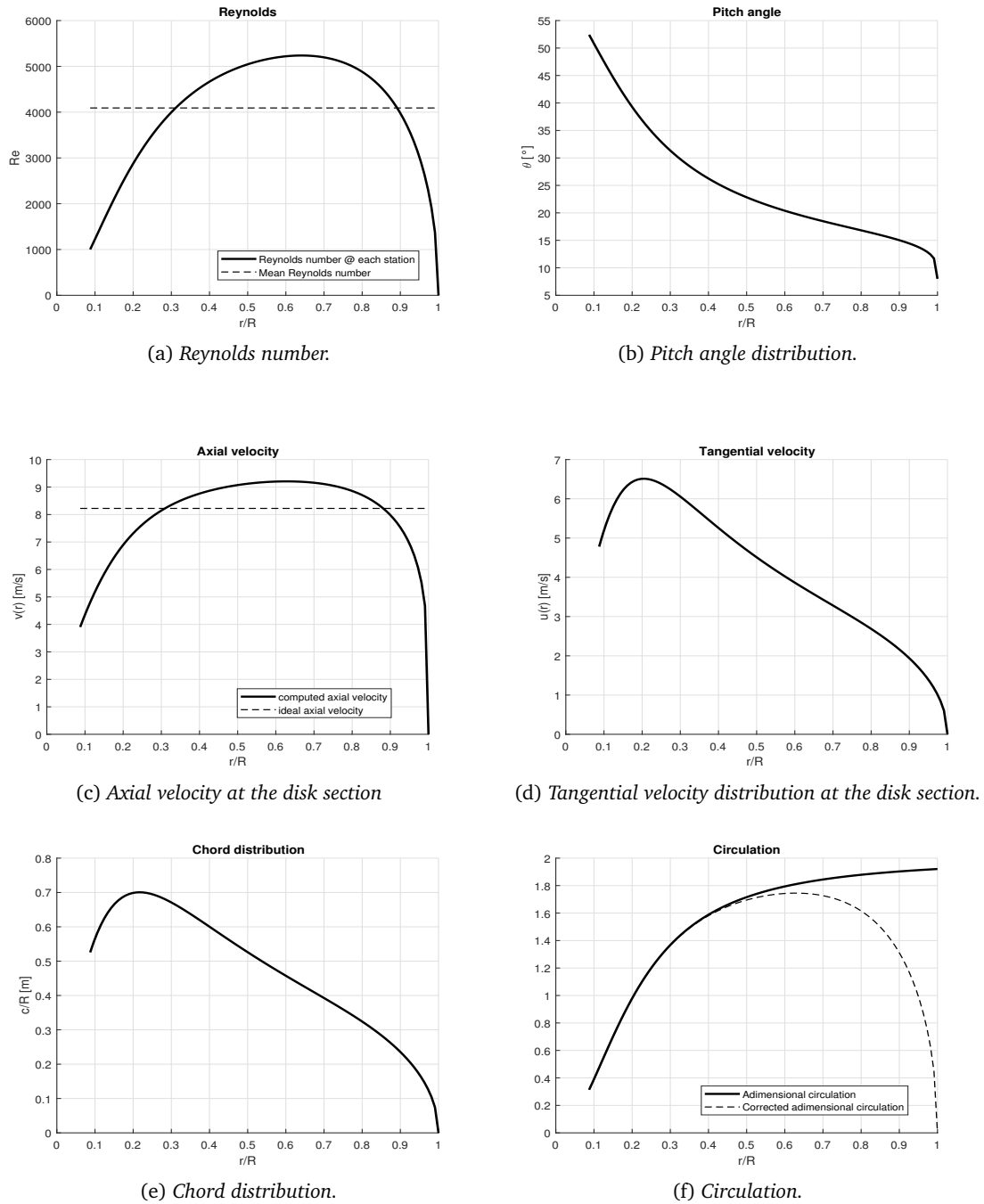


Figure 4.11: Matlab program outputs.

The grid is the same used in section 4.4 for the non optimized rotor with the same condition. The only difference is in the blade pitch angle and chord distribution: a value of  $0.307 N$  is

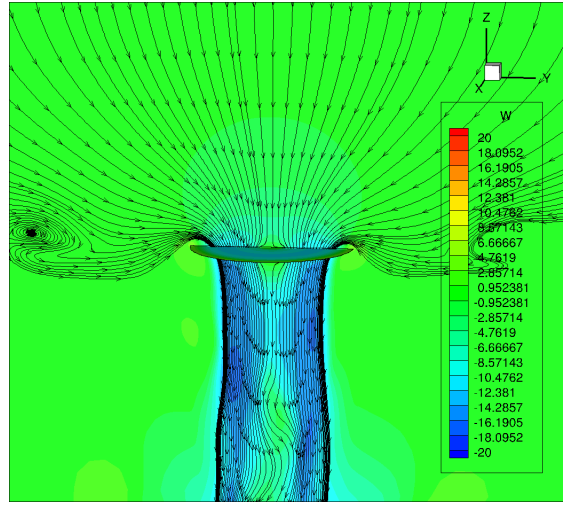


Figure 4.12: Velocity field of the optimized rotor model.

obtained for the thrust. The fact that the blade is more performing is suggested also by the flow visualization, in fact in this case it is clearly visible the flow tube under the blade indicating that the blade is pulling down the flow more intensively than the previous case where the flow tube was barely visible.

The rotor model analysis suggest that the new blade is more performing than the other one so it is possible to proceed with the implementation of a 3D model to find out how much is more performing and to validate the optimization tool used to design the blade.

#### 4.6.2 3D model

To realize the new grid it is necessary to have the CAD model of the blade on which the mesh can be built. As previously said, the new blade has the same airfoil of the previous one so the new geometry can be simply obtained by extrapolating the airfoil coordinates from the previous grids and rotate and scale it for different sections along the blade span in order to assign the pitch angle and the right chord.

It is chosen to *rotate the section about its centre of gravity*; the rotation and the scaling of the sections can be made directly with a script on Matlab. To rotate the sections a rotation matrix is used (where the index  $i$  indicates each section)

$$\begin{bmatrix} \cos(\theta_i) & -\sin(\theta_i) & 0 \\ \sin(\theta_i) & \cos(\theta_i) & 0 \\ 0 & 0 & 1 \end{bmatrix}$$

while to scale it is sufficient to multiply each coordinate for the chord value (this supposing the section to have an initial chord of 1 m). Once the new sections have been obtained it is sufficient to insert them as connectors in Gridgen and then to generate the domains which give shape to the blade. With a specific tool these domain can be then transformed into CAD entities.

The new blade is very different from the previous one, its particular shape makes really difficult and time consuming building a fully structured mesh. For this reason it is chosen to have a structured mesh on the blade surface, to extrude these surfaces in order to catch appropriately the boundary layer and to have an unstructured mesh for the rest of the grid (figure 4.13). Using this technique should reduce considerably the time to realize the grid and should at the same time give good results accuracy.

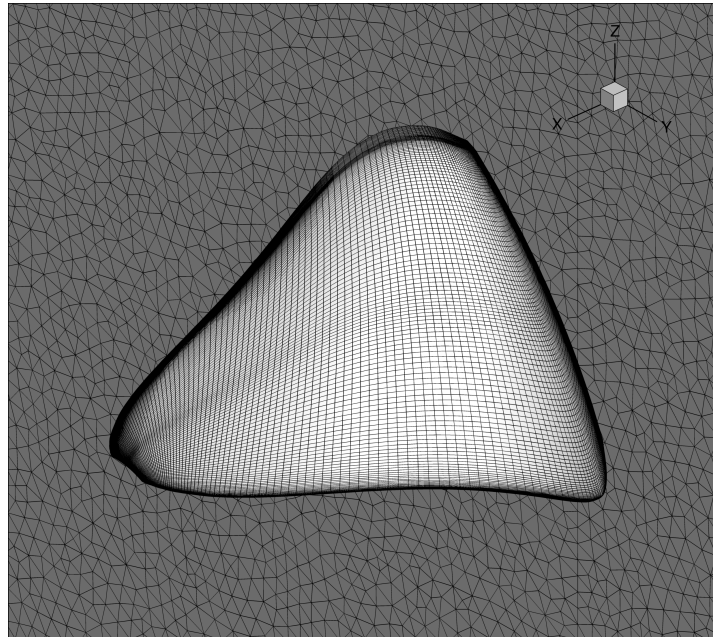


Figure 4.13: Grid constructed with the new optimized blade.

The considered case is *free flight* condition so the grid must be extended far upstream and far downstream the blade. It is important to have a smooth transition from the structured extruded block near the blade and the unstructured grid right near to it or the calculation will have difficulty to converge.

In this case the hub is not modelled, this is made to have a faster mesh generation process, in fact the intersection between the blade and the hub surfaces would generate very distorted cells affecting the convergence. Anyway, the hub absence does not have a significant impact on the thrust developed by the blade, this because it would be collocated immediately near the centre of rotation and the blade sections which would be erased, would face a very slow flow which would not develop considerable forces.

The grid has about 4 millions cells and is run with the same specifications of the simulation done in section 2.1.2. The calculation converged in relatively few iterations giving unexpected results. In fact the thrust developed by the blade is quite the same of the previous one (slightly lower) counteracting the previsions made with the rotor model.

The new optimized blade is did not give the results expected in terms of thrust (only  $\simeq 2\%$  more than the non-optimized blade) but at least decreased the torque and the drag, this decreases

the power<sup>5</sup> needed to the rotor to operate.

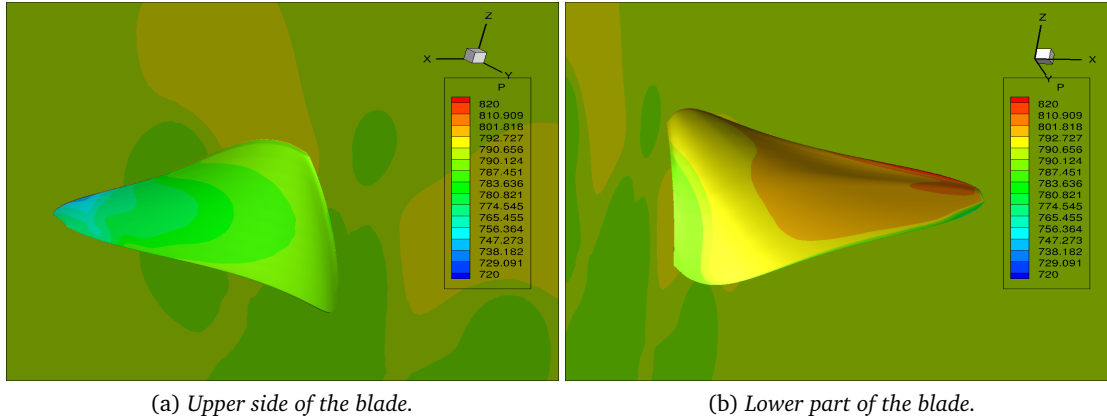


Figure 4.14: Pressure distribution on the optimized blade.

In such sense given the same power the new blade can rotate at a higher velocity, allowing to have a higher thrust. Obviously the rotational velocity cannot be increased too much due to the rise of compressibility effects and the transonic/sonic condition. Apart from this, the results obtained are not satisfactory because a more consistent increase in the thrust produced was expected. To explain this results, it is possible to look at the pressure distribution in figure 4.14. Despite having a much bigger chord near the hub, due to the low velocity that face these sections, the pressure distribution shows that there are no significant variations so this modification seems to be useless, because it also makes the blade heavier and the weight is a critical parameter that must be taken as low as possible.

Going to the blade tip instead shows that the pressure variation is not consistent as it was in the non optimized blade. The main problem is that going towards the tip the pitch angle decreases as the chord so at the tip the blade has a lower pitch angle and a lower or equivalent chord than the previous blade.

By taking a look at picture 4.15a it can be noted that for nearly 70% of the blade span, the pitch angle is lower than the one of the previous blade while the chord is considerably incremented, especially near the hub where the force generated is low.

It must be remembered that the pitch angle starts from the alpha value, inserted by the user in the optimization tool, at the tip. This value has been chosen to have the best efficiency of the airfoil and this is respected in the blade, because in fact the drag is drastically reduced and so the torque. So it is legit to try with another value of alpha, this time it is chosen a value to which corresponds the maximum value of section's lift coefficient as the goal now is to maximize the thrust and not the efficiency. With a value of  $\alpha = 24^\circ$  now the risk is to have a too much higher pitch angle (because the twist angle is the same of the previous case). The

<sup>5</sup>The power is defined as  $P = Q\Omega$ , where  $Q$  is the torque and  $\Omega$  is the rotational velocity.

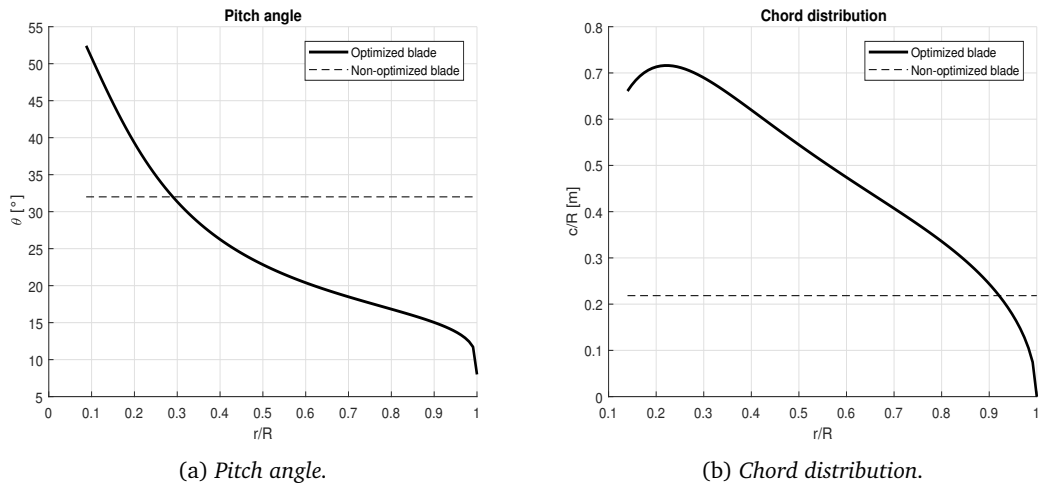


Figure 4.15: Comparison between the new and the non-optimized blade.

new blade in fact has a pitch angle that reaches  $68^\circ$  near the hub.

In figure 4.16 is displayed the pressure distribution on both sides of the blade and here it can be seen much larger suction and overpressure zones. In fact, the blade develops a thrust of  $0.275\text{ N}$  which is  $\approx 14\%$  more than the non-optimized blade. Anyway this lift increment has a cost, because also the drag and the torque are very increased ( $0.194\text{ N}$  and  $0.029\text{ Nm}$  respectively for drag and torque). This does not surprise because this time thrust has been maximized without taking care of the drag.

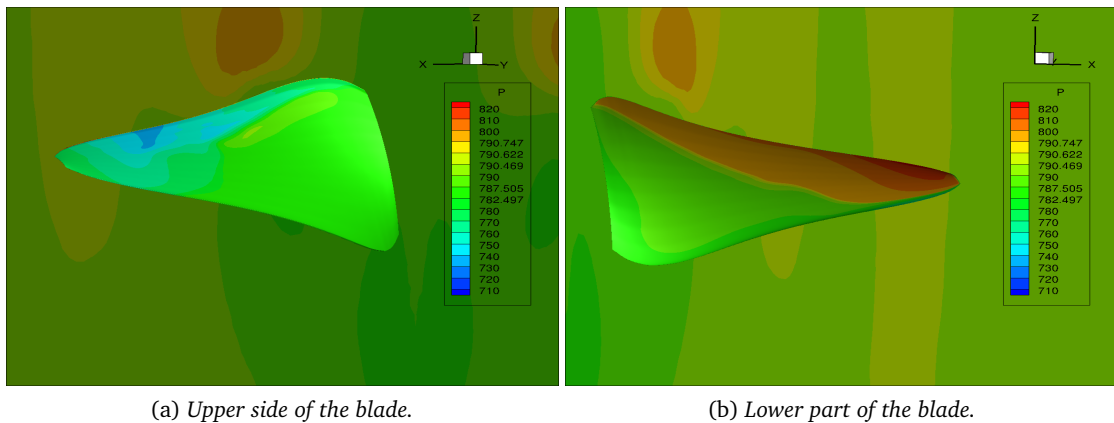


Figure 4.16: Pressure distribution on the optimized blade with a different pitch angle distribution.

In [39] can be found an analysis of a similar blade of the one used by JPL for the MHS. The blade is scanned with the help of a 3D optical laser scanner to extract the geometrical characteristics and to analyse the airfoil with the help of CFD.

Despite having a much larger radius, the blade presents a similar geometry to the one implemented by the optimization tool (in [40] can be found some more detailed photos of the rotor), in fact it has an important pitch angle and a very exotic shape (due to the higher radius it appear slimmer than the blade just implemented).

Apart from this, to understand better how the *initial value of alpha* affects the blade which is generated, also other two blades are implemented: the first starting with  $\alpha = 16^\circ$ , the second with  $\alpha = 20^\circ$  as starting value. The results found reveal that even if the blade with a starting angle of  $\alpha = 24^\circ$  has been optimized to reach the maximum value of thrust, these two last blades have not only a better thrust, but also a better "efficiency". In fact, they have lower values of drag and as a consequence of torque (table 4.2).

	Thrust [N]	Drag [N]	Torque [Nm]
Non-optimized blade	0.2413	0.132	0.0227
Optimized blade $\alpha = 8^\circ$	0.246	0.09	0.0126
Optimized blade $\alpha = 16^\circ$	0.314	0.155	0.024
Optimized blade $\alpha = 20^\circ$	0.312	0.187	0.028
Optimized blade $\alpha = 24^\circ$	0.275	0.194	0.029

Table 4.2: Results obtained with different optimized blades.

From the results it is possible to see that the blade with a starting value of  $\alpha = 16^\circ$  is better not only in terms of thrust but also in terms of torque so of all the four blades implemented is the more indicated to improve the rotor performances (it has to be remembered that all these values of force and torque are relative to only one blade).

To have a better idea it is possible to define a index, a sort of *blade efficiency* by simply dividing the thrust developed by the drag.

	incr. % $T$	incr. % $D$	incr. % $Q$	E (T/D)
Non-optimized blade	ref.case	ref.case	ref.case	ref.case
Optimized blade $\alpha = 8^\circ$	1.947783	-31.818	-44.4934	2.733333
Optimized blade $\alpha = 16^\circ$	30.12847	17.4242	5.7268	2.025806452
Optimized blade $\alpha = 20^\circ$	29.29963	41.6667	23.34802	1.668449198
Optimized blade $\alpha = 24^\circ$	13.96602	46.9697	27.7533	1.417525773

Table 4.3: Percentage performance improvement compared to the first optimized blade.

In table 4.3 are listed the percentage variations in terms of thrust, drag and torque respect to the blade non-optimized: from this table it is easy to see how much efficient is the case with initial value  $\alpha = 8^\circ$ , in fact all the other cases present an increment in terms of lift but have to pay an important price in terms of drag and torque. It must be remembered that increasing the torque needed to move the blade, increases the weight of the motor required. This is a crucial aspect because it means that increasing the thrust available increases also the weight to be lifted and this last element must be kept as low as possible to have a relevant payload. The flow behaviour on the blade remains the same even if the geometry is changed, this is confirmed by the presence of the leading edge vortex (figure 4.17). In parallel to this analysis,

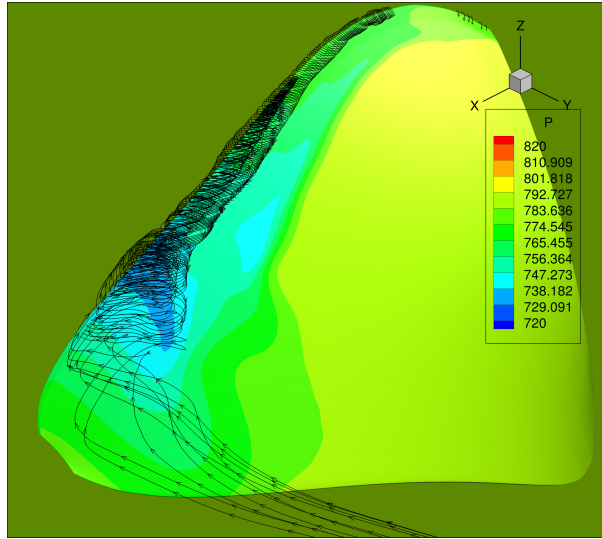


Figure 4.17: *Leading edge vortex on the optimized blade.*

also the rotor model has been used with results not really satisfactory. In fact, the case run in section 4.6.1 showed a great difference in terms of lift between the non-optimized and the first blade implemented. This difference did not emerged in the 3D model, but at least there was an increment (even if really small) in the optimized case.

As other blades are tested with the 3D model, it is decided to try again the rotor model and the results can be found in table 4.4 It turns out that the rotor model can not be used to predict

	Thrust [N]	Torque [Nm]	incr. %_T	incr. %_Q
Non-optimized blade	0.132	0.0275	ref. case	ref. Case
Optimized blade 8alpha	0.307	0.0164	132.5757	-40.3636
Optimized blade 16alpha	0.3	0.0227	127.2727	-17.4545
Optimized blade 20alpha	0.287	0.0259	117.4242	-5.81818
Optimized blade 24alpha	0.285	0.0285	115.909	3.6363

Table 4.4: *Rotor model results.*

the performance of the rotor. It is true that it predicted an increase of thrust in the optimized cases respect to the non-optimized one but it is not possible to make a comparison between the optimized cases. In all cases anyway the thrust is very different from the one encountered in the 3D model: this is due to three-dimensional effects (such as the leading edge vortex) that play an important role in the very low-Re flow. These effects are not captured by the simple rotor model, which is based in BEMT theory.

A similar thought can be made for the optimization tool, because as the rotor model it is also based on BEMT theory. The blades implemented are all better than the initial one, but there is not a criterion which can be applied to know which is the better value of  $\alpha$  to use. Anyway, the aim was to validate that the tool effectively increase the blade performance and this is verified. It is due to the CFD analyst the choice of which  $\alpha$  value is better.



## Chapter 5

# Conclusions

In the first part of the work many simulations of the Martian rotor have been done. The main goal was to get as close as possible to the experimental results obtained in the vacuum chamber but, as anticipated previously, this has not been achieved. To be fair, it has to be remembered that there are several factors that play a crucial role in the differences encountered between the results.

First of all, the accuracy of the results obtained in the vacuum chamber: this is the most important factor as the experimental results are the point of reference of all the CFD simulations. It must be said that they are quite similar to the results obtained by Maryland University but the massive noise encountered in the measures indicates that a more accurate solution can be reached.

Another point is the CAD model: all the geometry is been simplified and this can lead obviously to approximation errors. The whole structure that supports the rotor is really complex and for sure all the cables and the horizontal setup have an effect on the flow. In particular the cables which sustain the rotor are subject to important vibrations (which affects also the measurement) starting from 2700 rpm.

Lastly, the reduced vacuum chamber's dimensions lead to important aerodynamic interference and recirculation effects that could not be caught by the turbulence models.

In any case, the results show that in the best case there is an error respectively of the 35% and of the 6% for thrust and torque. These results are not satisfactory as they tend to overestimate the blade performances. It is worth to mention the fact that the two cylinders collocated in the wake of the blade do not have influence on the flow behaviour, probably because of the low density and high flow viscosity. Following transient simulations, it is observed also a vortex shedding from the blade which is responsible for forces oscillations. This vortex in particular is stably attached in the first half of the blade and it becomes to be unstable once the three quarters of the blade are reached.

Furthermore, it must be taken into account the increment in thrust given by the rotor operating in  $CO_2$  and not in air.

In the second part, the optimization tool is tested. Despite being based on quite strong assumption (for example the flow has to be inviscid and stall is neglected), the tool gave the results expected: the optimized blade is better in terms of thrust generation. Anyway, there are few tips to follow. The angle of attack inserted in the tool plays a meaningful role and,

for this reason, it must be selected from the 2D analysis of the airfoil depending on the aspect which needs to be optimized: thrust or efficiency.

In order to optimize the thrust it also has to be considered the pitch angle of the blade that can rise a lot, inducing the drag to increase. Meanwhile, efficiency improvement does not necessarily lead to a thrust increase, but can also be linked to drag reduction.

To support the optimization work carried out so far, also the Rotor Model tool from CFD++ has been tested. Despite having the advantage of a fast mesh creation process (that can be reused for other cases, given the same rotor radius), the model did not give the expected results.

The model was validated for some other cases in the CFD++ user guide and supposedly failed in these simulations because of the low-Re flow, which involves viscous effect not captured by the BEMT.

Moreover, this work has proved that it is possible to apply a few modifications to the experimental setup in order to obtain a better correlation with the CFD model. Furthermore the optimization tool, which allows to have a more performing blade, has been validated and can be useful for upcoming activities.

Future works will deal with the optimization of the airfoil which, together with the tool tested in this thesis, will give a proper blade design. All the design process will need to consider that the 3D model overestimates the forces developed.

Eventually, a very last factor that could support the improvement of the correlation between numerical simulations and experimental tests consists in repeating the test in a different vacuum chamber. In fact the use of a vertical setup could help to reduce oscillations and to achieve more accurate results.

## Appendix A

# Structured and Unstructured grids

A *structured grid* is composed of families of intersecting lines, one for each space dimension (two families of lines in 2D and three in 3D), where each mesh point is located at the intersection of one line, and only one line, of each family. *Unstructured grids*, on the contrary, refer to arbitrary distributions of mesh points, where the points are connected by triangles, quadrilaterals or polygons in 2D, or by various polyhedra in 3D (tetrahedra, prisms, pyramids, hexahedra or arbitrary polyhedra) [8].

Structured grids are, compared to unstructured grids, more efficient in term of accuracy, convergence and CPU time. Unstructured grid are anyway used because it is easier to realize these type of grid, especially for complex geometries and this fact can make the difference in terms of time required to build the grid.

The ideal mesh has a Cartesian distribution, which means that all points are equidistant and all the cells are cubes, with all sides congruent. This type of distribution not always can be implemented as curved surfaces can be present in the model to be discretized: in this case it is necessary to introduce curvilinear grids. These type of grids are called *body fitted* (figure A.1).

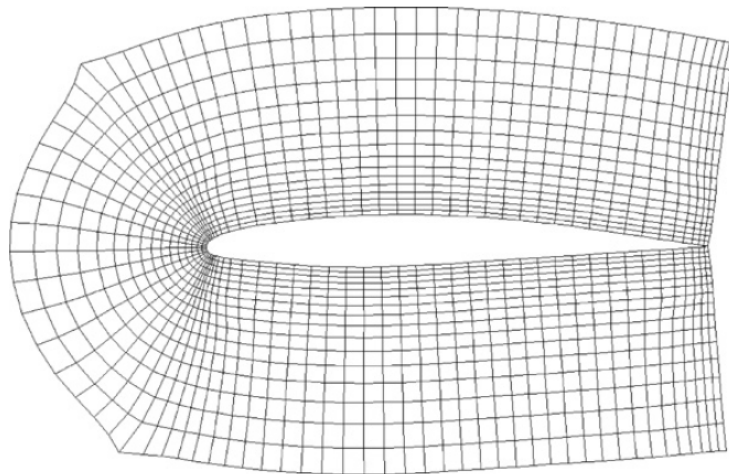


Figure A.1: Example of a structured C-type mesh around an airfoil[8]

As the construction of structured grids can be very time consuming, multi-block grids are a solution: they are formed of sub-domains with their own structured grid. This leads to *non-matching boundaries*<sup>1</sup> which can be managed by many CFD software.

An alternative to body fitted grids are *non-uniform Cartesian* grids: as the former they can be used when are present curvilinear surfaces.

As already said, unstructured grids (figure A.2) are easier to improve and for this reason have progressively become the dominating approach to industrial CFD. Another advantage is the possibility to perform local refinements in a certain region without affecting the grid point distribution outside that region.

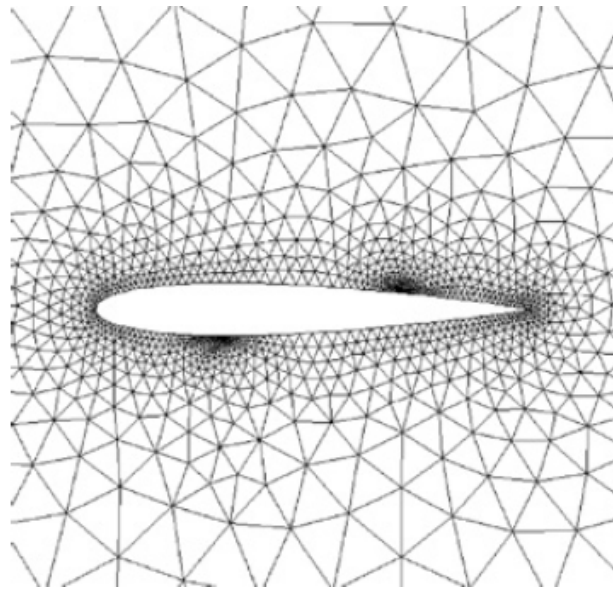


Figure A.2: Example of an unstructured mesh around an airfoil[8]

A third group of grid is called *hybrid grid*, this consists simply of the combination of structured and unstructured grids. Often they are used when the flow needs to be investigated in the boundary layer (structured grid) but in the rest of the domain it is desirable to have a faster mesh generation process (unstructured grid). Related to the example of the airfoil considered in the two figures above, a hybrid mesh could be made of some layers of structured grid near the airfoil and then when a certain  $y^+$  coordinate is reached the grid can switch to unstructured (figure A.3).

One thing that worth to remember is to have a continuous variation of the cells dimension in all the direction, having discontinuities will cause a decrease in terms of accuracy and convergence velocity. This aspect must be considered also when switching from structured to unstructured cells.

Another tip involves cells distortion and concave cells, the latter ones in particular tend to

---

<sup>1</sup>At one interface between two blocks, the mesh of one sides of the interface is different from the one on the other side.

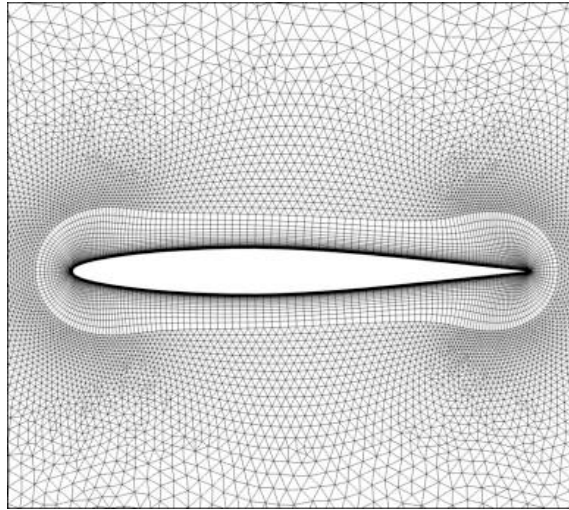


Figure A.3: *Example of a hybrid mesh around an airfoil*[14]

make negative volume cells.

If even a cell has a negative volume then the solver will not even start because it is not able to find the normals to the cell's faces.



## Appendix B

# Experimental setup

In this section experimental results are briefly resumed to give the reader a better understanding of the comparison between CFD models and experimental results. The vacuum chamber (*PHASE*) has a cylindrical shape with horizontal axis made of stainless steel (figure B.1); its vacuum pump can get the chamber to about  $1 \cdot 10^{-1} \text{ mbar}$ . Inside, there are two movable  $600 \times 800 \text{ mm}$  steel plates mounted on sliding rails; for this experiment, one plate has been removed.

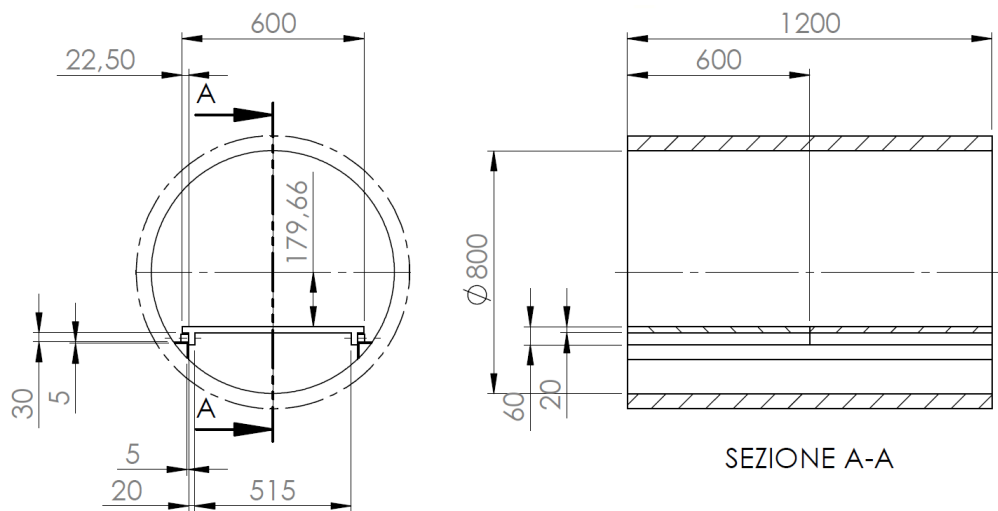


Figure B.1: *PHASE* vacuum chamber dimensions.[20]

Once the rotor has been mounted on the inferior plate, it is important to verify that the tips of the blades are sufficiently distant from the chamber walls, as the centre of rotation of the blade does not coincide with the centre of the vacuum circumferential section. In figure B.2 it is possible to see the sizes of the blades: the reduced distance between the blade tip and the wall will probably give some aerodynamic issues.

In fact, an important parameter used to estimate the influence of volume occupied by the

model is the following

$$C_b = \frac{A_m}{A_s} \cdot 100 = \frac{\pi r^2}{\pi R^2} = \frac{0.66476}{2.010} = 33\%$$

where  $A_m$  is maximum cross section of the model and  $A_s$  is the section of the chamber. So  $C_b$  is the percentage ratio between the two section and must be kept as low as possible.

The wall proximity to the blade tip is responsible also for an alteration of the angle of attack induced by the changing of the flow direction and of the flow lines curvature.

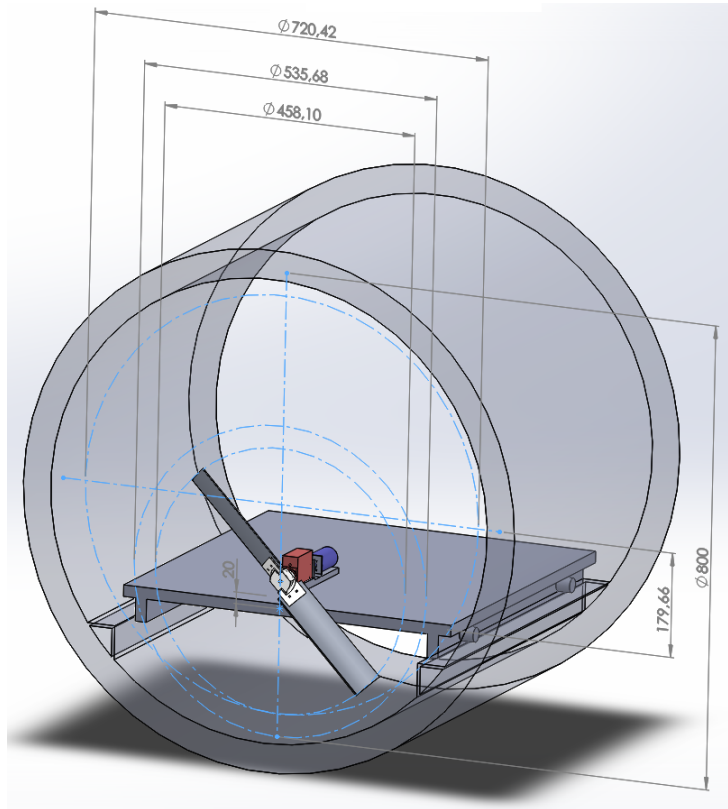


Figure B.2: *Experimental test setup dimensions.*[20]

The drawback of this facility is the limited internal dimensions, for this reason the aerodynamic turbulence created by the rotor affects negatively the whole setup producing a lot of vibrations and noise in the measures [21].

The limited space imposes also a compact design for the measurement instrumentation and various supports to the rotor: the setup is like a pendulum in order to measure the thrust and minimize any friction effect. In this way, the rotor is free to move along the axial direction but also along the lateral, this last degree of freedom let the rotor oscillate producing a lot of noise in the acquired data.

In the *PHASE* vacuum chamber is impossible to control the temperature, for this reason, to obtain the right air density ( $\rho = 0.0167 \text{ Kg/m}^3$ ) it is possible to set a particular pressure

value, using the ideal gas law  $p = \rho RT$ , where  $R = 287 \text{ J}/(\text{KgK})$  is the specific gas constant of the air.



Figure B.3: *Suspended setup within the vacuum chamber.*[21]

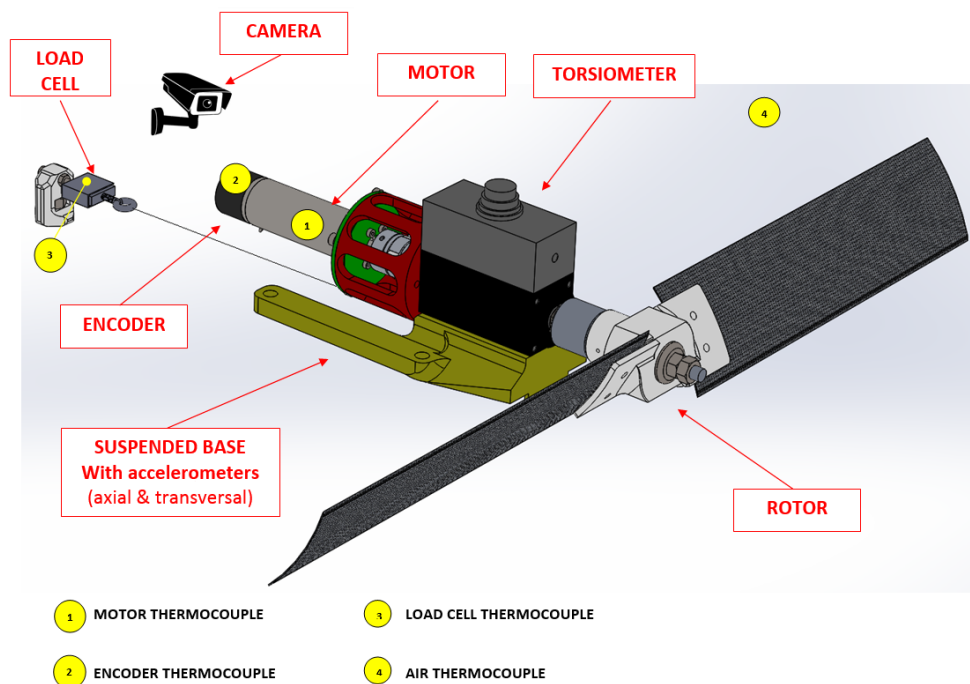


Figure B.4: *Schematic representation of the setup components.*[21]

## B.1 Results

The results obtained are displayed in figure B.5, at 3000 *rpm* the blade generates 0.27 *N* of thrust and 0.03 *Nm* of torque.

Due to motor temperature and chamber vibrations rising, the acquisition has been stopped at 3200 *rpm*, even if the main goal was to have experimental data in the range between 3000 and 4000 *rpm*. Anyway the simulation are run for 3000 *rpm* so data are available. One important fact that must be kept in mind is that experimental measures are affected by some errors, for this reason the simulation results don't need to accurately match these values. Apart from this, the z-force values follow appropriately the one obtained by the Maryland University with their rotor, from which is derived the rotor used in this experimental setup.

The torque instead has a slightly different value than the one obtained by Maryland University, this is due to some friction that develops on the transmission shaft. By fixing this issue, it is more likely to reach the torque value obtained by Maryland University.

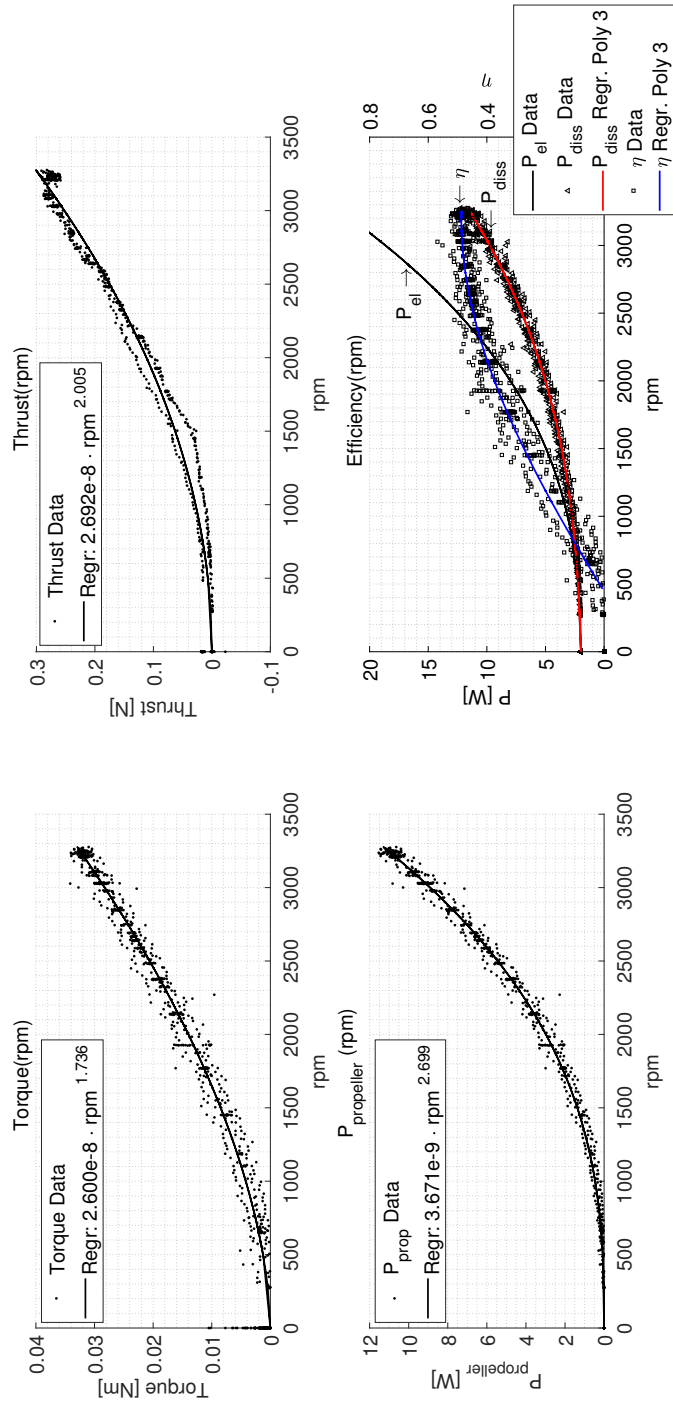


Figure B.5: Results of the first experimental test.



## Appendix C

### CFD solver

The common factor to all the thesis work is the Computational Fluid Dynamics (CFD) analysis. CFD is defined as the set of methodologies that enable the computer to provide numerical simulations of fluid flows [8]. The whole system is transformed into a virtual environment. This can be opposed to an experimental investigation, characterized by a prototype of the system. Computational fluid dynamics is a new approach which comes up with the experimental and the theoretical approach, helping to interpret and understand their results, and vice versa. It can be said briefly that it consists in the implementation of the fluid dynamics laws on a calculator, taking advantage of its capacity to do a lot of calculations in relatively small time. The equations to be solved are five, they represent three physic principles and they are called Navier-Stokes equations:

1. Mass conservation;
2. Momentum conservation (Newton's second law);
3. Energy conservation (thermodynamics first principle).

All equations are subjects to boundary conditions and are valid only if the fluid can be considered a continuum. In differential form:

$$\frac{\partial \rho}{\partial t} + \nabla \cdot (\rho \mathbf{V}) = 0 \quad (\text{C.1})$$

$$\frac{\partial (\rho u)}{\partial t} + \nabla \cdot (\rho u \mathbf{V}) = -\frac{\partial p}{\partial x} + \frac{\partial (\tau_{xx})}{\partial x} + \frac{\partial (\tau_{yx})}{\partial y} + \frac{\partial (\tau_{zx})}{\partial z} + \rho f_x \quad (\text{C.2})$$

$$\frac{\partial (\rho v)}{\partial t} + \nabla \cdot (\rho v \mathbf{V}) = -\frac{\partial p}{\partial y} + \frac{\partial (\tau_{xy})}{\partial x} + \frac{\partial (\tau_{yy})}{\partial y} + \frac{\partial (\tau_{zy})}{\partial z} + \rho f_y \quad (\text{C.3})$$

$$\frac{\partial (\rho w)}{\partial t} + \nabla \cdot (\rho w \mathbf{V}) = -\frac{\partial p}{\partial z} + \frac{\partial (\tau_{xz})}{\partial x} + \frac{\partial (\tau_{yz})}{\partial y} + \frac{\partial (\tau_{zz})}{\partial z} + \rho f_z \quad (\text{C.4})$$

$$\begin{aligned}
 \frac{\partial}{\partial t} \left[ \rho \left( e + \frac{V^2}{2} \right) \right] + \nabla \cdot \left[ \rho \left( e + \frac{V^2}{2} \right) \mathbf{V} \right] = \rho \dot{q} + \frac{\partial}{\partial x} \left( k \frac{\partial T}{\partial x} \right) + \frac{\partial}{\partial y} \left( k \frac{\partial T}{\partial y} \right) \\
 + \frac{\partial}{\partial z} \left( k \frac{\partial T}{\partial z} \right) - \frac{\partial (up)}{\partial x} - \frac{\partial (vp)}{\partial y} - \frac{\partial (wp)}{\partial z} + \frac{\partial (u\tau_{xx})}{\partial x} \\
 + \frac{\partial (u\tau_{yx})}{\partial y} + \frac{\partial (u\tau_{zx})}{\partial z} + \frac{\partial (v\tau_{xy})}{\partial x} + \frac{\partial (v\tau_{yy})}{\partial y} \\
 + \frac{\partial (w\tau_{zy})}{\partial z} + \frac{\partial (w\tau_{xz})}{\partial x} + \frac{\partial (w\tau_{yz})}{\partial y} + \frac{\partial (w\tau_{zz})}{\partial z} + \rho \mathbf{f} \cdot \mathbf{V}
 \end{aligned} \tag{C.5}$$

There are four independent variables,  $x$ ,  $y$ ,  $z$  and  $t$  (spatial coordinates and time) and six dependent variables: pressure  $p$ , velocity (three components as velocity is a vector)  $u$ ,  $v$  and  $w$ , density  $\rho$  and temperature  $T$ . There are five equations for six unknowns, another equation is needed to close the problem: the sixth equation is usually the equation of state C.6, which relates pressure, temperature and density.

$$\boxed{p = \rho RT} \tag{C.6}$$

The equations listed above are nonlinear partial differential equations, hence are very difficult to solve analytically, they can be written in differential or integral form (differential in this case) and their formulation can be conservative or non-conservative (conservative in this case). If an inviscid flow is considered, some simplifications can be done (in particular energy equation is decoupled from the other two) and they are called *Euler equations*.

The Navier-Stokes equations can be solved analytically only for a small number of cases, most of them have a limited industrial interest.

CFD is based on the discretization of a domain, this leads to *approximation errors*. These errors are unavoidable because they arise in the moment when a continuum problem is resolved through an iterative method. There are various type of numerical errors, they can be convergence, discretization or round-off errors. In particular, round-off errors depend from the machine accuracy and are caused by the wrong representation of real numbers through binary code.

Another problem that arise is the *uncertainty*, which is not due to the CFD solver but is due to the non perfect knowledge of the problem. In this category are included the assumptions and the simplifications done to the physical model or errors due to the wrong imposition of boundary and initial conditions.

Given these potential issues, a numerical solution method has to satisfy a certain number of properties [27]:

- Consistency: the discretization should be exact as the grid spacing tends to zero, so there should be no difference between the exact and the discretized equation;
- Stability: the method doesn't magnify the errors that appear in the course of the numerical processes;
- Convergence: the solution of the discretized equations must tend to the solution of the exact equations as the grid spacing tends to zero;

- Conservation: as the equation to be solved are conservation laws, the numerical scheme should also respect this laws;
- Realizability: Models of phenomena that are too complex to treat directly should be designed to guarantee physically realistic solutions;
- Accuracy: All the systematic errors of the approximate solution should be as low as possible.

The technique commonly used in CFD is the *Finite Volume Method*: the domain is divided in small control volumes (cells), in the centre of these cells are resolved the integral balance equations. The cells communicate between each other through surface integrals and in order to know the quantities at the interface different discretization techniques can be used. The discretization techniques represent the main difference between discretization methods, which are one of the most important element of a CFD simulation.

Another important feature of a simulation is obviously the domain discretization, in other words the *mesh*. The accuracy of the solution (but also the convergence) is strictly dependent from the spatial discretization. As a consequence the grid generation process is a crucial step in the CFD and can be really time consuming especially in the case of complex geometries (as explained Appendix A).

The third main element, after accuracy and discretization, is the *calculation time*: one can have really fine grid which guarantees the minimum discretization error but has to deal with the time necessary to resolve the equation for all the cells.

The simulation is a balance between many elements, what the CFD analyst has to do is finding the best combination between all these factors.

## C.1 Rotating grids

In computational fluid dynamics, the Navier-Stokes equations can be written in many ways all equal each other. The motion of a fluid can be described by following the motion of a fluid particle<sup>1</sup>, this type of approach is called *Lagrangian*. On the contrary, the *Eulerian* description analyse the temporal evolution of the flow variables in every point of the domain.

In a Lagrangian approach it is possible to define the substantial derivative:

$$\frac{D(.)}{Dt} = \underbrace{\frac{\partial (.)}{\partial t}}_{\text{Local derivative}} + \underbrace{\mathbf{V} \cdot \nabla (.)}_{\text{Convective derivative}}$$

The first term represents the local variation of (.) in a specific point in the time interval  $\partial t$ , while in the second term  $\mathbf{V}$  is the observer velocity and  $\nabla(.)$  is the gradient of the variable to be measured. The scalar product is important because it takes into account the direction along which the observer moves. The substantial derivative can also be called *Lagrangian derivative*

---

<sup>1</sup>A fluid particle is an infinitesimal volume which contains a numbers of particles sufficient to define average quantities such as density, velocity, etc..

while the local derivative can be called *Eulerian derivative*.

In all the simulations done in this work rotating grid are encountered. For a rotating grid the Navier-Stokes equation change a little their formulation [41]:

$$\frac{d}{dt} \int_V \rho dV - \int_S \rho (\mathbf{U} - \mathbf{u}) \cdot \mathbf{n} dS = 0 \quad (\text{C.7})$$

$$\frac{d}{dt} \int_V \rho \mathbf{u} dV - \int_S \rho \mathbf{u} (\mathbf{U} - \mathbf{u}) \cdot \mathbf{n} dS + \int_V \nabla p dV - \int_V \rho \mathbf{f} dV = 0 \quad (\text{C.8})$$

$$\frac{d}{dt} \int_V \rho E dV - \int_S \rho E (\mathbf{U} - \mathbf{u}) \cdot \mathbf{n} dS + \int_S \nabla p \mathbf{u} \cdot \mathbf{n} dS - \int_V \rho \mathbf{f} \cdot \mathbf{u} dV = 0 \quad (\text{C.9})$$

where  $\mathbf{U}$  is the velocity vector of the surface  $S$ . The equations are written in integral form because it is easier to reason over a volume  $V$  which can be moved with an arbitrary velocity  $\mathbf{U}$ . The main difference with the equations written previously for a non rotating grid is in the convective term: if  $\mathbf{U} = 0$  the equation are in the Eulerian form, if  $\mathbf{U} = \mathbf{u}$  the equations are in Lagrangian form.

## C.2 Turbulence

The application of CFD to real life flow systems, in nature or technology, makes necessary dealing with turbulent flows, as these are the most easily encountered. In a turbulent flow, the velocity field is random: this characteristic needs to be explained as it can be misleading. Considering a flow experiment that can be repeated as many times as wanted under a certain set of conditions and considering an event (for example the velocity in a certain direction being less than a fixed value), if the event occurs then it is certain or sure, if the event cannot occur then it is impossible. But there is one more possibility: the event may occur or it may not occur. In this last case the event is random (the velocity is a random variable in this example). Being the velocity a random variable means that it does not have an unique value, i.e. every time the experiment is performed under the same conditions a different velocity value is found [28].

Turbulence contains a wide range of different scales. Following the concept of energy cascade elaborated by Richardson it can be said that turbulence is composed of eddies<sup>2</sup> of different sizes.

$$\frac{\partial \omega_i}{\partial t} + \underbrace{u_j \frac{\partial u_i}{\partial x_j}}_{\text{Convection}} = \underbrace{\omega_j \frac{\partial u_i}{\partial x_j}}_{\text{Vortex stretching}} + \underbrace{\nu \frac{\partial^2 \omega_i}{\partial x_j \partial x_j}}_{\text{Viscous diffusion}} \quad (\text{C.10})$$

In the equation<sup>3</sup> of vorticity  $\omega$ , the term  $\omega_j \frac{\partial u_i}{\partial x_j}$  is responsible of the *vortex stretching*. This three-dimensional phenomenon transfer the energy associated to the fluctuations of the larger

<sup>2</sup>A fluid region characterized by elevated vorticity.

<sup>3</sup>Index  $i$  and  $j$  indicate the different components of the vector to which they are referred. In this case for example  $i = 1$  indicates the velocity component along the x-axis. With this notation,  $u$  is the velocity vector, not the y-component of the velocity.

scales towards the smaller ones through non linear interactions. The smaller eddies undergo a similar process and transfer energy to yet smaller scales. This energy cascade continues until the Reynolds number is sufficiently small that the eddy motion is stable. So far the process has been inviscid, but in the smallest scale (called Kolmogorov scale) the energy is dissipated by viscous action (figure C.1).

Kolmogorov determined the spatial ( $\frac{\hat{\eta}}{l}$ ) and temporal ( $\frac{\hat{t}}{t}$ ) ratios of the smallest to largest scales

$$\boxed{\frac{\hat{\eta}}{l} = Re^{-3/4}} \quad (C.11)$$

$$\boxed{\frac{\hat{t}}{t} = Re^{-1/2}} \quad (C.12)$$

As these scales are extremely small, the DNS<sup>4</sup> are really demanding in terms of computational cost. Anyway, in many engineering applications what really matter are the flow averaged quantities, for this reason the RANS equation turn out to be very useful.

Following this approach, every quantities can be decomposed into a *mean* and a *fluctuating* field. Considering the x-velocity field it can be written

$$\underbrace{U_i(x, t)}_{\text{Instant value}} = \underbrace{\langle U_i(x, t) \rangle}_{\text{Mean}} + \underbrace{u'_i(x, t)}_{\text{Fluctuating}} \quad (C.13)$$

With this notation, the Navier-Stokes equations can be rewritten so the RANS equations are obtained. The continuity equation can be rewritten<sup>5</sup>:

$$\frac{\partial (U_i + u'_i)}{\partial x_i} = 0 \quad (C.14)$$

averaging this equation

$$\frac{\partial U_i}{\partial x_i} = 0 \quad (C.15)$$

and subtracting the result from the previous equation

$$\frac{\partial u'_i}{\partial x_i} = 0 \quad (C.16)$$

it is clear now that both the mean and the fluctuating parts of the velocity field individually satisfy the the usual form of the continuity equation [29]. Following a similar process for the momentum equation it can be written

$$\frac{\partial U_i}{\partial t} + U_j \frac{\partial U_i}{\partial x_j} = -\frac{1}{\rho} \frac{\partial p}{\partial x_i} + \nu \frac{\partial^2 U_i}{\partial x_j^2} - \frac{\partial}{\partial x_j} (\overline{u_i u_j}) \quad (C.17)$$

<sup>4</sup>Simulation in which Navier-Stokes equations are numerically solved without any turbulence model.

<sup>5</sup>The density is assumed to be constant.

where the last term is not present in the laminar case, it represent the action of the velocity fluctuation on the mean flow arising from the non linearity of the Navier-Stokes equation. The quantity  $-\rho \overline{u_i u_j}$  is called *Reynolds stress tensor* and represent the correlation of two components of the velocity fluctuation at the same point. It is now necessary to quantify the Reynolds stresses: the *turbulent-viscosity hypothesis*, introduced by Boussinesq in 1877, is analogous to the stress relation for a Newtonian fluid. It states that the Reynolds stress is proportional to the mean rate of strain

$$-\rho \overline{u_i u_j} + \frac{2}{3} \rho k \delta_{ij} = \rho \nu_t \left( \frac{\partial U_i}{\partial x_j} + \frac{\partial U_j}{\partial x_i} \right) = 2 \rho \nu_t \overline{S}_{ij} \quad (\text{C.18})$$

where  $k = \overline{u'_i u'_j} / 2$  is the mean turbulent kinetic energy per unit mass,  $\overline{S}_{ij}$  is the mean rate of strain tensor,  $\delta_{ij}$  is the Kroeneker delta and  $\nu_t$  is the turbulent viscosity or eddy viscosity. Anyway there are cases in which the hypothesis fails significantly:

- Strongly swirling flows;
- Flow with significant curvature;
- Fully developed flows in ducts of non circular cross-section

It is important to remember that this interpretation does not leads to a simplification. Equations C.16 and C.17 still does not form a closed system so it is necessary to introduce one (or more) relation between mean velocity field and Reynolds stresses. These relations form a *turbulence model*. Besides the DNS and the RANS method there is a third way to run a simulation and is called *Large Eddy Simulation (LES)*. In this method the larger three-dimensional unsteady turbulent motions are directly represented while the smaller scale motions are modelled. This method lies between RANS and DNS and it is made necessary by their limitations. In fact, LES is more reliable than RANS concerning flows with large-scale unsteadiness but has less computational cost than DNS (which is inapplicable to high-Reynolds flows).

### One-equation Spalart-Allmaras turbulence model

The S-A turbulence model is a one-equation model, designed for aerospace applications. It is quite robust and effective in modelling the flow on an airfoil, with adverse pressure gradients in the boundary layer and it is also used in turbomachinery applications [29].

The equation modelled is the one for the kinematic eddy turbulent viscosity  $\nu_t$ , in its original form, the model is effectively a low-Reynolds number model, requiring the viscous region of the boundary layer to be properly resolved ( $y^+ < 1$ ). A one-equation model for  $\nu_t$  is the lowest level at which a model can be complete; Spalart and Allmaras developed the model to remove the incompleteness of algebraic and one-equation models based on  $k$ , and yet have a model which has less computational cost than a two-equation model. The model equation is

$$\frac{D \nu_t}{Dt} = \nabla \cdot \left( \frac{\nu_t}{\sigma_\nu} \nabla \nu_t \right) + S_{\nu_t} \quad (\text{C.19})$$

where  $S_{\nu_t}$  is a source term which depends on the laminar or turbulent viscosities,  $\nu$  and  $\nu_t$ , the mean vorticity, the turbulent viscosity gradient  $\nabla \nu_t$  and the distance to the nearest wall. By having only one equation, this model grants faster convergence.

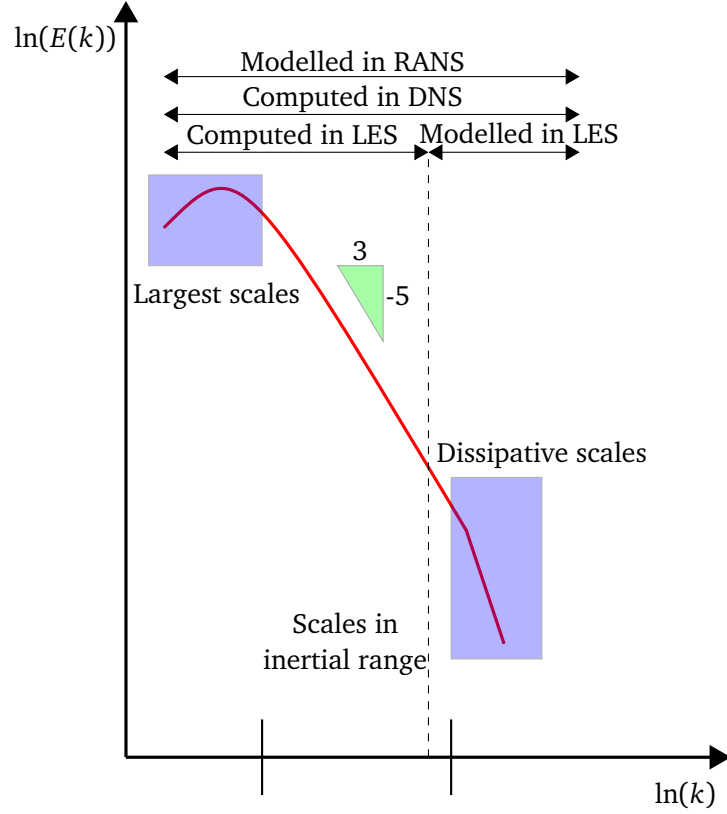


Figure C.1: Schematic of the energy cascade process.

### Two-equations realizable $k - \varepsilon$ turbulence model

This turbulence model in CFD++ is used as default [31], as it is the most widely used turbulence model. It solves transport equations for the turbulence kinetic energy ( $k$ ) and its dissipation rate ( $\varepsilon$ ).

In addition to the Boussinesq relation, the  $k - \varepsilon$  model consists of:

- The model transport equation for  $k$

$$\frac{\rho k}{\partial t} + \frac{\partial}{\partial x_j}(U_j \rho k) = \frac{\partial}{\partial x_j} \left[ \left( \mu + \frac{\mu_t}{\sigma_k} \right) \frac{\partial k}{\partial x_j} \right] + P_k - \rho \varepsilon \quad (\text{C.20})$$

where  $P_k = -\rho u_i \bar{u}_j \partial U_i / \partial x_j$  is the production term and  $\sigma_k = 1.0$  is a constant

- The model transport equation for  $\varepsilon$ ;

$$\frac{\rho \varepsilon}{\partial t} + \frac{\partial}{\partial x_j}(U_j \rho \varepsilon) = \frac{\partial}{\partial x_j} \left[ \left( \mu + \frac{\mu_t}{\sigma_\varepsilon} \right) \frac{\partial \varepsilon}{\partial x_j} \right] + (C_{\varepsilon 1} P_k - C_{\varepsilon 2} \rho \varepsilon + E) T_t^{-1} \quad (\text{C.21})$$

where  $T_t$  is a realizable estimate of the turbulence timescale,  $C_{\varepsilon 1} = 1.44$ ,  $C_{\varepsilon 2} = 1.92$  and  $\sigma_\varepsilon = 1.3$  are other constants of the model.

- The specification of the turbulent viscosity as

$$\nu_t = C_\mu k^2 / \varepsilon$$

Where  $C_\mu = 0.09$  is one of the five constants of the model.

Constant	Value
$c_\mu$	0.09
$c_{\varepsilon 1}$	1.44
$c_{\varepsilon 2}$	1.92
$\sigma_k$	1.0
$\sigma_\varepsilon$	1.3

Table C.1: Constant used in  $k - \varepsilon$  turbulence model.

This turbulence model will be largely used in the following simulations as it is the one which gives the best convergence performance for all the cases encountered.

### Two-equations Menter SST turbulence model

The third turbulence model analysed in this section is the two-equation SST model. It is a combination of the  $k - \omega$  model elaborated by Wilcox and the  $k - \varepsilon$  model already explained. Wilcox proposed in his model to use the turbulent frequency  $\omega = \frac{\varepsilon}{C_\mu k}$  instead of  $\varepsilon$ . The model obtained is more accurate in the near-wall zone but too much sensible to the freestream conditions.

For this reason Menter blended the two models in order to take advantage of the  $k - \omega$  model near wall and of the  $k - \varepsilon$  model in the outer region. The two model equations are:

$$\frac{\partial(\rho k)}{\partial t} + \frac{\partial(\rho u_j k)}{\partial x_j} = P - \beta^* \rho \omega k + \frac{\partial}{\partial x_j} \left[ (\mu + \sigma_k \mu_t) \frac{\partial k}{\partial x_j} \right] \quad (\text{C.22})$$

$$\frac{\partial(\rho \omega)}{\partial t} + \frac{\partial(\rho u_j \omega)}{\partial x_j} = \frac{\gamma}{\nu_t} P - \beta \rho \omega^2 + \frac{\partial}{\partial x_j} \left[ (\mu + \sigma_\omega \mu_t) \frac{\partial \omega}{\partial x_j} \right] + 2(1 - F_1) \frac{\rho \sigma_{\omega 2}}{\omega} \frac{\partial k}{\partial x_j} \frac{\partial \omega}{\partial x_j} \quad (\text{C.23})$$

The following constants (table C.2) are used to close the system

It has been added then an equation to control the value of  $\mu_t$ , as this model tends to overestimate its value, to improve the model's performance in the wake region and in adverse gradient regions:

$$\mu_t = \frac{a_1 \rho k}{\max(a_1 \omega, S^* F_2)} \quad (\text{C.24})$$

where  $F_2$  is a *blending function* similar to  $F_1$ ,  $a_1$  is a constant and  $S^*$  is linked to the deformation velocity tensor.

	Constant	Value
$k - \omega$ closure	$\sigma_{k1}$	0.85
	$\sigma_{\omega1}$	0.65
	$\beta_1$	0.075
$k - \varepsilon$ closure	$\sigma_{k2}$	1.0
	$\sigma_{\omega2}$	0.856
	$\beta_2$	0.0828
SST closure constants	$\beta^*$	0.09
	$a_1$	0.31

Table C.2: SST turbulence model constants.

### Algebraic models

It is straightforward that two-equation models are more accurate than one-equation models, but Spalart-Allamaras model is still used thanks to its convergence velocity. Anyway, also *algebraic models* (zero-equation models) exist. They are models that do not require the solution of any additional equations, and are calculated directly from the flow variables. As a consequence, zero equation models may not be able to properly account for history effects on the turbulence, such as convection and diffusion of turbulent energy. These models are often too simple to be used in general situations, but can be quite useful for simpler flow geometries or in start-up situations (for example the initial phases of a computation in which a more complicated model may have difficulties). The two most well known zero equation models are:

- Baldwin-Lomax model;
- Cebeci-Smith model.

These models are not used in the simulations but it is useful to remind their existence.

### C.3 Boundary layer

The presence of walls and being the flow viscous make necessary the presence of a zone where the velocity of the flow is zero. As a consequence it must exist a transition zone, a layer, where the velocity gradually passes from the freestream value to zero. This concept was introduced by Ludwig Prandtl in 1904 with the *boundary layer theory*.

In this fluid region it is possible to define two *wall variables*:

- $y^+ = \frac{y u_\tau}{\nu}$
- $u^+ = \frac{V}{u_\tau}$

where  $u_\tau = \sqrt{\frac{\tau_w}{\rho}}$  is the *friction velocity* and  $\tau_w = \mu \left( \frac{\partial u_i}{\partial x_j} \right)$ , with  $\mu$  being the *dynamic viscosity*. Looking at the  $y^+$  formulation it is evident the similarity with the Reynolds number formulation, where the characteristic length here is the coordinate  $y$ .

$y^+$  is an important parameter as, depending on its value, it can define different flow regions. In fact, when  $y^+$  tends to zero, through the similarity with the Reynolds number, it is logical to imagine that the viscous effects increase considerably: this region ( $y^+ < 5$ ) is called *viscous sublayer*. The  $30 < y^+ < 500$  range is called *logarithmic sublayer* while between this region and the viscous sublayer there is the *buffer layer*. Each of these regions has a specific *wall velocity profile*:

- Viscous sublayer:

$$u^+ = y^+$$

- Logarithmic sublayer:

$$u^+ = \frac{1}{\chi} \ln y^+ B$$

- Buffer layer: it represent a sort of link between the two preceding laws.

In the logarithmic sublayer  $\chi$  represent the *Von Karman* constant. For most of the turbulent flows:

$$\chi = 0.41 \quad B = 5.2$$

confirming the universality of the law. It is possible to plot these law obtaining figure

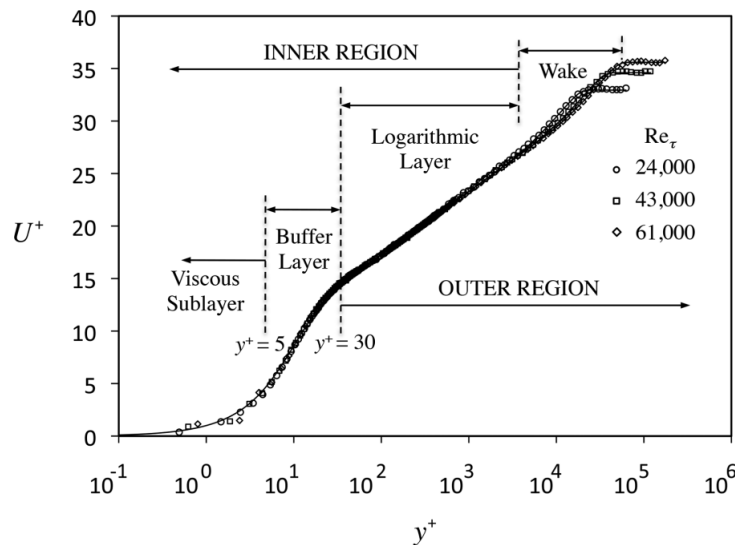


Figure C.2: *Universal wall law.*

Traditionally, there are two approaches to model the near-wall zone. The first does not resolve the viscous sublayer and buffer layer (where viscosity has a relevant effect). Through the use of semi-empirical formulas, called *wall functions*, it is created a link between the fully-turbulent region and the zone dominated by viscosity. They come in handy because the turbulence model do not need to account the presence of the wall. In the second approach, turbulence models are modified to enable the viscosity-affected region to be resolved with a mesh all the way to

the wall, including the viscous sublayer.

All the grids implemented in this work respect the second approach. For this reason, to resolve the viscous sublayer the grid spacing, in the direction normal to the wall, is made so that *there are at least 10 cells in the boundary layer*. Furthermore, if more accuracy is needed, it is sufficient to increase the number of cells included in the boundary layer, generally the increase in accuracy is well worth the additional computing costs.

For unstructured mesh, it is recommended to generate some prism layers near the wall for an accurate prediction of the wall boundary layers.



# Bibliography

- [1] Space.com website, <https://www.space.com>, consulted in October 2018.
- [2] ESA website, <https://www.esa.int>, consulted in October 2018.
- [3] NASA website, <https://www.nasa.gov>, consulted in October 2018.
- [4] SpaceX website, <https://www.spacex.com>, consulted in October 2018.
- [5] L. A. Young, E. Aiken, P. Lee, G. Briggs, *Mars Rotorcraft: Possibilities, Limitations and Implications for Human/Robotic Exploration*, 2005.
- [6] C. Leovy, *Weather and climate on Mars*, Department of Atmospheric Sciences, University of Washington.
- [7] M. Talmelli, *Mars drone rotors analysis in Mars atmosphere*.
- [8] C. Hirsch, *Numerical computation of internal & external flows*, Vol.1 - Fundamentals of Computational Fluid Dynamics.
- [9] T. Désert, J-M. Moschetta, H. Bézard, *Aerodynamic Design of a Martian Micro Air Vehicle*, 7th European Conference for Aeronautics and Aerospace Sciences (EUCASS), 2017.
- [10] K. J. Corfeld, R. C. Strawn, L. N. Long, *Computational Analysis of a Prototype Martian Rotorcraft Experiment*, 20th AIAA Aerodynamics Conference 24-26 June 2002.
- [11] J. M. Fu, Z. F. Xia, F. Mohd-Zawawi, E. Benard, J-M. Moschetta, *Numerical Investigation of a Proof-of-Concept Rotor in Martian Atmosphere*.
- [12] J-M. Moschetta, H. Bézard, *Aerodynamic Study of a Micro-UAV for Mars Exploration*, 2015.
- [13] L. A. Young, G. A. Briggs, *Smart Rotorcraft Field Assistants for Terrestrial and Planetary Science*, 2004.
- [14] ResearchGate website, <https://www.researchgate.net>, consulted in November 2018.
- [15] L. A. Young, E. Aiken, *Experimental Investigation and Demonstration of Rotary-Wing Technologies for Flight in the Atmosphere of Mars*, 58th Annual Forum of the AHS (American Helicopter Society), June 11-13 2002.
- [16] M. Benedict, J. Winslow, Z. Hasnain, I. Chopra, *Experimental Investigation of Micro Air Vehicle Scale Helicopter Rotor in Hover*, Revised version of the paper presented at the American Helicopter Society Annual Forum, May 20–22 2014.
- [17] M. McCoy, A. J. Wadcock, L. A. Young, *Documentation of the Recirculation in a Closed-Chamber Rotor Hover Test*, 2016.
- [18] M. Benedict, R. Shrestha, V. Hrishikeshavan I. Chopra, *Hover Performance of a Small-Scale Helicopter Rotor for Flying on Mars*, 2016.
- [19] J. Garcia, T. Mathy, H. Diez, *MARS Original System for Qualitative Imaging and Tactical Operations. System and Architecture Analysis.*, 2015.
- [20] A. Botta, *MARS DRONE - Engine & Rotor test*.

- [21] A. Botta, *MARS DRONE - Rotors and Engines testing in a Mars-like Atmosphere*.
- [22] J. H. Abbot, A. von Doenhoff, *Theory of wing sections*, 1959.
- [23] J. Winslow, H. Otsuka, B. Govindarajan, I. Chopra, *Basic Understanding of Airfoil Characteristics at Low Reynolds Numbers ( $10^4 - 10^5$ )*, 2018.
- [24] S. P. Sane, *The aerodynamics of insect flight*, Department of biology, University of Washington, 2003.
- [25] E. Polhamus, *Prediction of vortex-lift characteristics by a leading edge suction analogy*, 1971.
- [26] C. P. Ellington, C. Van den Berg, A. P. Willmott, A. L. R. Thomas, *Leading-edge vortices in insect flight*, 1996.
- [27] D. D'Ambrosio, *Computational Fluid Dynamics course slides*.
- [28] S. B. Pope, *Turbulent flows*, Cornell University.
- [29] D. J. Tritton, *Physical Fluid Dynamics*.
- [30] Thales Group website, <https://www.thalesgroup.com>, consulted in December 2018.
- [31] Metacomp, *CFD++ user manual*.
- [32] S. P. Sane, *The aerodynamics of insect flight*.
- [33] Nasa Langley Research Center site, <https://turbmodels.larc.nasa.gov>, consulted in January 2019.
- [34] W. Johnson, *Helicopter theory*.
- [35] ANSYS, *ANSYS Fluent theory guide*.
- [36] D. Zaza, *Analisi delle prestazioni e del campo di moto indotto da un'elica in ambiente marziano*, Politecnico di Torino.
- [37] R. Modarres, D. A. Peters, *Optimum blade loading for a powered rotor in descent*, Washington University, 2016.
- [38] P. J. Kunz, *Aerodynamics and design for ultra-low Reynolds number flight*, Stanford University, 2003.
- [39] W. J. F. Koning, *Generation of Performance Model for the Aeolian Wind Tunnel (AWT) Rotor at Reduced Pressure*, NASA Ames Research Center, December 2018.
- [40] W. J. F. Koning, G. A. Ament, *Isolated Rotor Forward Flight Testing From One Atmosphere Down to Martian Atmospheric Densities*, NASA Ames Research Center, 2018.
- [41] C. W. Hirt, A. A. Amsden, J. L. Cook, *An Arbitrary Lagrangian-Eulerian Computing Method for All Flow Speeds*, University of California, Los Alamos Scientific Laboratory, 1972.